NOAA Technical Memorandum OAR ETL-304

LABORATORY MODELING AND THEORETICAL STUDIES OF SURFACE WAVE MODULATION BY A MOVING SPHERE

(MEMO-6)

L.A. Ostrovsky (Editor)

Environmental Technology Laboratory
Boulder, Colorado
March 2002

noaa NATIONAL OCEANIC AND ATMOSPHERIC ADMINISTRATION / Oceanic and Atmospheric Research Laboratories

NOAA Technical Memorandum OAR ETL-304

LABORATORY MODELING AND THEORETICAL STUDIES OF SURFACE WAVE MODULATION BY A MOVING SPHERE

(MEMO-6)

L.A. Ostrovsky (Editor)

Environmental Technology Laboratory
Boulder, Colorado
March 2002

UNITED STATES DEPARTMENT OF COMMERCE

Donald L. Evans
Secretary

NATIONAL OCEANIC AND ATMOSPHERIC ADMINISTRATION

VADM Conrad C. Lautenbacher, Jr.
Under Secretary for Oceans
and Atmosphere/Administrator

Oceanic and Atmospheric Research Laboratories

David L. Evans
Director

This memorandum presents the results of the experimental and theoretical research conducted in 2000 by the Institute of Applied Physics (IAP) of the Russian Academy of Sciences in the framework of the agreement between IAP and the NOAA Environmental Technology Laboratory (ETL). It reflects the second parts of two IAP reports dealing with surface effects; namely, interactions of background surface gravity waves with streamlining currents around the sphere. Correspondingly, the memorandum consists of two chapters; for convenience, enumeration of equations, reference lists, and figures are given for these chapters separately. The experiments were performed in the large tank at the IAP.

Head of the Project: V. I. Talanov
Deputy Head: V. V. Bakhanov
Program Coordinator: L. A. Ostrovsky
Participants: V. I. Kazakov, D. P. Korotkov, B. V. Serin, S. N. Vlasov, E. V. Koposova, and O. N. Kemarskaya.

Chapter 1. SURFACE WAVE MODULATION BY A FLOW AROUND A MOVING SPHERE

Abstract

This chapter reflects the first stage of the IAP work in 2000 regarding interactions between the current around a moving sphere and the surface waves excited independently by a wave maker. It contains a theoretical study of modulated gravity waves which includes an account for their nonlinearity. The latter may result in modulation instability which, in turn, can enhance the effect of wave modulation by a surface current. Also, an experimental design to be used in the second chapter is described, together with preliminary studies of gravity waves.

Contents of Chapter 1

INTRODUCTION

Theoretical and experimental studies of surface wave transformation in the field of an inhomogeneous current have been performed by IAP for several years [1-7]. It was shown [1,3,4] that even weak inhomogeneous flows can strongly affect the surface wave characteristics. Moreover, the nonlinearity of the surface wave can sharply increase the wave-amplitude variability in a broad frequency range due to the interference of the effect of modulation instability [2, 7]. At the same time, calculations made according to the equations used in [2, 7] that take into account the third-order nonlinearity in slopes have shown that an intensive small-scale variability of the wave develops with time which limits the applicability of the basic equation. This is due to the approximation of [2, 7] in which the growth rate does not decrease for small-scale perturbations. At the same time, as noted in [8], the account of nonlinear dispersion of surface wave imposes a strong limitation on the small-scale instability.

Here, a more consistent theoretical consideration of this problem is given. In sec. 1, a nonlinear equation for the complex amplitude of surface waves on an inhomogeneous flow is obtained which incorporates both nonlinear and full linear dispersion for gravity-capillary waves. In sec. 2 the regions of instability are found for this equation, and in sec. 3 a program for its numerical solution is described. The program will be used at the second stage of this work for calculations of surface wave transformation in the field of inhomogeneous current for the conditions of the planned experiment in a large thermostratified tank. The results of sec. 2 will be used for interpretation of calculation results.

In sec. 4, the preparatory experiments are outlined; namely, the systems for measurement of surface wave parameters are described, which will be used at the second stage of this work for investigation of the moving sphere effect on surface waves. Then, the results of the study of background surface wave amplitude distribution are presented.

1. AN EQUATION FOR GRAVITY-CAPILLARY SURFACE WAVE AMPLITUDE UNDER THE ACTION OF AN INHOMOGENEOUS CURRENT

We shall consider here transformation of deep-water gravity-capillary surface waves in an inhomogeneous current field assuming that characteristic scales of current variations (both horizontal and vertical) are much larger than the surface wavelengths and thus the depth of their penetration into the water. Let the current have the form $\mathbf{U} = -U_0\mathbf{x}_0 + \mathbf{u}(x, y)$; i.e., it consists of the main homogeneous flow and its perturbation, on the water surface. Then, assuming the current velocity is a function of only horizontal coordinates, we give a known dispersion equation for linear surface waves:

$$[\omega - \mathbf{k}(-U_0\mathbf{x}_0 + \mathbf{u}(x,y))]^2 = gk + Tk^3, \tag{1.1}$$

where $\mathbf{k}$ is the wave vector of surface waves, and ω is the frequency in the reference frame fixed with respect to the bottom. We introduce dimensionless variables: $\tilde{\mathbf{k}} = \dfrac{\mathbf{k}}{k_*}$, $\tilde{\omega} = \dfrac{\omega}{k_* U_0}$, $\boldsymbol{\beta} = \dfrac{\mathbf{u}}{U_0}$, $\tilde{T} = \dfrac{Tg}{16U_0^4}$, where $k_* = \dfrac{g}{4U_0^2}$, T is the surface tension coefficient normalized to water density, and g is the gravity acceleration. The parameters of an unperturbed surface wave incident on the inhomogeneous current region are designated as $\tilde{\omega}_0$, $\tilde{k}_{x0}$, and $\tilde{k}_{y0}$. Choosing a positive branch of

dispersion relation (1.1) which corresponds to the wave propagating in a positive direction in the absence of current, we obtain, in dimensionless variables:

$$\Omega = -\tilde{\omega}_0 - \tilde{k}_{x0}(1-\beta_x) + \tilde{k}_{y0}\beta_y - (1-\beta_x)\chi_x + \beta_y\chi_y + \tag{1.2}$$

$$+ 2\sqrt{\left[\left(\tilde{k}_{x0}+\chi_x\right)^2 + \left(\tilde{k}_{y0}+\chi_y\right)^2\right]^{\frac{1}{2}} + \tilde{T}\left[\left(\tilde{k}_{x0}+\chi_x\right)^2 + \left(\tilde{k}_{y0}+\chi_y\right)^2\right]^{\frac{3}{2}}} \quad .$$

Here, Ω, χ_x, and χ_y are perturbations of the wave frequency and of the components of the wave number, respectively. By using the expression (1.2) one can obtain an equation for a complex amplitude of linear gravity-capillary waves. For this purpose we introduce the operators:

$$\frac{\partial}{\partial\tilde{t}} = i\Omega, \qquad \frac{\partial}{\partial\tilde{x}} = -i\chi_x, \qquad \frac{\partial}{\partial\tilde{y}} = -i\chi_y,$$

$$L\,J = \frac{1}{2\pi}\int\exp\left(i\left(k_x'\tilde{x} + k_y'\tilde{y}\right)\right)\cdot$$

$$\cdot\left[\left(\left(\tilde{k}_{x0}+k_x'\right)^2 + \left(\tilde{k}_{y0}+k_y'\right)^2\right)^{\frac{1}{2}} + \tilde{T}\left(\left(\tilde{k}_{x0}+k_x'\right)^2 + \left(\tilde{k}_{y0}+k_y'\right)^2\right)^{\frac{3}{2}}\right]^{\frac{1}{2}} \tilde{J}\left(k_x', k_y'\right) d\,k_x' d\,k_y' \quad ,$$

where $\tilde{J}\left(k_x', k_y'\right)$ is the Fourier transform of the function J:

$$\tilde{J}\left(k_x', k_y'\right) = \frac{1}{2\pi}\int\exp\left(-i\left(k_x'\tilde{x} + k_y'\tilde{y}\right)\right) J(\tilde{x},\tilde{y})\, d\,\tilde{x}\, d\,\tilde{y},$$

$\tilde{t} = t\,k_* U_0$, $\tilde{x} = x k_*$, $\tilde{y} = y k_*$ being the dimensionless time and coordinates. Then the equation for linear surface wave amplitude is

$$\frac{\partial A}{\partial\tilde{t}} = 2iL\,A + (1-\beta_x)\frac{\partial A}{\partial\tilde{x}} - \beta_y\frac{\partial A}{\partial\tilde{y}} + i\left[(\beta_x - 1)\tilde{k}_{x0} + \beta_y\tilde{k}_{y0} - \tilde{\omega}_0\right]A.$$

Nonlinearity of surface waves is taken into account here following [9]. We assume that the value β is small and thus variations of the wave number χ_x, χ_y are also small. As a result, in the dimensionless variables introduced in this section, we obtain an equation for weakly nonlinear gravity-capillary surface waves on an inhomogeneous current:

$$\frac{\partial A}{\partial\tilde{t}} = 2iL\,A + (1-\beta_x)\frac{\partial A}{\partial\tilde{x}} - \beta_y\frac{\partial A}{\partial\tilde{y}} + i\left[(\beta_x - 1)\tilde{k}_{x0} + \beta_y\tilde{k}_{y0} - \tilde{\omega}_0\right]A +$$

$$+ \frac{ic}{2}\tilde{k}_0^{\,2}\sqrt{\tilde{k}_0 + \tilde{T}\tilde{k}_0^{\,3}}\,|A|^2 A - \frac{u}{4}\tilde{k}_0\sqrt{\tilde{k}_0 + \tilde{T}\tilde{k}_0^{\,3}}\,A^2\frac{\partial A^*}{\partial\tilde{x}} + \tag{1.3}$$

$$+ \frac{\nu}{4}\tilde{k}_0\sqrt{\tilde{k}_0 + \tilde{T}\tilde{k}_0^{\,3}}\,|A|^2\frac{\partial A}{\partial\tilde{x}} + i\tilde{k}_0 A\frac{\partial\overline{\Phi}}{\partial\mathbf{r}_{k0}} \quad ,$$

where

$$c = \frac{8+R^2+2R^4}{16(1+R^2)(1-2R^2)}; \qquad u = \frac{(1-R^2)(8+R^2+2R^4)}{16(1-2R^2)(1+R^2)^2} = \frac{1-R^2}{1+R^2}c;$$

$$\nu = \frac{3(4R^8+4R^6-9R^4+R^2-8)}{8(1+R^2)^2(1-2R^2)^2}; \qquad R = \sqrt{\tilde{T}}\tilde{k}_0,$$

$\mathbf{r}_{k0}$ is the direction $\mathbf{k}_0$, and $\dfrac{\partial\overline{\Phi}}{\partial\mathbf{r}_{k0}}$ is determined from a system of equations:

$$\Delta\overline{\Phi} = 0$$

$$\frac{\partial\overline{\Phi}}{\partial z} = \frac{\sqrt{\widetilde{k}_0 + \widetilde{\widetilde{T}}\widetilde{k}_0^{\,3}}}{4}\frac{\partial}{\partial x}\left(|A|^2\right).$$

In the following sections we shall analyze the regions of modulation instability for the equation (1.3) and describe a program for numerical calculations.

2. MODULATION/SELF-FOCUSING INSTABILITY IN A WIDE RANGE OF ANGLES AND FREQUENCIES AS APPLIED TO GRAVITY-CAPPILLARY WAVES

Space-time instability of intense plane waves in dispersive media with cubic nonlinearity is a phenomenon known since the mid-1960s [10-15]. Instability with respect to transverse (spatial) perturbations is called self-focusing [14], while that with respect to longitudinal (temporal) perturbations, is modulation instability [16]. In most cases, self-focusing was considered, as a rule, with respect to perturbations propagating almost collinearly with the main wave, and modulation instability, at frequencies close to the carrier frequency. This permitted in both cases use of the 2nd-order Schrödinger equation. However, this description is inapplicable to perturbations having broad spatial and temporal spectra (such as narrow beams and short pulses or a broadband noise). A more precise but rather complicated theory based on the Hamiltonian description was suggested in [16-18]. This section describes a simple theory of modulation/self-focusing instability in a wide range of angles and frequencies. It is applicable to non-Hamiltonian systems but requires knowledge of dispersion characteristics for waves propagating in a medium. These characteristics can be obtained as a result of test data.

Let a dispersion equation of a given wave mode be known:

$$\omega = F(\mathbf{k}), \tag{2.1}$$

where ω is the frequency, and $\mathbf{k}$ is the wave vector. The wave field A_0 in a medium with such a dispersion relationship can be described by an integral relation [7]:

$$\frac{\partial A_0(\mathbf{r},t)}{\partial t} = \frac{i}{(2\pi)^s}\iint F(\mathbf{k}')\exp\left[-i\mathbf{k}'\mathbf{r} + i\mathbf{k}'\mathbf{r}'\right] A_0(\mathbf{r}',t)\,d\mathbf{k}'d\mathbf{r}', \tag{2.2}$$

where s is the space dimension. Let the equation (2.2) have a solution of the form of a plane wave with amplitude $\overline{A}$:

$$A_0 = \overline{A}\exp\left(i\omega_0 t - i\mathbf{k}_0\mathbf{r}\right),$$
$$\omega_0 = F(\mathbf{k}_0).$$

For brevity, we introduce the operator

$$L(\mathbf{k}_0)\overline{A} = \frac{1}{(2\pi)^s}\iint F(\mathbf{k}_0 + \mathbf{k}')\exp\left[-i\mathbf{k}'\mathbf{r} + i\mathbf{k}'\mathbf{r}'\right]\overline{A}(\mathbf{r}')\,d\mathbf{k}'d\mathbf{r}'$$

and write down an equation for $\overline{A}$ in the form

$$\frac{\partial\overline{A}}{\partial t} = iL(\mathbf{k}_0)\overline{A} - i\omega_0\overline{A}. \tag{2.3}$$

Now we supplement the latter equation by the nonlinear term, which is, as known, is proportional to $|\overline{A}|^2\overline{A}$. The coefficient at this nonlinear term is chosen according to the nonlinear

dispersion relation for a plane wave. The amplitude is normalized in such a way that the resulting nonlinear equation has the form

$$\frac{\partial \overline{A}}{\partial t} = iL(\mathbf{k}_0)\overline{A} - i\omega_0 \overline{A} + \frac{i\varepsilon' \left|\overline{A}\right|^2 \overline{A}}{2} \quad , \tag{2.4}$$

where ε' is the nonlinearity coefficient.

In the framework of the nonlinear equation (2.4) we investigate the stability of its plane-wave solution:

$$\overline{A} = B\exp(i\Omega t),$$

where $\Omega = \dfrac{|B|^2}{2}$ is the nonlinear frequency shift (detuning). We consider a perturbed solution in the form

$$\overline{A} = \left[B + \alpha\right] \exp(i\Omega t),$$

where α is small. Assuming that α has the form:

$$\alpha = \alpha_0(t)\exp(-i\mathbf{kr}) + \beta_0(t)\exp(i\mathbf{kr}), \tag{2.5}$$

we obtain for perturbation amplitudes a pair of linear equations with constant coefficients

$$\frac{d\alpha_0}{dt} = iL(\mathbf{k}_0 + \mathbf{k})\alpha_0 - i\omega_0\alpha_0 + \frac{i\omega_0\varepsilon'|B|^2}{2}\alpha_0 + \frac{i\omega_0\varepsilon'|B|^2}{2}\beta_0^*, \tag{2.6}$$

$$\frac{d\beta_0^*}{dt} = -iL(\mathbf{k}_0 - \mathbf{k})\beta_0^* + i\omega_0\beta_0^* - \frac{i\omega_0\varepsilon'|B|^2}{2}\beta_0^* - \frac{i\omega_0\varepsilon'|B|^2}{2}\alpha_0, \tag{2.7}$$

Upon the assumption that $a_0 \sim \beta_0 \sim \exp\left[\dfrac{h}{\omega_0}t\right]$, we have for the growth rate (increment) normalized to the frequency ω_0:

$$h = i\frac{\omega_+ - \omega_-}{2} + \frac{1}{2}\sqrt{\left|\varepsilon'^2 B^4\right| - \left(\omega_+ + \omega_- - 2 + \varepsilon'|B|^2\right)^2}$$

where $\omega_+ = \dfrac{F(\mathbf{k}_0 + \mathbf{k})}{\omega_0}$ is a linear detuning of one of the perturbation spectral components and $\omega_- = \dfrac{F(\mathbf{k}_0 - \mathbf{k})}{\omega_0}$ is the one for the other perturbation component. It is evident that for isotropic media the vector $\mathbf{k}_0$ should be directed along the x-axis.

The boundaries of the instability region on the plane of the wave vector components are determined by the conditions:

$$\omega_+ + \omega_- = 2, \tag{2.8}$$

$$2\varepsilon'|B_0|^2 - 2 + \omega_+ + \omega_- = 0 \tag{2.9}$$

The first of them is determined by linear dispersion. It describes a real surface if the dispersion curve is convex. In this case instability takes place both for the focusing nonlinearity ($\varepsilon' > 0$) and the defocusing nonlinearity ($\varepsilon' < 0$), but the instability regions for different signs lie on the opposite sides of the surface (2.8). If the dispersion curve is concave, the surface (2.9) degenerates into one point, $\omega = F(\mathbf{k})$. In this case the instability takes place only for a positive value ε'.

For potential gravity waves on the liquid surface,

$$\omega = \sqrt{g|k_0|} = \sqrt{g\left(k_{x0}^{\,2} + k_{y0}^{\,2}\right)^{1/2}},$$

where g is the gravity acceleration, and k_x and k_y are wave vector components in the plane. In this case equation (2.4) is written as:

$$\frac{\partial \overline{A}}{\partial t} = iL(\mathbf{k}_0)\overline{A} - i\omega_0 \overline{A} + \frac{i\omega_0}{2}\left|\mathbf{k}_0 \overline{A}\right|^2 \overline{A}, \tag{2.10}$$

where $\overline{A}$ is the wave amplitude. When investigating the instability in Eq. (2.10), we pass over to the dimensionless variables $t_{dl} = \frac{\omega_0 t}{2}$, $x_{dl} = |\mathbf{k}_0| x$, $y_{dl} = |\mathbf{k}_0| y$, $z_{dl} = |\mathbf{k}_0| z$, $A = 2|\mathbf{k}_0|\overline{A}$.[1]

Omitting below the subscript "*dl*", we rewrite equation (2.10) in the form:

$$\frac{\partial A}{\partial t} = \frac{2i}{\omega_0} L(\mathbf{k}_0) A - 2iA + \frac{i}{4}|A|^2 A, \tag{2.11}$$

For the normalized increment of a perturbation:

$$h_d = \frac{1}{2}\mathrm{Re}\sqrt{\frac{A^4}{4} - \left\{2\left[\left(1+\tilde{k}_x\right)^2 + \tilde{k}_y^{\,2}\right]^{1/4} + 2\left[\left(1-\tilde{k}_x\right)^2 + \tilde{k}_y^{\,2}\right]^{1/4} - 4 + \frac{A^2}{2}\right\}^2}, \tag{2.12}$$

where $\tilde{k}_x = \frac{k_x}{k_0}$, $\tilde{k}_y = \frac{k_y}{k_0}$. Note that the non-breaking gravity waves exist at $A \le 0.88718$. The region of the nonzero increment for $A = 0.15$ is shown in Fig. 2.1. In the plane $\left(\tilde{k}_x, \tilde{k}_y\right)$ the instability region is butterfly shaped and is adjacent to the known curve of four-wave synchronism following from (2.8). The points $\tilde{k}_x = \pm 1$, $\tilde{k}_y = 0$ lying in the middle of the loops are always stable. The maximal (and constant for a given amplitude) increment value is achieved under the condition

$$4 - 2\left[\left(1+\tilde{k}_x\right)^2 + \tilde{k}_y^{\,2}\right]^{1/4} - 2\left[\left(1-\tilde{k}_x\right)^2 + \tilde{k}_y^{\,2}\right]^{1/4} = \frac{A^2}{2},$$

which is also fulfilled at a butterfly shaped curve lying close to the line of four-wave synchronism. At small detunings, when $\tilde{k}_x$, $\tilde{k}_y \ll 1$, the main wave is unstable only with respect to waves having a nonzero component $\tilde{k}_x$, i.e., modulation instability takes place. For comparison, the instability region obtained in the parabolic approximation of the dispersion dependence (2.1) for the same wave amplitude is shown in Fig. 2.2. In this case Equation (2.10) turns into the well-known nonlinear Schrödinger equation:

$$\frac{\partial A}{\partial t} = \frac{i}{4}\frac{\partial^2 A}{\partial x^2} - \frac{i}{2}\frac{\partial^2 A}{\partial y^2} + \frac{i}{4}|A|^2 A. \tag{2.13}$$

The corresponding curve has asymptotes approaching infinity at angles $\varphi \sim \pm \arctan\sqrt{2}$, and the amplitude of the increment does not decrease when going to infinity along the line $\tilde{k}_x + \sqrt{2}\tilde{k}_y = A^2$. On the contrary, the exact linear dispersion considered above results in a limitation of the instability region but does not change the maximum increment value.

We have not considered above the effect of nonlinearity dispersion. Now we shall introduce it following [8,9]. We add to equation (2.3) a nonlinear term with allowance for its dispersion. As a result we obtain the following set of equations to describe the wave envelope:

---

[1] The latter substitution means that we neglect the dependence of nonlinear parameters on wave vectors of the waves participating in the process, i.e. the dispersion nonlinearity. This factor will be taken into account in the second chapter.

$$\frac{\partial A}{\partial t}=\frac{2i}{\omega_0}L(\mathbf{k}_0)A-2iA+\frac{i}{4}|A|^2A-\frac{1}{8}A^2A^*{}_x-\frac{3}{4}|A|^2A_x+i\Phi_xA, \tag{2.14}$$

and an averaged potential Φ:

$$\Delta\Phi=0. \tag{2.15}$$

The potential should tend to zero at large depths (at $z\to-\infty$) and also satisfy the condition

$$\Phi_z=\frac{1}{4}|A^2|_x$$

on the liquid surface (at $z=0$). Only the terms cubic in $|A|$ are kept in (2.14). Using the method described above, we obtain the following expression for the perturbation increment normalized to the carrier frequency:

$$h_d=\frac{1}{2}\mathrm{Re}\sqrt{\frac{|A^4|}{4}\left[\left(1-\frac{\tilde{k}_x{}^2}{K}\right)^2-\left(\frac{\tilde{k}_x}{2}\right)^2\right]-\left[2\omega_++2\omega_--4+\frac{|A^2|}{2}\left(1-\frac{\tilde{k}_x{}^2}{K}\right)\right]^2}, \tag{2.16}$$

where $K=\sqrt{\tilde{k}_x{}^2+\tilde{k}_y{}^2}$, $\omega_+=\sqrt{\sqrt{(1+\tilde{k}_x)^2+\tilde{k}^2{}_y}}$, and $\omega_-=\sqrt{\sqrt{(1-\tilde{k}_x)^2+\tilde{k}^2{}_y}}$. Note that the presence of current (a term with Φ_x in [2.14]) leads to an effective decrease of the wave amplitude (namely, it changes $|A^2|$ to $|A^2|\left(1-\frac{\tilde{k}^2{}_x}{K}\right)$ in the expression (2.16) as compared to (2.12)). This amplitude decrease leads to a narrowing of the unstable region and a decrease of the increment inside it. The term $\frac{A^2A^*{}_x}{8}$ leads to the occurrence of a correction $\sim\frac{\tilde{k}^2{}_x}{4}$ in (2.16) and to a decrease of the increment at strong detuning (which is not mentioned in [8,9]). The instability regions in the plane $\left(\tilde{k}_x,\ \tilde{k}_y\right)$ for $A=0.15$ are shown in Fig. 2.3. It follows from comparison of Figs. 2.1 and 2.3 which differ only by the role of nonlinear dispersion that the latter decreases increments, turning it to zero for large detunings. Comparison with numerical results given in [19] obtained using the theory of [16,17], shows their agreement with those obtained above. The instability region narrows due to nonlinear dispersion. There is a difference at amplitudes close to the limiting ones ($A\approx0.8$). According to the theory (see [16]), at such amplitudes the waves with small detuning, $\tilde{k}_x\ll1$, become stable, whereas according to (2.12) they remain unstable. This is due to more accurate and more complicated expressions for nonlinear dispersion in [16] and [19] as compared to [8].

For *gravity-capillary waves* on the liquid surface, when surface tension is taken into account, the dispersion equation has the form:

$$\omega=\sqrt{g|\mathbf{k}_0|\left(1+\overline{T}|\mathbf{k}_0|^2\right)},$$

where $\overline{T}=\frac{T}{g\rho}$, T is the surface tension, and ρ is the liquid density. We introduce a dimensionless coefficient $\widetilde{T}=\frac{T_ng}{16V_0{}^4}$, where $V_0=\left(\frac{g^2}{16k_0{}^2}\right)^{1/4}$ is the group velocity of gravity waves with the same wave vector modulus, and $T_n=\frac{\overline{T}}{\rho}$. At first we consider a case without nonlinear dispersion. The equation for evolution of the wave packet envelope in dimensionless variables has the form:

$$\frac{\partial A}{\partial t}=\frac{2i}{\omega_0}\tilde{L}(\mathbf{k}_0)A-2i\tilde{\omega}A+\frac{ic\tilde{\omega}}{2}|A|^2A, \qquad (2.17)$$

where

$$\tilde{L}(\mathbf{k}_0)A=\frac{1}{(2\pi)^s}\iint\tilde{F}(\mathbf{k}_0+\mathbf{k}')\exp[-i\mathbf{k}'\mathbf{r}+i\mathbf{k}'\mathbf{r}']\,A(\mathbf{r}')\,d\mathbf{k}'d\mathbf{r}',$$

$$F(\mathbf{k}_0+\mathbf{k})=\omega_0\sqrt{\sqrt{\left(1+\tilde{k}_x\right)^2+\tilde{k}_y^{\,2}}\left[1+\tilde{T}\left(\left(1+\tilde{k}_x\right)^2+\tilde{k}_y^{\,2}\right)\right]}, \qquad \tilde{\omega}=\sqrt{1+\tilde{T}}, \qquad c=\frac{1}{2}q,$$

$$q=\frac{1+\frac{R^2}{8}+\frac{R^4}{4}}{\left(1+R^2\right)\left(1-2R^2\right)}, \quad R=\sqrt{\tilde{T}}.$$

Equation (2.17) has a limited applicability region. It describes the self-action of gravity-capillary waves, and, in particular, modulation instability. The latter can prevail only when a more rapid parametric "decay" instability is absent. A necessary condition for the occurrence of the latter is given by the equalities:

$$\omega_n=\omega_1+\omega_2, \qquad (2.18)$$

$$\mathbf{k}_n(\omega_n)=\mathbf{k}_1(\omega_1)+\mathbf{k}_2(\omega_2), \qquad (2.19)$$

where ω_n and $\mathbf{k}_n(\omega_n)$ are the frequency and wave vector of a strong wave (pump wave), $\omega_{1,2}$ and $\mathbf{k}_{1,2}(\omega_{1,2})$ are the frequencies and wave vectors of perturbations. The corresponding increment has the order $h\sim\omega_n k_n\overline{A}$ as distinct from modulation instability for which the conditions

$$2\omega_n=\omega_1+\omega_2, \qquad (2.20)$$

$$2\mathbf{k}_n(\omega_n)=\mathbf{k}_1(\omega_1)+\mathbf{k}_2(\omega_2), \qquad (2.21)$$

should be fulfilled. The increment of this instability, h, has the order $h\sim\omega_n\left(k_n\overline{A}\right)^2$. For a collinear interaction, the equalities (2.18) and (2.19) can be fulfilled for rather short waves under the condition (written in our notations):

$$R^2>\frac{1}{2}. \qquad (2.22)$$

If (2.22) is not fulfilled, only the modulation or elf-focusing instability can take place. Its increment is given by the formula:

$$h=\frac{\tilde{\omega}}{2}\mathrm{Re}\sqrt{\frac{q^2A^4}{4}-\left\{\frac{2\Omega_+}{\tilde{\omega}}+\frac{2\Omega_-}{\tilde{\omega}}-4+\frac{qA^2}{2}\right\}^2}, \qquad (2.23)$$

where $\Omega_+=\sqrt{\sqrt{(1+\tilde{k}_x)^2+\tilde{k}_y^{\,2}}+\tilde{T}\left[\sqrt{(1+\tilde{k}_x)^2+\tilde{k}_y^{\,2}}\right]^3}$,

$$\Omega_-=\sqrt{\sqrt{(1-\tilde{k}_x)^2+\tilde{k}_y^{\,2}}+\tilde{T}\left[\sqrt{(1-\tilde{k}_x)^2+\tilde{k}_y^{\,2}}\right]^3}.$$

For example, for $A=0.15$ at $\overline{T}=0.00007m^3/s^2$, $g=9.81m/s^2$ and $V_0=1m/s$, the region of a nonzero increment does not differ practically from that shown in Fig. 2.1, because the surface tension does not affect longer waves. Its influence begins at $V_0\sim0.10\div0.15m/s$. The instability region in the plane $\left(\tilde{k}_x,\,\tilde{k}_y\right)$ at the same value of the parameter $\tilde{T}$ and $V_0=0.15m/s$, $V_0=0.12m/s$, is exhibited in Figs. 2.4 and 2.5, respectively. The instability region

narrows (Fig. 2.4) and then disappears close to $\tilde{k}_x \approx 0$. The stability boundary can be determined from the following consideration. We write down a parabolic approximation of equation (2.17). It has the form:

$$\frac{\partial A}{\partial t} = \frac{i}{4}\left(\frac{(1+3\tilde{T})^2}{(1+\tilde{T})^{3/2}} - \frac{12\tilde{T}}{(1+\tilde{T})^{1/2}}\right)\frac{\partial^2 A}{\partial x^2} - \frac{i(1+3\tilde{T})}{2(1+\tilde{T})^{1/2}}\frac{\partial^2 A}{\partial y^2} + \frac{ic(1+\tilde{T})^{1/2}}{2}|A|^2 A. \quad (2.24)$$

The instability vanishes when the coefficient at the second derivative with respect to x becomes zero at $V_0 = 0.13 m/s$. When calculating instability increment using Equation (2.24), one can see that it really becomes zero in a wide range of detunings, as soon as the coefficient at the second derivative changes the sign. A more precise analysis using Equation (2.17) shows that the region of the nonzero increment first moves aside from the zero point and then, at the velocity $V_0 = 0.101 m/s$, the whole region becomes stable. At further decrease of the parameter V_0 up to $V_0 = 0.0961 m/s$, the modulation/self-focusing instability occurs again. Now it acquires the character of a "collapse" when the instability regions have the shape of ellipses. They are shown in Fig. 2.6 for $V_0 = 0.08 m/s$. It should be noted, however, that in the "collapse" region there exist stronger instabilities [17] that are not described by the equation (2.17).

For the gravity-capillary waves with account for the full linear dispersion and for nonlinear dispersion according to [8,9], the corresponding equation has the form

$$\frac{\partial A}{\partial t} = \frac{2i}{\omega_0}\tilde{L}(\mathbf{k}_0)A - 2i\tilde{\omega}A + \frac{ic\tilde{\omega}}{2}|A|^2 A - \frac{\bar{u}q\tilde{\omega}}{8}A^2 A^*{}_x - \frac{3\bar{v}\tilde{\omega}}{4}|A|^2 A_x + iA\Phi_x,$$

where the potential function satisfies Equation (2.15) with the boundary condition on the liquid surface ($z = 0$):

$$\Phi_z = \frac{\tilde{\omega}}{4}|A^2|_x,$$

and $\bar{u} = \dfrac{1-R^2}{1+R^2}$, $\bar{v} = \dfrac{1 - \frac{R^2}{8} + \frac{9R^4}{8} - \frac{R^6}{2} + \frac{R^8}{2}}{(1+R^2)^2(1-2R^2)^2}$. In this case the increment reads as follows:

$$h_d = \frac{\tilde{\omega}}{2}\mathrm{Re}\sqrt{\frac{|A^4|}{4}\left[\left(q - \frac{\tilde{k}_x^2}{K}\right)^2 - \left(\frac{\tilde{k}_x q\bar{u}}{2}\right)^2\right] - \left\{\frac{2\Omega_+}{\tilde{\omega}} + \frac{2\Omega_-}{\tilde{\omega}} - 4 + \frac{A^2}{2}\left(q - \frac{\tilde{k}_x^2}{K}\right)\right\}^2}.$$

The occurrence of nonlinear dispersion in gravity-capillary waves as well as in purely gravity waves leads to the suppression of instability at large detuning. This is seen from comparison of instability diagrams in the plane $(\tilde{k}_x, \tilde{k}_y)$ at $A = 0.15$ and $U_0 = 0.12 m/s$, with taking into account nonlinear dispersion (Fig. 2.7) and without it (Fig. 2.5). In a "collapse"- type region the occurrence of nonlinear dispersion leads to the narrowing of the unstable region and decreasing of the increment in it. The latter statement is valid for both gravity and gravity-capillary waves.

3. METHOD OF NUMERICAL CALCULATION

In this section, a program for computing the transformation of nonlinear surface waves is briefly outlined. Note that in the second chapter a later modification of this program is used which includes the nonlinear dispersion.

The equation describing the evolution of the wave envelope has the following form in dimensionless variables:

$$\frac{\partial A}{\partial t} = 2i\tilde{L}(\mathbf{k}_0)A + (1-\beta_x)\frac{\partial A}{\partial x} - \beta_y \frac{\partial A}{\partial y} + i\left[(\beta_x - 1)k_{x0} + \beta_y k_{y0} - \omega_0\right]A + \frac{ic\omega}{2}|A|^2 A \qquad (3.1)$$

where $\tilde{L}(\mathbf{k}_0)A = \frac{1}{(2\pi)^2}\iint F(\mathbf{k}_0 + \mathbf{k}')\exp\left[-i\mathbf{k}'\mathbf{r} + i\mathbf{k}'\mathbf{r}'\right]A(\mathbf{r}')d\mathbf{k}'d\mathbf{r}'$,

$F(\mathbf{k}_0 + \mathbf{k}') = \sqrt{\sqrt{(k_{x0}+k_x')^2 + (k_{y0}+k_y')^2}\left[1 + \tilde{T}\left\{(k_{x0}+k_x')^2 + (k_{y0}+k_y')^2\right\}\right]}$, $k_0 = \sqrt{{k_{x0}}^2 + {k_{y0}}^2}$

$\omega_0 = 2\sqrt{k_0\left(1+\tilde{T}{k_0}^2\right)} - k_{x0}$, $\omega = {k_0}^2\sqrt{k_0\left(1+\tilde{T}{k_0}^2\right)}$, $c = \frac{8+R^2+2R^4}{16(1+R^2)(1-2R^2)}$, $R = \sqrt{\tilde{T}}k_0$,

$\tilde{T} = \frac{Tg}{16{U_0}^4}$, $T, g, U_0, k_{x0}, k_{y0}$ are numerical parameters. It is assumed that at the initial moment, $t = 0$, the wave amplitude does not depend on the coordinates (x, y) and has an amplitude A_0, whereas β_x, β_y are in the general case the functions of x, y. These functions can have different forms depending on the specifics of a problem. Equation (3.1) was solved in the square $(X_{in}, X_{fin}; Y_{in}, Y_{fin})$, up to a time $t_{\max}$. The splitting method was used when solving the problem (see Fig. 3.1). At the first step, Δt, an equation

$$\frac{\partial A}{\partial t} = 2i\tilde{L}(\mathbf{k}_0)A$$

was solved with the assigned initial conditions; thereby, the fast two-dimensional Fourier transform was twice used. The number of transverse points, $NF \times NF$, could vary up to 300×300 for a two-dimensional problem, whereas the number of points $NF1$ could reach 30000 for a one-dimensional problem. At the square boundaries, $X_{in}, X_{fin}; Y_{in}, Y_{fin}$, periodicity conditions were imposed.

At the second step, at each point of the plane (x, y), a set of equations

$$\frac{\partial A}{\partial t} = (1-\beta_x)\frac{\partial A}{\partial x} - \beta_y \frac{\partial A}{\partial y} + i\left[(\beta_x - 1)\tilde{k}_{x0} + \beta_y \tilde{k}_{y0} - \tilde{\omega}_0\right]A + \frac{ic\tilde{\omega}}{2}|A|^2 A,$$

was solved at an interval Δt by splitting this system into real and imaginary parts and using various versions of the modified Runge-Kutta method. As the initial condition, we used a function obtained at the previous stage, with calculation of derivatives with respect to coordinates x, y and employment of fast Fourier transform. Values of the step Δt could vary within wide limits. The obtained function was assumed to be the initial one for the next step.

Features of the program.

Minimal requirements for program operation are: Windows 95, Pentium 90, optoelectronic storage 24 Mb, a free place on a hard disk of 50 Mb, monitor resolution 800 x 600 with 16-bit high color.

Two groups of parameters are placed on the panel. The upper group consists of independent parameters of the problem. The lower has parameters assigned for investigation and those controlling the observation method and the research process. $X_{in}, X_{fin}; Y_{in}, Y_{fin}$ denote the boundaries of the field region; S_{in}, S_{fin} enables one to set fixed boundaries of processing review regions.

The main menu contains both conventional, standard items and those specialized for this program. The program "File Menu" enables one to record and read text files in the text format .txt, calculation results (field structure matrices), and parameters for which they are obtained, in the

special format, .mtr, and the read-out regions with structures, plots, and a panel of parameters with values of the latter in the graphic format .bmp.

The menu "Calculations" enables one to start calculations and monitor the process. In the same menu a modification of the solved problem can be chosen (an equation with taking into account full linear dispersion or dispersion in the parabolic approximation; equation for gravity waves or for gravity-capillary waves), the choice of a FFT library (a standard or a newer one). Then we indicate if we cut a spectrum around the circle inside the square of the spectrum region involved in calculations.

After starting the program in the operating region there are two squares prepared for graphical output of data. The left square is designed for the field structure image, the right one for maximum and minimum of the field, their difference and the control integral of energy.

Menu "Readout" determines which field structures we observed in calculation. The structure can be represented both in a black-and-white variant (with the intensity proportional to the amplitude or phase of the field), and in a color variant (the values are represented by colors from white to black through a visible spectrum range according to the wavelength growth).

It is possible to copy the exchange buffer in the graphical format both of the entire operating region including values of parameters and of any part preliminarily singled out by the left click of the "mouse". It is also possible to store the required part in the file of .bmp format (correct record in file occurs when using 16-bit color resolution and higher).

One can temporarily stop calculations at any instant for analysis and then continue (menu item "Calculation"). One can also terminate them and start again for other parameters, having previously renewed all internal parameters and values by choosing the item "New" of menu "File."

Menu "Processing" permits one to choose the resulting curves. For analysis of the results, these curves can be presented both in linear and logarithmic scales. Marks on axes can be made in numbers of calculation points and dimensional values.

4. MEASUREMENTS OF PARAMETERS OF SURFACE WAVES PRODUCED BY A WAVE MAKER IN THE ABSENCE OF CURRENTS. SPATIAL DISTRIBUTIONS OF WATER SURFACE ELEVATION AND SLOPE.

As a preparation for experiments on surface wave transformation due to the motion of the sphere, at this stage we studied characteristics of free surface waves generated by a wave maker. The work was performed in a large thermostratified tank of IAP. After an upgrading of the wave maker, we were able to work in a higher frequency range of surface waves than before. Namely, a relatively homogeneous train of surface waves was created at frequencies of up to 3.5 Hz. To measure surface wave parameters, we used two different systems: ultrasonic sensors of water surface elevation and a video complex for measuring water surface slope. First, we briefly describe these systems.

4.1. Ultrasonic sensors of surface water elevation.

For remote measurements of surface wave parameters we used a four-channel ultrasonic gauge of surface motions working in a continuous regime. A phase method was employed in this gauge. Its distinctive feature is automatic confinement of operating range of the phase detector within the linear part of its phase characteristic. A time-dependent value of the voltage amplitude at the output is proportional to the distance between the sensor and the reflecting surface. The device consists of an electronic unit, four sensors connected to it with a 5-m-long cable, and a 20-m-long cable for ADC-PC connection. It has the following technical specifications:

Frequency of generated ultrasonic wave: 30 kHz.

Amplitude of measured movements: ± 35 mm.

Frequency range of measured movements: 0-30 Hz.
Distance from sensor to water surface: 70 mm.
Voltage at output: not more than 3.5 V.

It is possible to measure movements with amplitudes from 0.1 mm and over, with a signal-to-noise ratio of not less than 40 dB. Positioning of sensors depends on measurements performed (towing trolley, rack, etc., with a possibility of varying coordinates in both X and Y horizontal directions).

A signal (voltage variation) from the ultrasonic gauge enters an input-output board (ACD-DAC) of series L-card (L-153, 154, 164) mounted in the PC. Specially designed software was employed in the measuring systems of the tank. ADC boards have the following technical specifications:

Number of channels: differential 16, with common ground 32.
Word length: 12 bit.
Conversion time: 10 microsecond.
Input signal range: ±(10.24, 5.12, 1.024) V.
Maximal conversion frequency: 50 kHz.
Signal transmission band: not more than 250 kHz.
Input resistance: 2 MOhm.

To determine spatial distribution of the surface wave amplitude, the sensors were placed across the tank at different distances from the tank axis for each realization. As a result, spatial resolution of 50 mm was achieved.

4.2. Video system for measuring water surface slope.

The system is based on an analog-digital video complex for optical observation and registration of processes on the liquid surface. The system allows one to perform remote diagnostics of a rather large spatial region, of about 1.5 x 1.5 m^2 to determine surface wave parameters with digital recording of an analog video signal for further processing of video images. The system consists of an analog video camera placed above the water surface, diffraction grates (ruled with black, 50-mm-spaced strips in X,Y coordinates divided by white shields) placed on the tank bottom, a system of uniform illumination of grates (by underwater searchlights), and a special board of input and digitization of an analog video signal. The board is placed in a PC.

To obtain a video signal we used a Bishke CCD-30LP compact black-and-white TV video camera based on CCD 1/3" matrix with 300 000 elements with resolution of 384 TVL and minimum sensitivity 0.1 lx at the object, an automatic electron shutter and 4(6) mm lens without diaphragm control. A video signal from the camera enters a board of video image trapping, miro-VIDEO DC20. The board and appropriate hardware and software facilities of the computer enables one to trap a video signal with maximum velocity of data flow for this board, about 3100 kb/s with resolution 768 x 576 lines for M-JPG compression of a video signal 7:1 or 640 x 480 lines for compression 5.5:1, 60 fields/s, 24-bit color with 100% absence of frame skip at recording AVI-file on PC hard disk. This quality of video image recording corresponds to that of broadcast quality.

When surface waves pass images of the grate line deviate from the initial position (regular at unperturbed liquid surface). An example of the image of the grate without a surface wave and with it (frequency 3 Hz) is shown in Fig. 4.1. Comparison of coordinates of grate node images with their values in the absence of surface waves permits one to determine both projections of water surface slope. A specially designed program packet enables one to automatically define coordinates of grate nodes and interpolate values of water surface slopes to a regular grate. Further processing including in particular, high-frequency filtration, permits one to retrieve distribution of surface wave amplitude in a tank.

The use of a video complex enables one to register rapid surface wave transformations.

4.3. Measurements of surface wave parameters.

Measurements were made for three fixed frequencies of the wave maker, f: 2.5 Hz, 3 Hz, and 3.4 Hz in the 0.2 – 2 mm range of generated surface wave amplitudes. The efficiency of surface wave generation abruptly falls with the frequency increase, which is seen well in Fig. 4.2, where the data from ultrasonic sensors are shown. The oscillation amplitude of the cylindrical wave maker is the same at all frequencies. The time of the wave maker operation t is shown on the horizontal axis, the distance Y to the longitudinal axis of the tank is shown on the vertical axis. Color is used to show the surface wave amplitude in mm according to the scale on the right-hand side of each figure. The distance X from the wave maker to the sensor line is 6 m. In future experiments with a sphere, approximately the same time interval will be chosen, since at smaller time intervals transition processes are observed that are related to the onset of surface wave generation, and at large time intervals the influence of a weak wave reflected from the wave absorber at the opposite end of the tank can be felt. This can be seen from Fig. 4.3, where we show the surface wave variation during the entire time of the experiment, corresponding to Fig. 4.2. It is seen from the figure that the surface wave amplitude changes considerably during this experiment (120 s). But the characteristic time of the experiments on surface wave transformation by a current around the sphere will not exceed 20 s [5], and we may choose a time interval in which the background field does not significantly change its structure.

The data corresponding to Fig. 4.2 but obtained with the use of the video complex are shown in Fig. 4.4. Data on surface slope amplitude were recalculated in terms of elevation amplitude for linear surface waves:

$$a_{el} = \frac{a_{sl} g}{4\pi^2 f^2}.$$

Figure 4.4 was obtained as a result of averaging of surface wave amplitude from all transversal lines of the grate on the underwater board. It is assumed that the amplitude of surface waves during their propagation along the board changes slowly and is transmitted with the wave group velocity. Since the lines on the board are at different distances from the wave maker, we introduce for the corresponding data the time shift equal to the distance between the lines divided by the surface wave group velocity. It is seen from Figs. 4.2-4.4 that there is a transverse inhomogeneity of surface wave amplitude which, as shown below, increases with the amplitude increase. Such a transverse modulation may be caused by both bending vibrations of the wave maker cylinder and the growth of the transverse waves in the tank [20]. Comparison of the data for $X = 6$ m and $X = 9$ m performed below shows that the latter reason plays the main role.

Figures 4.5 and 4.6 deal with the distribution of surface wave amplitude at a fixed frequency, 3 Hz, but with different amplitudes of the wave maker oscillations (Fig. 4.5 - data from the ultrasonic sensors, Fig. 4.6 – from the video system), at $X = 6$ m. With the increase of the surface wave amplitude at a fixed X and f, its variability increases. This is seen well from Table 1, where average values of amplitude $\overline{A}$, amplitude deviation variance δ^2 and the value of $\delta^2 / \overline{A}$ are given for all experiments.

Table 1.

Experimental series	Date	$\overline{A}$	δ^2	$\delta^2/\overline{A}$
Ultrasonic sensors:				
a4 x6 f3.0	28.03.00	0.479	0.0080	0.00166
a5 x6 f3.0	30.03.00	0.786	0.0334	0.04245
a6 x6 f3.0	31.03.00	1.285	0.0804	0.06255
a4 x6 f2.5	28.03.00	0.892	0.0819	0.09187
a4 x6 f3.4	28.03.00	0.212	0.0020	0.00923
a6 x6 f3.4	31.03.00	0.409	0.0254	0.06197
a8 x6 f2.5	31.03.00	1.826	0.2004	0.10975
Video system:				
a4 x6 f3.0	28.03.00	0.608	0.0212	0.03487
a5 x6 f3.0	30.03.00	0.932	0.0334	0.03584
a6 x6 f3.0	31.03.00	1.592	0.1061	0.06665
a4 x6 f2.5	28.03.00	1.073	0.0368	0.03606
a4 x6 f3.4	28.03.00	0.301	0.0076	0.02467
a6 x6 f3.4	31.03.00	0.580	0.0215	0.03703
a8 x6 f2.5	31.03.00	1.501	0.1276	0.08496
a4 x6 f2.5	24.03.00	1.492	0.0818	0.05483
a4 x6 f3.0	24.03.00	0.741	0.0287	0.03866
a4 x6 f3.4	24.03.00	0.372	0.0092	0.02466
a4 x9 f2.5	24.03.00	1.036	0.0873	0.08427
a4 x9 f3.0	24.03.00	0.260	0.0165	0.06329

Here the following summations were used:

$$\overline{A} = \frac{1}{NM}\sum_{i=1}^{N}\sum_{j=1}^{M} A_{ij}\,, \qquad \delta^2 = \frac{1}{NM-1}\sum_{i=1}^{N}\sum_{j=1}^{M}(A_{ij}-\overline{A})^2$$

These values were calculated for the entire range of coordinate Y in the measurement region (in the time intervals shown in Figs. 4.2, 4.4-4.6, and 4.8-4.10). The first column gives the conditions of the experiment performance: the number after "a" is the amplitude of cylinder oscillation in mm; the number after "x" is the distance from the wave maker to the ultrasonic sensor line in meters; the number after "f" is the frequency of wave maker oscillations in Hz.

Variations of surface wave amplitude with the increase of X are presented in Figs. 4.7-4.10. Data of ultrasonic measurements at $Y = 0$ and $Y = 35$ cm are given in Fig. 4.7 for $X = 6$ m (Fig. 4.7a) and $X = 9$ m (Fig. 4.7b). Estimates of the surface wave damping rate are made based on these data. The average amplitude of surface waves in time intervals marked in Fig. 4.7a by the gray color (40-60 s at a frequency of 2.5 Hz and 60-80 s at frequencies of 3 Hz and 3.4 Hz), is calculated. /*Then the average amplitude is calculated also during 20 s using Figure 4.7b, but the time interval is shifted by the time equal to 3 m/V_{gr}, where V_{gr} is the surface wave group velocity. At a frequency of 2.5 Hz the amplitude decreases, on average, by about 1.3 times, at 3Hz, 2.9 times, and at 3.4 Hz, 6.8 times. This corresponds to the following values of damping rate, γ : $\gamma = 0.027\ s^{-1}$ at

f=2.5 Hz, γ = 0.092 s^{-1} at f=3 Hz and γ = 0.147 s^{-1} at f=3.4 Hz. Theoretical estimates show that the wave damping rate due to the influence of the tank walls and bottom is γ_b = 0.002 s^{-1} for the frequencies mentioned above; the surface wave damping coefficient for deep water in the case of a clean surface is γ_v = 0.002 s^{-1} at f=2.5 Hz, γ_v = 0.003 s^{-1} at f=3 Hz and γ_v = 0.006 s^{-1} at f=3.4 Hz [21], whereas for the surface covered with a non-stretchable surface-active film, the damping coefficient is γ_f = 0.040 s^{-1} at f=2.5 Hz, γ_f = 0.063 s^{-1} at f=3 Hz and γ_f = 0.087 s^{-1} at f=3.4 Hz [22]. In the case of the surface covered with an elastic film, the damping coefficient can be twice as large as γ_f [23]. Therefore, under our experimental conditions surface wave damping is most probably caused by the influence of a surface-active film.

Gray color areas in Fig. 4.7 were used to indicate measurement time intervals for the video system (Figs. 4.8-4.10). Figures 4.8 and 4.9 demonstrate that with the increase of X the surface wave amplitude decreases and the transverse field inhomogeneity increases. It can also be seen also from Table 1 that the value of $\overline{A}$ decreases and the value of $\delta^2/\overline{A}$ caused evidently by the nonlinearity of the surface waves increases at the fixed f. These results are analogous to those obtained in [20]. As in [20], a slight frequency downshift is observed.

The dependence of wave parameters on the state of the water surface should also be mentioned. It is not possible to completely remove a film from the surface and, moreover, film characteristics could vary from day to day. This leads to different distributions of wave amplitude during various days under the same generation conditions. Comparison of Figs. 4.4a and 4.8a, or 4.4c and 4.10 shows that the value of $\overline{A}$ and the distribution of surface wave amplitude across the tank also vary. Thus, the series of experiments, the results of which are planned to be compared, should be performed in one day.

The range of surface wave amplitudes in which the video complex can be used was determined. Its lower limit corresponds to the case when the video camera records node image shift by only 1-2 points. The upper limit corresponds to the case when images of various lines on a board begin to merge. It was found experimentally that for this system, a minimum possible amplitude is about 0.3 mm, and maximum about 1.5 mm.

As seen from Table 1, the values of $\overline{A}$ measured by the video system and ultrasonic meter, differ slightly. This is presumably due to a difference in the widths of areas used for calculation of $\overline{A}$ for these two systems (indeed, the distribution of surface wave amplitude is non-uniform along Y). In the planned experiments with a moving sphere, this discrepancy in $\overline{A}$ will not strongly influence experimental results. Indeed, the variability of $\overline{A}$ does not exceed 10% for experimental realizations obtained under identical conditions within one day.

CONCLUSION

An equation for the complex amplitude of surface waves on an inhomogeneous flow is obtained that includes a nonlinear and full linear dispersion for gravity-capillary waves. Based on it we investigated modulation instability in a wide range of angles and frequencies for gravity-capillary waves in approximations of linear and nonlinear dispersion. It is shown that the use of full linear dispersion results in limiting of the instability spectrum both in frequency and angular ranges. Nonlinear dispersion due to the current induced by a finite-length packet of gravity-capillary waves results in decrease of increments and narrowing of the instability regions. This effect is especially strong for perturbations with large detunings of frequencies and angles.

A method of numerical solution of the equations describing propagation of gravity-capillary waves in the presence of an inhomogeneous flow is developed. Based on this method, a program packet has been designed for the corresponding problems.

The parameters of space-time variability of surface waves of different frequencies and amplitudes are measured in a large tank. It is shown that there is a transverse field inhomogeneity, which grows with the increase of the surface wave amplitude. This will make the definition of the characteristics of the surface wave transformation in the current around the sphere more complicated. However, the application of the data processing procedure used before will enable one to ascertain the main regularities of the investigated process. Also, the surface wave damping is estimated. It is shown to be caused by the presence of an elastic film on the surface. The intervals of surface wave amplitudes, in which the ultrasonic sensor data of the water surface elevation and video complex data of the surface slope agree with each other are defined.

REFERENCES

1. Bakhanov, V. V., V. I. Kazakov, O. N. Kemarskaya, I. A. Shereshevskii, and A. Ya. Basovich, 1995. Effect of two-dimensional inhomogeneous flow on surface waves. International Geoscience and Remote Sensing Symposium Proceedings. v.1, 340-342.

2. Bakhanov, V. V., O. N. Kemarskaya, V. I. Pozdnyakova, I. A. Okomel'kova, and I. A. Shereshevskii, 1996. Evolution of surface waves of finite amplitude in field of inhomogeneous current. 1996 International Geoscience and Remote Sensing Symposium Proceedings, v. 1, 609-611.

3. Basovich, A.Ya, V. V. Bakhanov, S. D. Bogatyrev, V. I. Kazakov, O. N. Kemarskaya, V. I. Pozdnjakova, V. I. Talanov, and I. A. Shereshevskii, 1997. Influence of two-dimensional nonuniform currents on surface waves. Izv. Akad. Nauk SSSR. Fiz. Atmos. i Okeana, , v. 33, N3, 371-376.

4. Bakhanov, V. V., K. A. Gorshkov, E. M. Gromov, O. N. Kemarskaya, L. A. Ostrovsky, V. V. Papko, V. I. Talanov, Yu. I. Troitskaya, S. N. Reznik, and I. A. Soustova, 1997. Laboratory Modeling and Theoretical Studies of Wave Processes in the Ocean. Part 2: First Stage Results. Ed., L. A. Ostrovsky. Environmental Technology Laboratory, Boulder, CO, ERL, NOAA, 65 pp.

5. Bakhanov, V. V., I. S. Dolina, S. A. Ermakov, E. M. Gromov, V. V. Papko, V. I. Talanov, and Yu. I. Troitskaya, 1997. Laboratory Modeling and Theoretical Studies of Wave Processes in the Ocean. Part 3: Second Stage Results. Ed. L. A. Ostrovsky. Environmental Technology Laboratory, Boulder, CO, ERL, NOAA, 88 pp.

6. Bakhanov, V. V., V. I. Kazakov, and O. N .Kemarskaya, 1998. Action of inhomogeneous currents on fields of elevations and slopes of water surface nonlinear waves. 1998 International Geoscience and Remote Sensing Symposium Proceeding, v. 5, 2568-2570.

7. Bakhanov, V. V. and V. I. Talanov, 1999. Transformation of nonlinear surface waves in the field of inhomogeneous flows. In Pripoverhnostnyi Sloi Okeana. Fizicheskie Processu i Distantsionnoe Zondirovanie (The Upper Layer of the Ocean. Physical Processes and Remote Sensing). Ed. V. V. Talanov and E. N. Pelinovsky. Nizhny Novgorod, v. 1, 81-106.

8. Dysthe, K.B., 1979. Note on a modification to the nonlinear Schrödinger equation for application to deep water waves. Proc. R. Soc. Lond., v. A369, 105-114.

9. Hogan, S.J., 1985. The fourth-order evolution equation for deep-water gravity-capillary waves. Proc. R. Soc. Lond., v. A402, 359-372.

10. Bespalov, V. I. and V. I. Talanov, 1966. On thread-like structure of light beams in a nonlinear liquid. Pisma v ZHETF, v. 3, N12, 471-476.

11. Benjamin, T. B. and J. E. Feir, 1967. The disintegration of wave trains on deep water. Part 1. Theory. J. Fluid Mech., v. 27, N3, 417-430.

12. Lighthill, M. J., 1965. Contributions to the theory of waves in non-linear dispersive systems. J. Inst. Math. Applics., v. 1, p.269-306.
13. Bespalov, V. I., A. G. Litvak, and V. I. Talanov, 1968. Self-action of electromagnetic waves in cubic isotropic media. In: Nonlinear optics, Novosibirsk, Nauka, 428-463.
14. Vlasov, S. N. and V. I. Talanov, 1997. Self-focusing of waves. N. Novgorod, IAP RAS, 220 pp.
15. Ostrovsky, L. A., 1966. Propagation of wave trains and spatial - temporary self-focusing in nonlinear media. J. Exp. and Theor. Ph., v. 51, N4(10), 1189-1194.
16. Zakharov, V. E., 1966. On wave stability in nonlinear media with dispersion. ZhETF, v. 51, N4, 1107-1114.
17. Zakharov, V. E., 1968. Stability of periodic waves of finite amplitude on surface of a deep fluid. J. Appl. Mech. Tech. Phys., v. 2, 190-194.
18. Zakharov, V. E., 1974. Hamiltonian formalism for waves in nonlinear media with dispersion. Izv.VUZ. Radiofizika, v. 17, N4, 431-453.
19. Yuen, H. C. and B. M. Lake, 1982. Nonlinear dynamics of deep-water gravity waves. Adv. in Appl. Mech., v. 22, p.67-229.
20. Trulsen, K., C. T. Stansberg, and M. G. Velarde, 1999. Laboratory evidence of three-dimensional frequency downshift of waves in a long tank. Physics Fluids, v. 11, N1, p.235-237.
21. Landau, L. D. and E. M. Lifshits, 1988. Theoretical Physics. v. 6, Hydrodynamics. M.: Nauka, 736 pp.
22. Phillips, O.M., 1977. Dynamics of the Upper Ocean. Cambridge Univ. Press, 336 pp., 2nd ed.
23. Monin, A. S. and V. P. Krasitskii, 1985. Phenomena on the Ocean Surface. Leningrad: Gidrometeoizdat, 375 pp.

Figures to Chapter 1

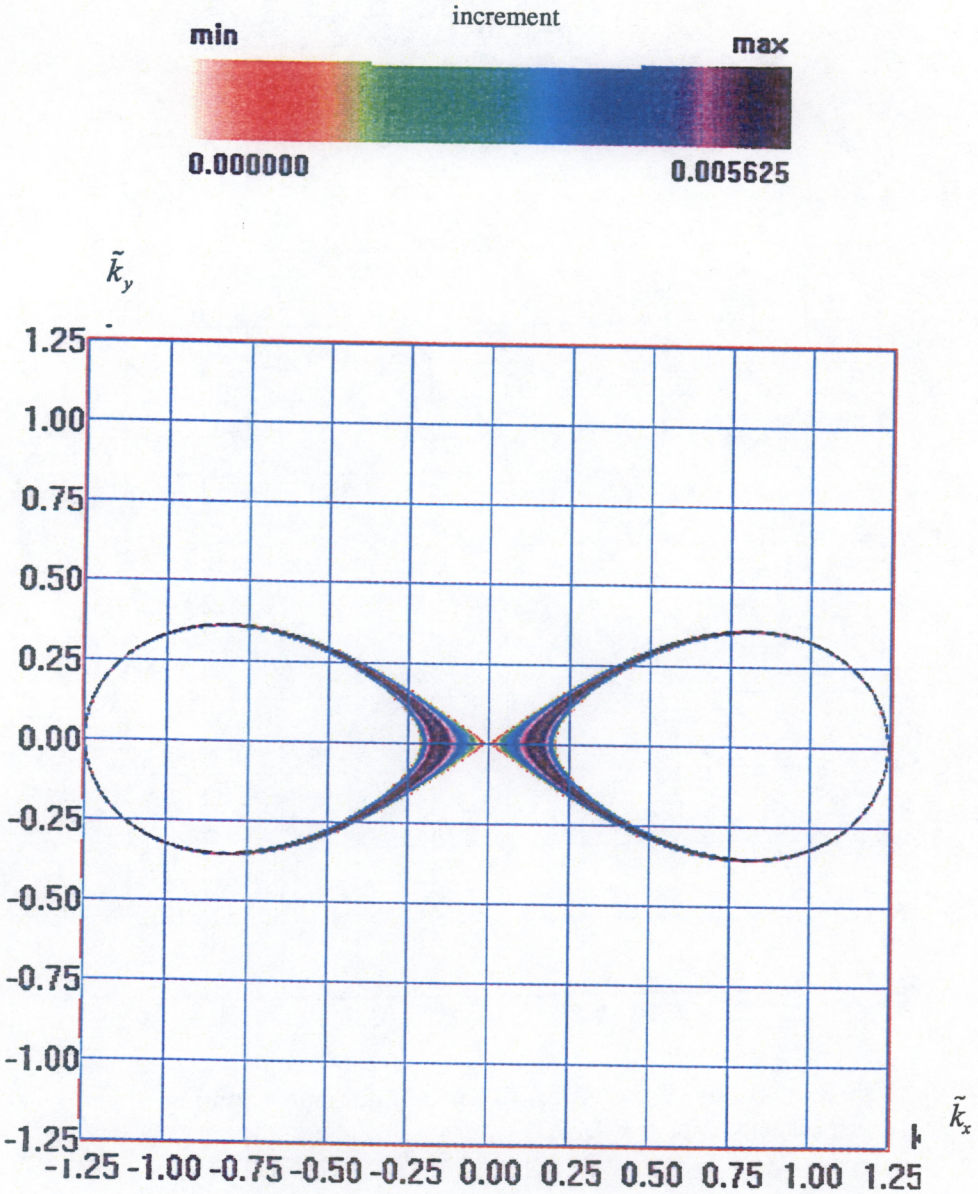

Fig. 2.1. Instability region with an account of full linear dispersion, without nonlinear dispersion, at $A = 0.15$.

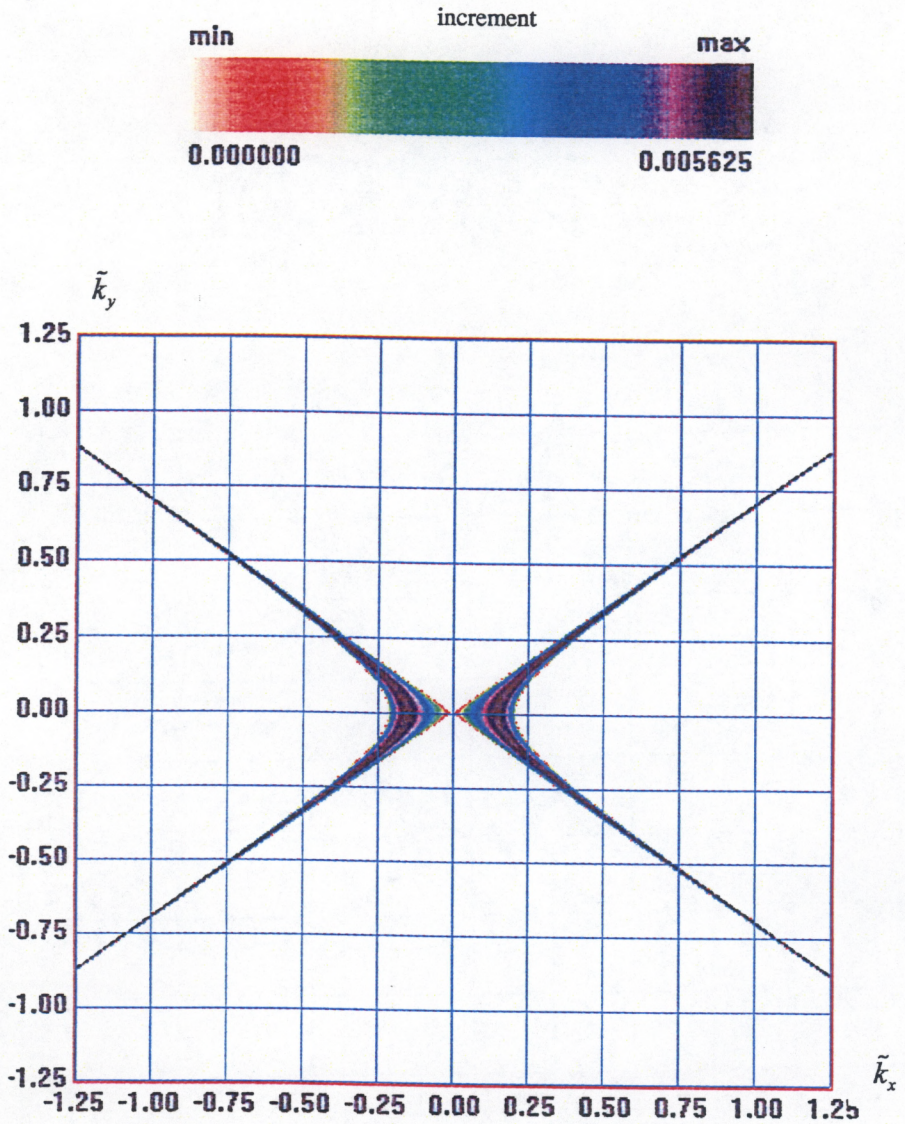

Fig. 2.2. Instability region for full parabolic approximation of linear dispersion at $A = 0.15$.

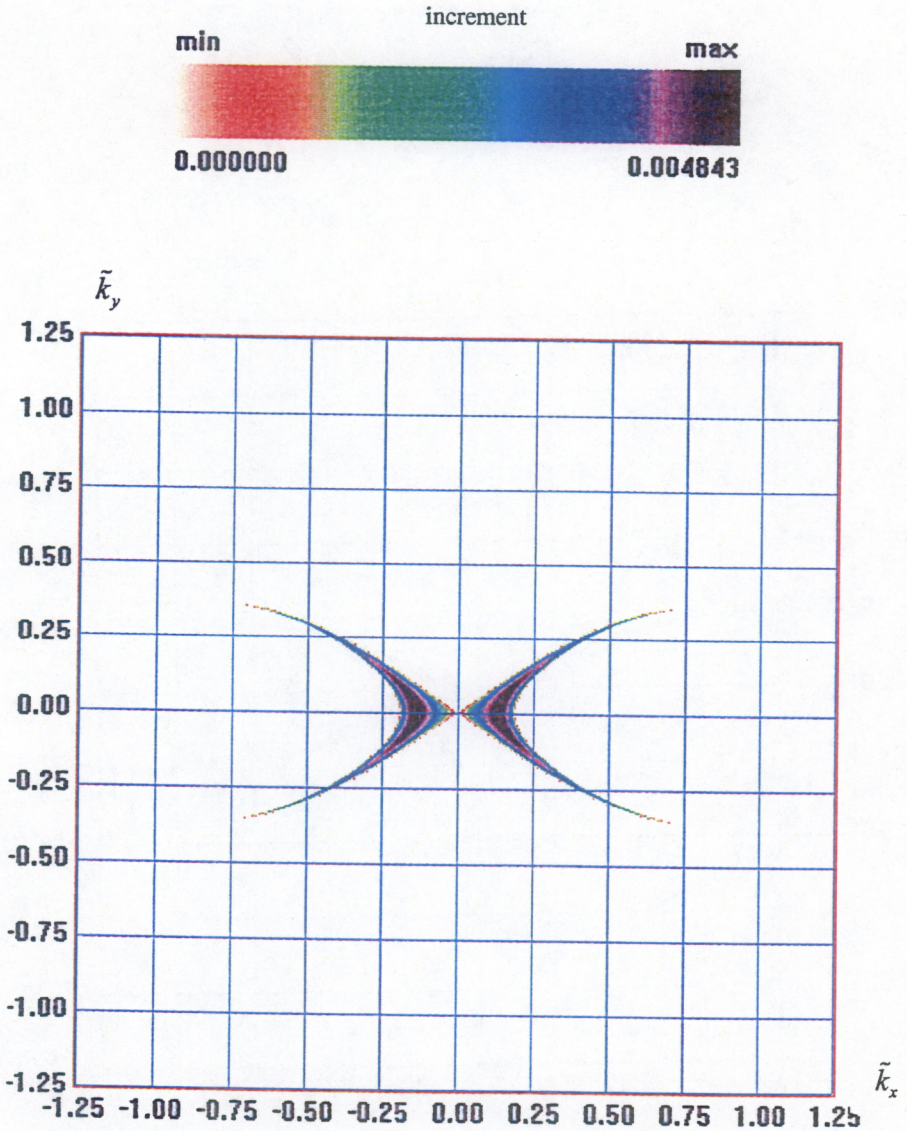

Fig. 2.3. Instability region with an account of full linear and nonlinear dispersion at $A = 0.15$.

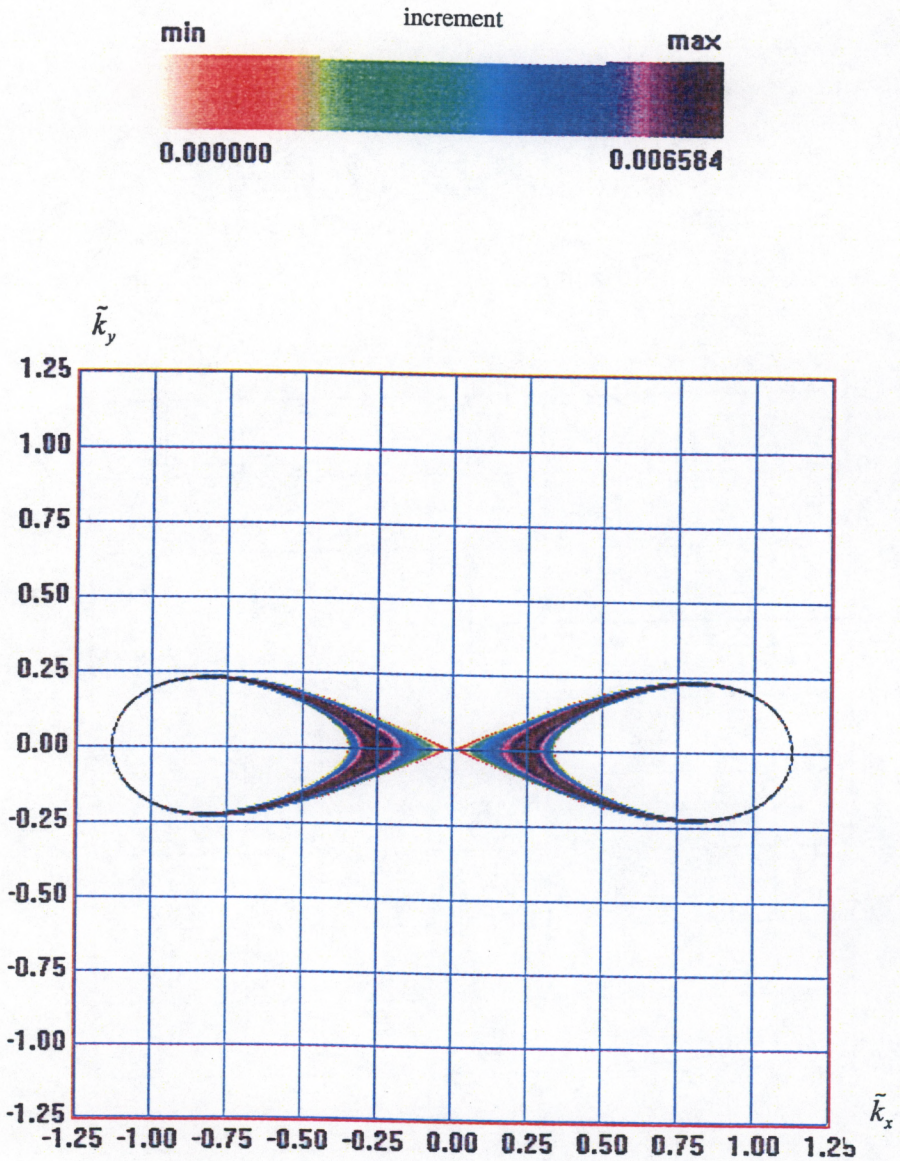

Fig. 2.4. Instability region for gravity-capillary waves with an account of full linear dispersion without nonlinear dispersion at at $A = 0.15$, $V_0 = 0.15$ m/s.

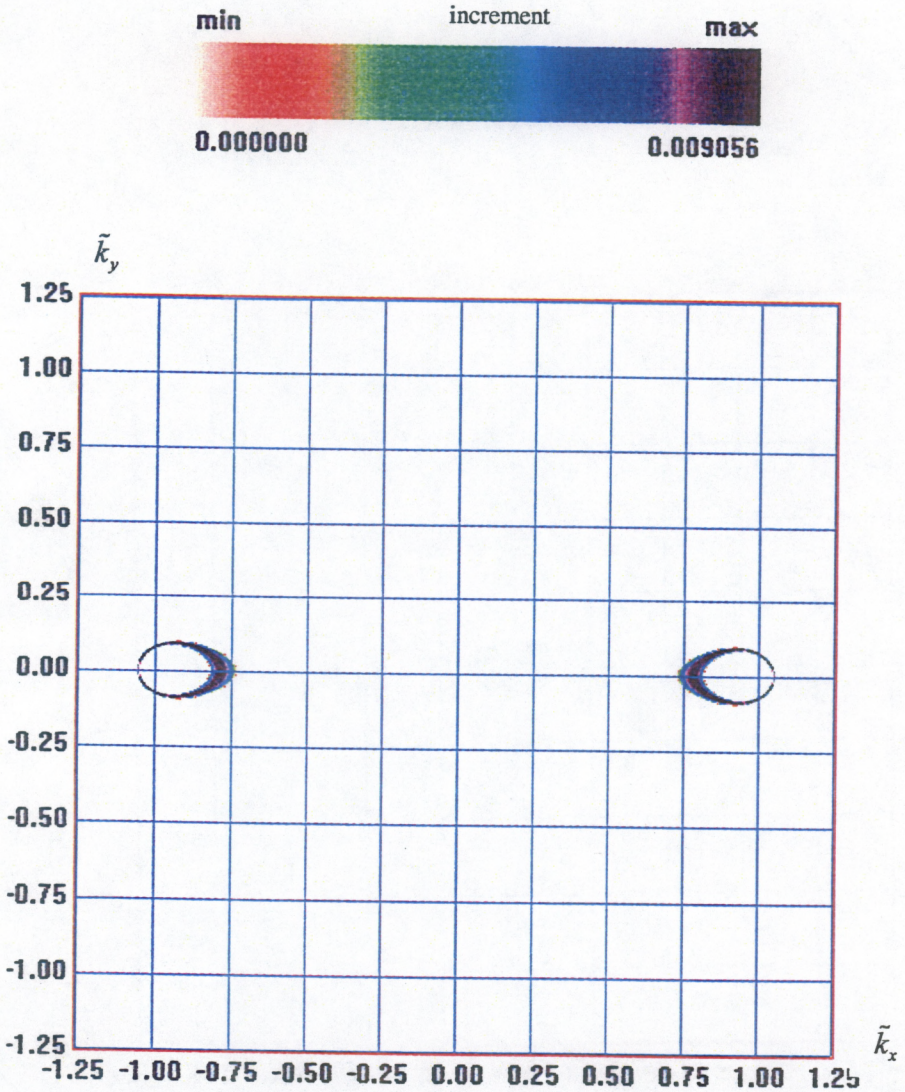

Fig. 2.5. Instability regions for gravity-capillary waves with an account of full linear dispersion, without nonlinear dispersion at $A = 0.15$, $V_0 = 0.12$ m/s.

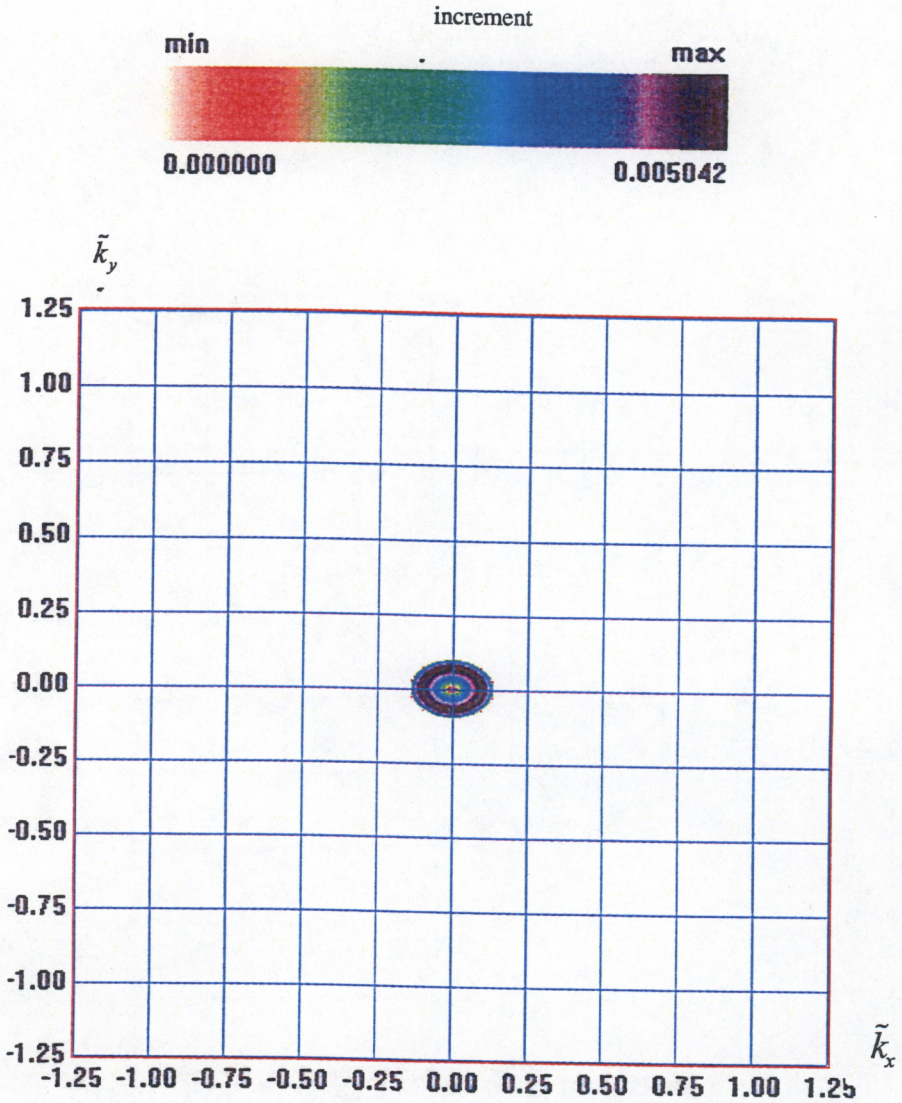

Fig. 2.6. Instability region for gravity-capillary waves with an account of full linear and nonlinear dispersion at A = 0.15, V_0 = 0.08 m/s.

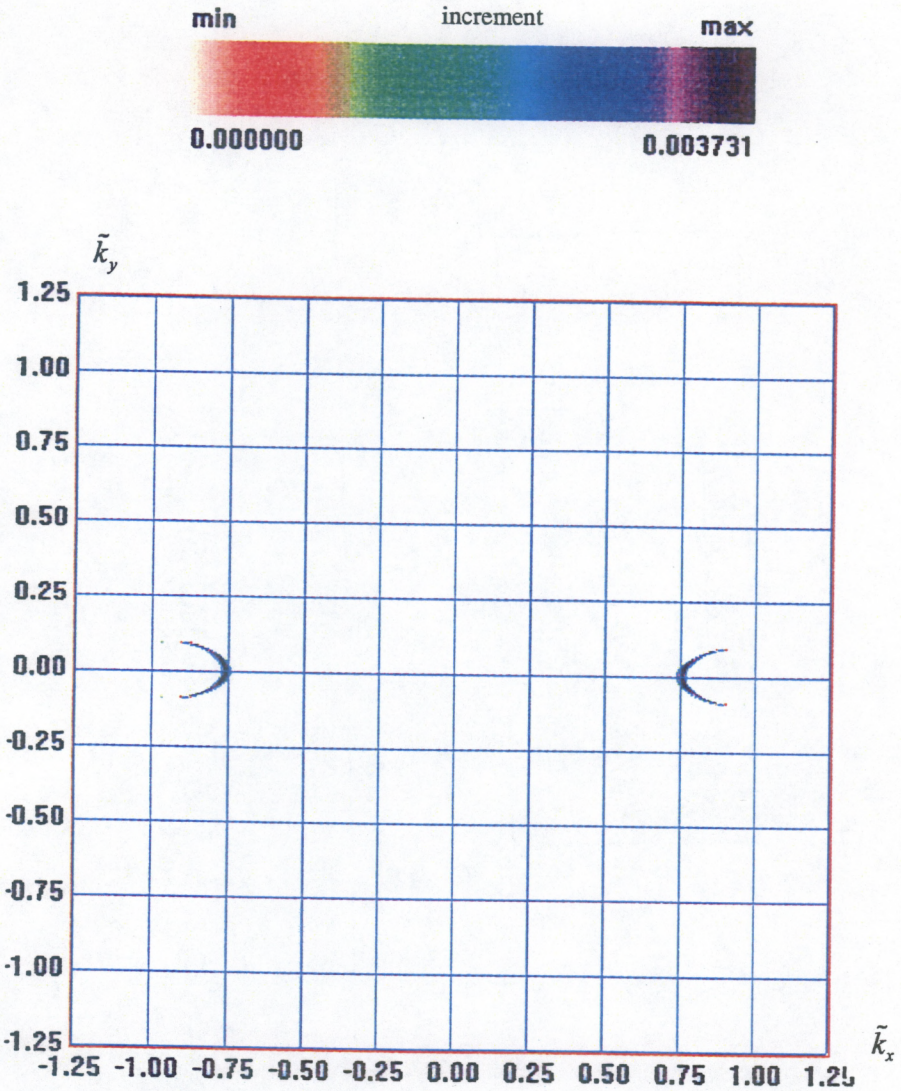

Fig. 2.7. Instability regions for gravity-capillary waves with an account of full linear and nonlinear dispersion at $A = 0.15$, $V_0 = 0.12$ m/s.

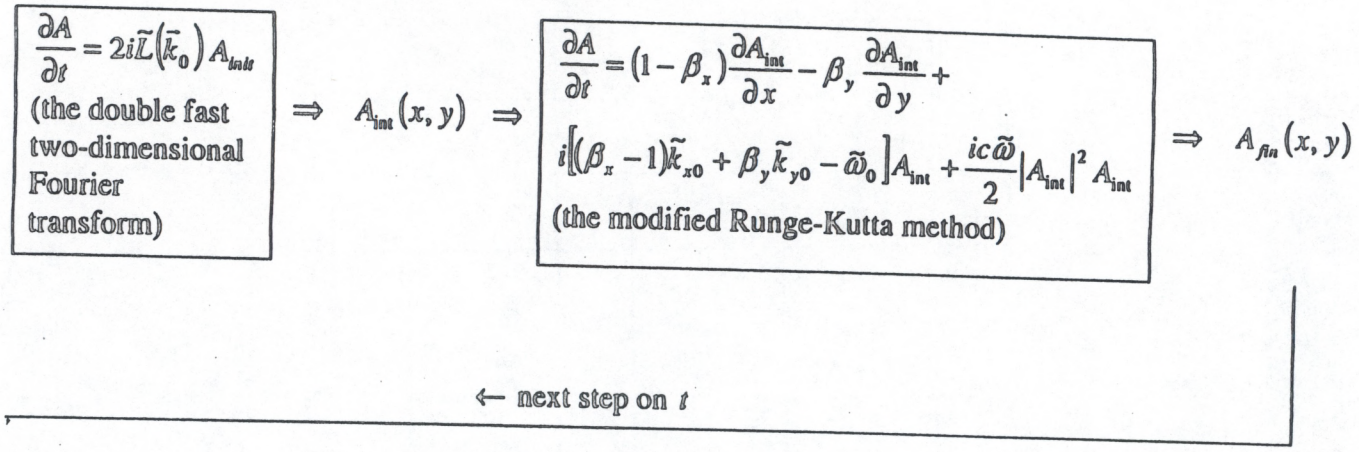

Fig. 3.1. A scheme of numerical calculation.

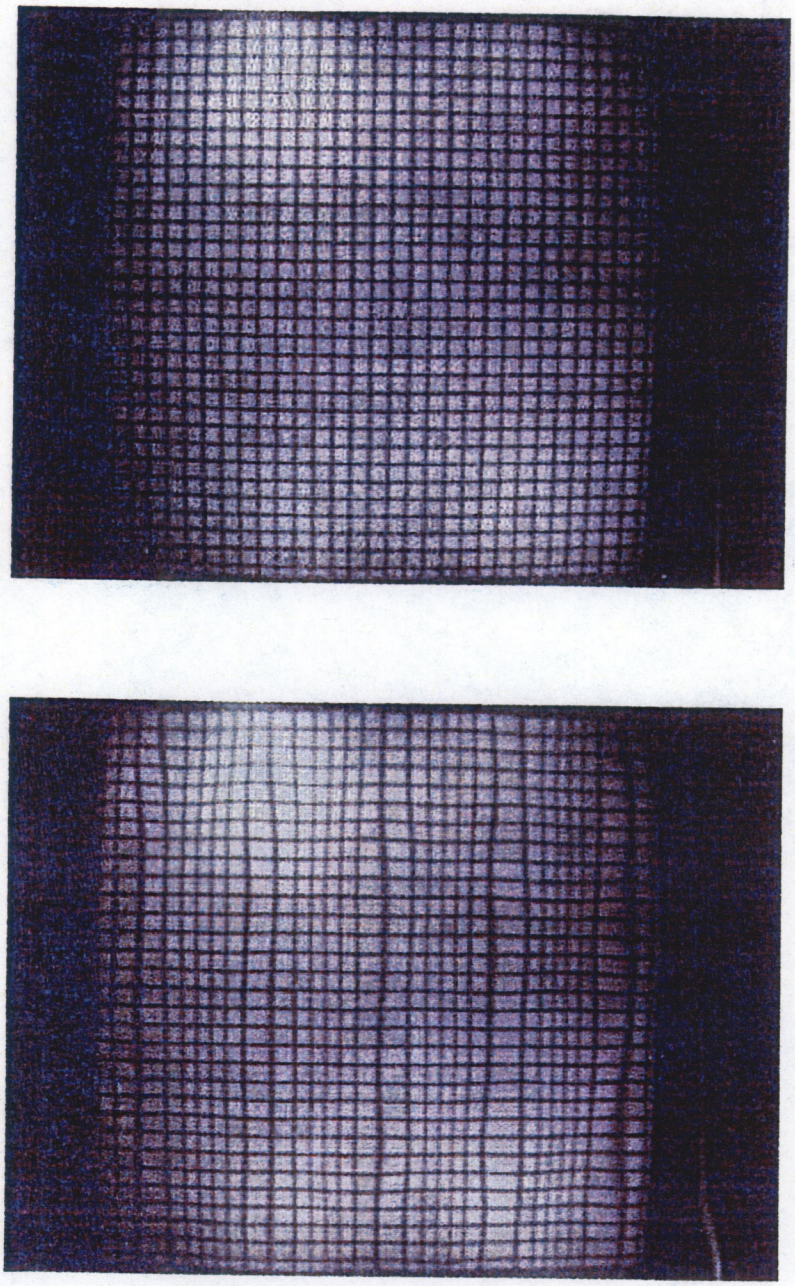

Fig. 4.1. The image of the grate placed on the tank bottom, without surface waves (upper figure) and with a surface wave of frequency 3 Hz (lower figure).

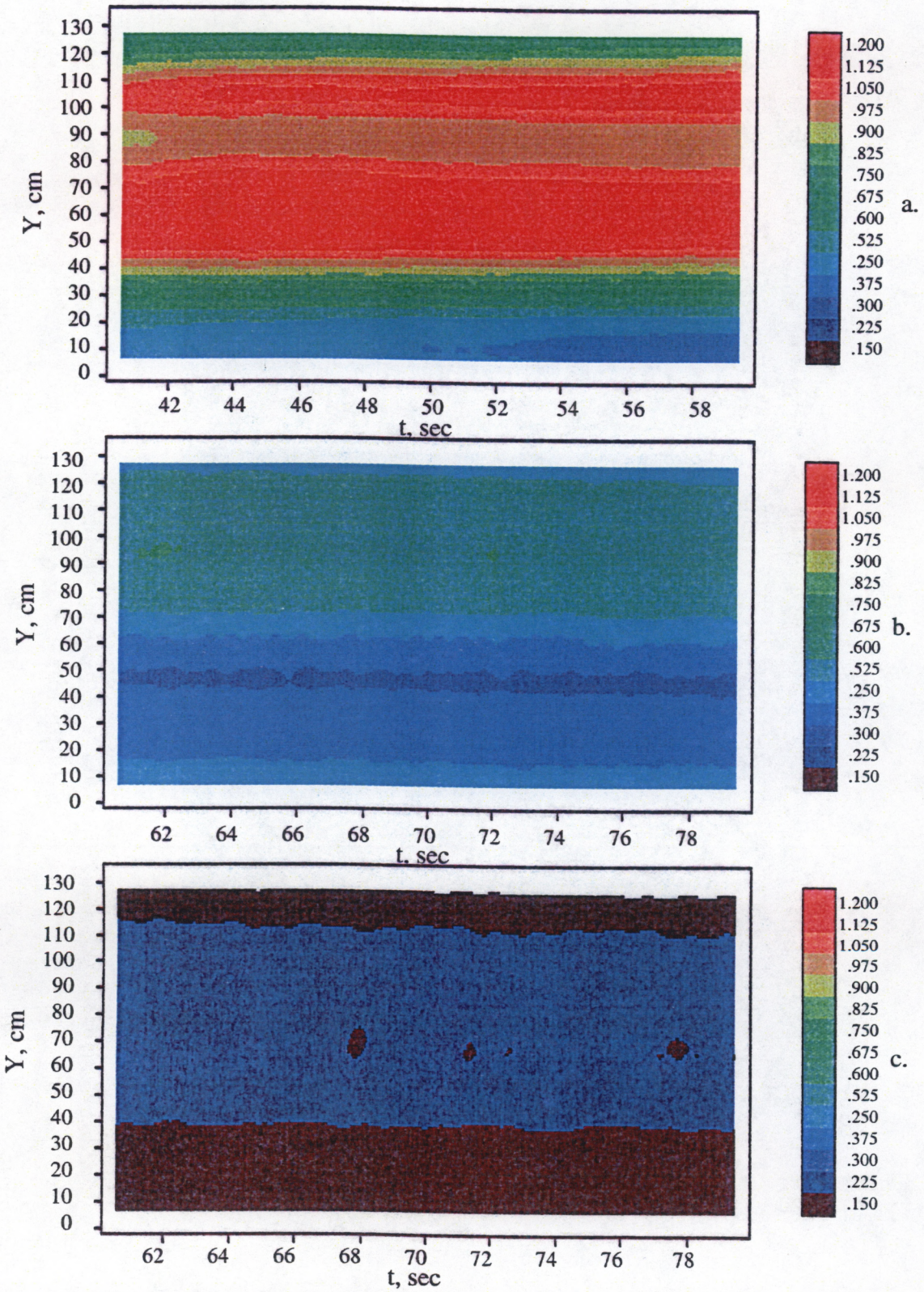

Fig. 4.2. Distribution of the surface wave amplitude A along the axis Y perpendicular to propagation direction (data from ultrasonic sensors). t is the time of the wave maker operation; the values of A are displayed according to the scale on the right of each figure; distance from the wave maker to the sensors line is X = 6 m; oscillation amplitude of the wave maker in all figures is 4 mm. a - f = 2.5 Hz, b - f = 3.0 Hz, c - f = 3.4 Hz.

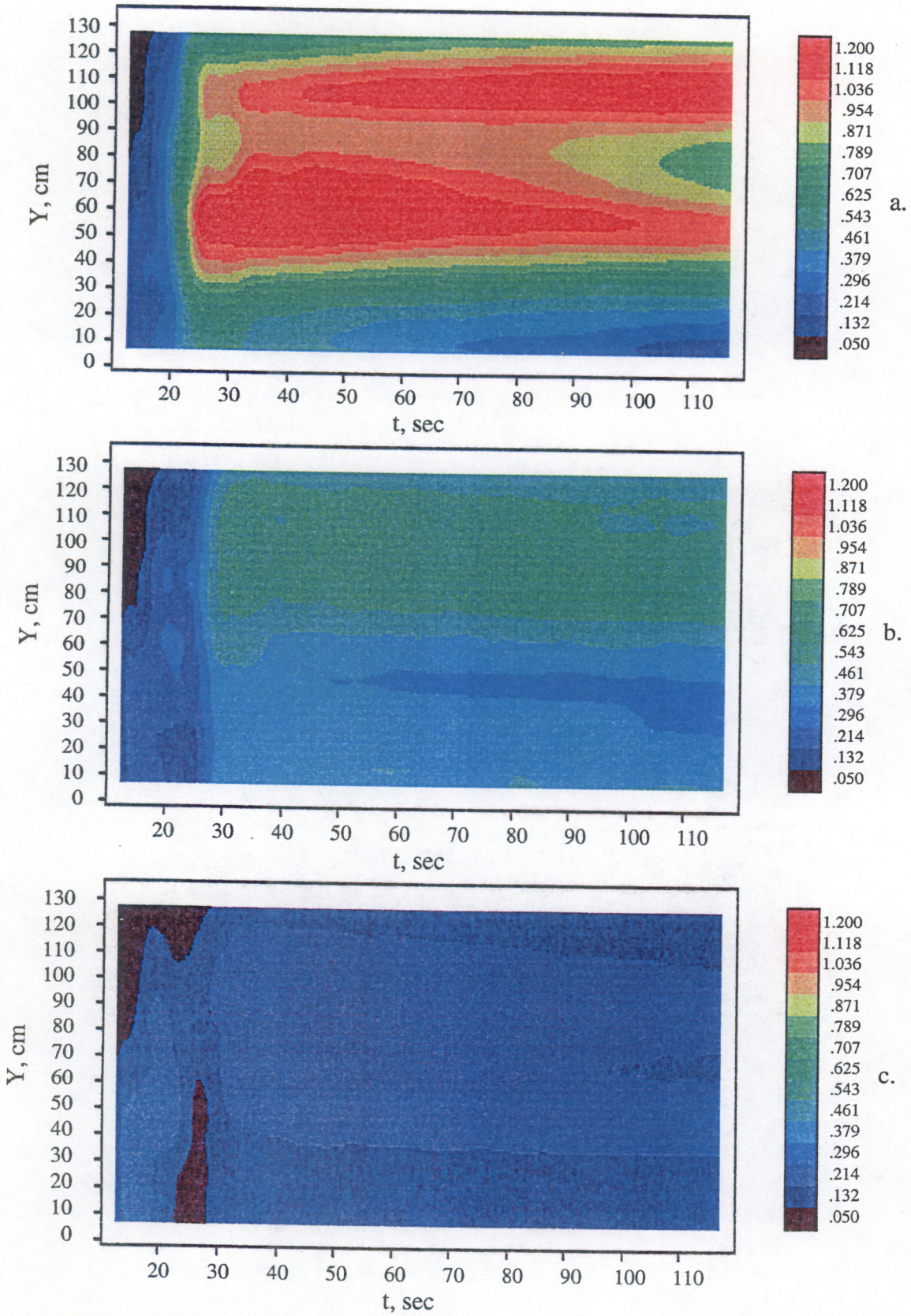

Fig. 4.3. Same as in Fig. 4.2 but the data during the entire time of the experiment are given.

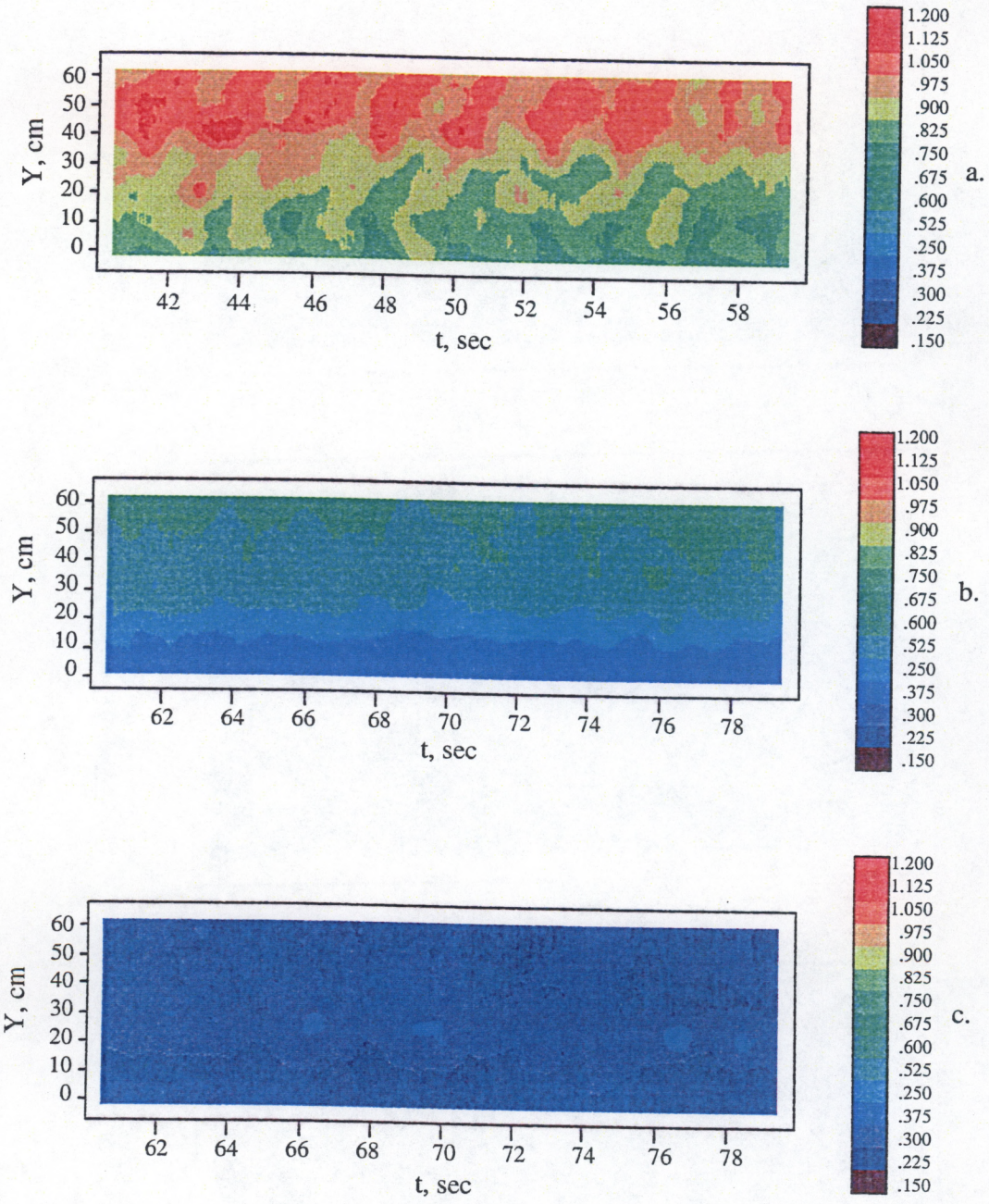

Fig. 4.4. Same as in Fig. 4.2, but the experimental data are obtained with the use of the video complex.

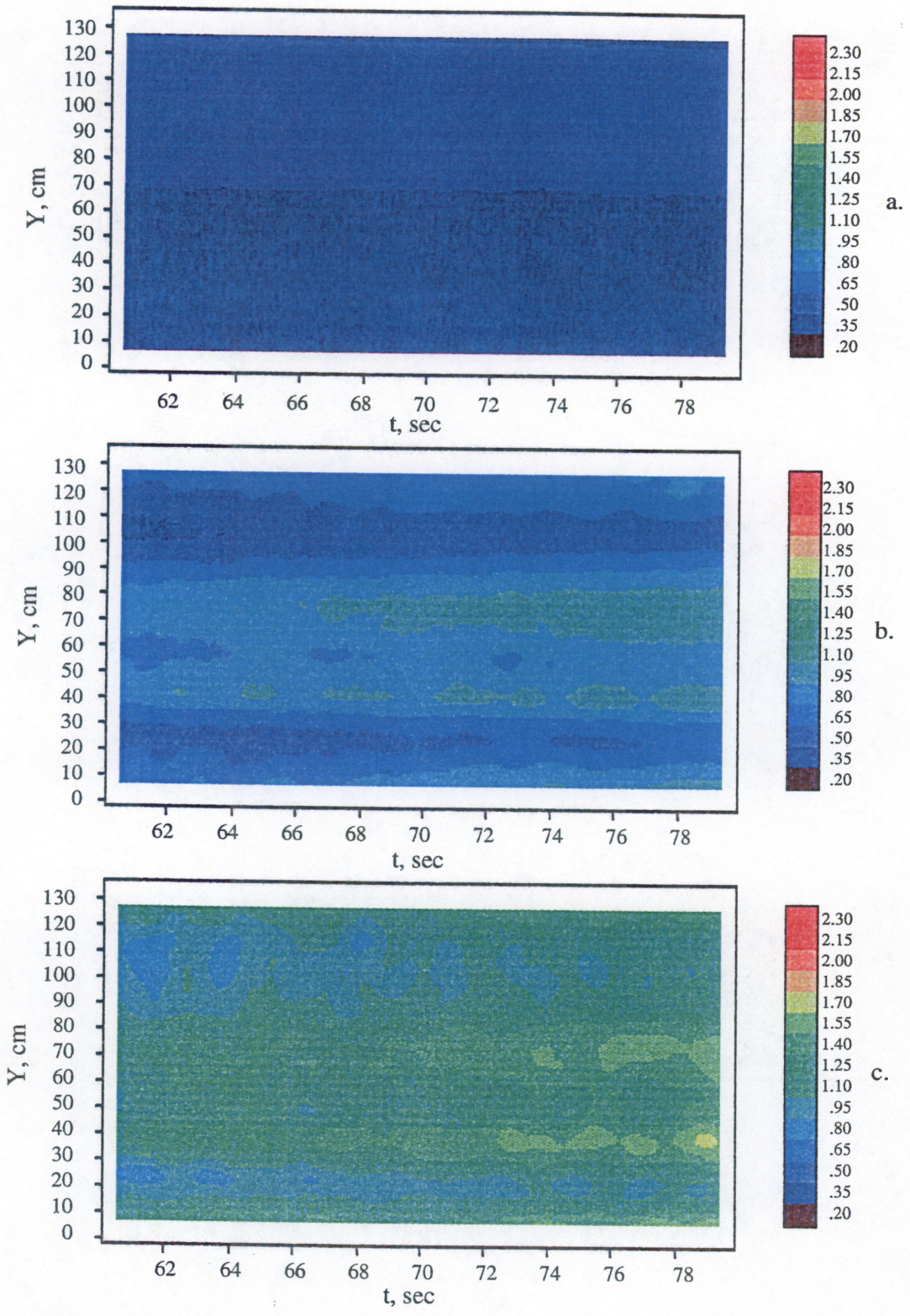

Fig. 4.5. Analogous to Fig. 4.2, but in all figures the frequency f =3.0 Hz, the oscillation amplitude of the wavemaker is 4 mm (a), 5mm (b) and 6 mm (c).

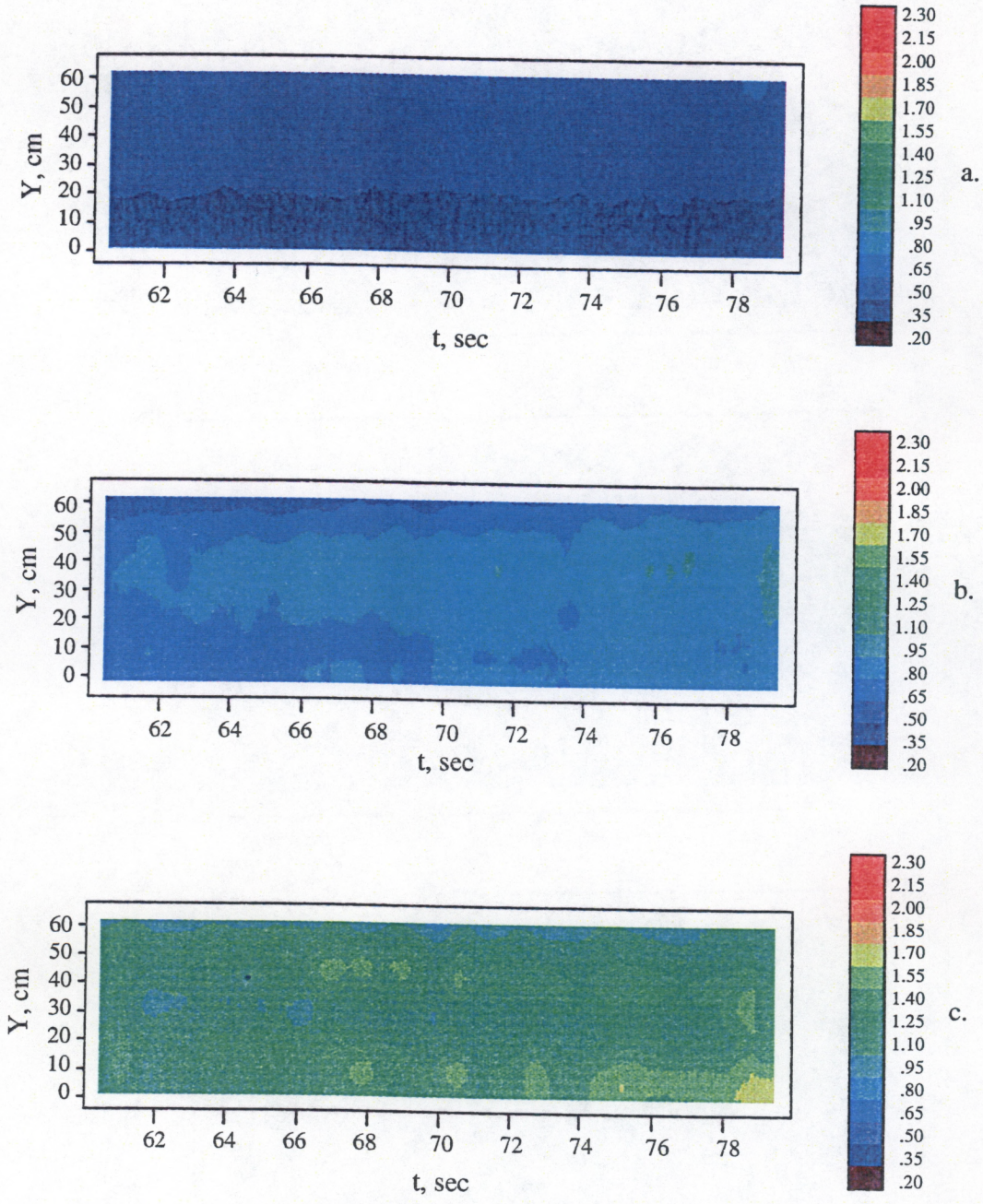

Fig. 4.6. The same as in Fig. 4.5, but the experimental data are obtained with the use of the video complex.

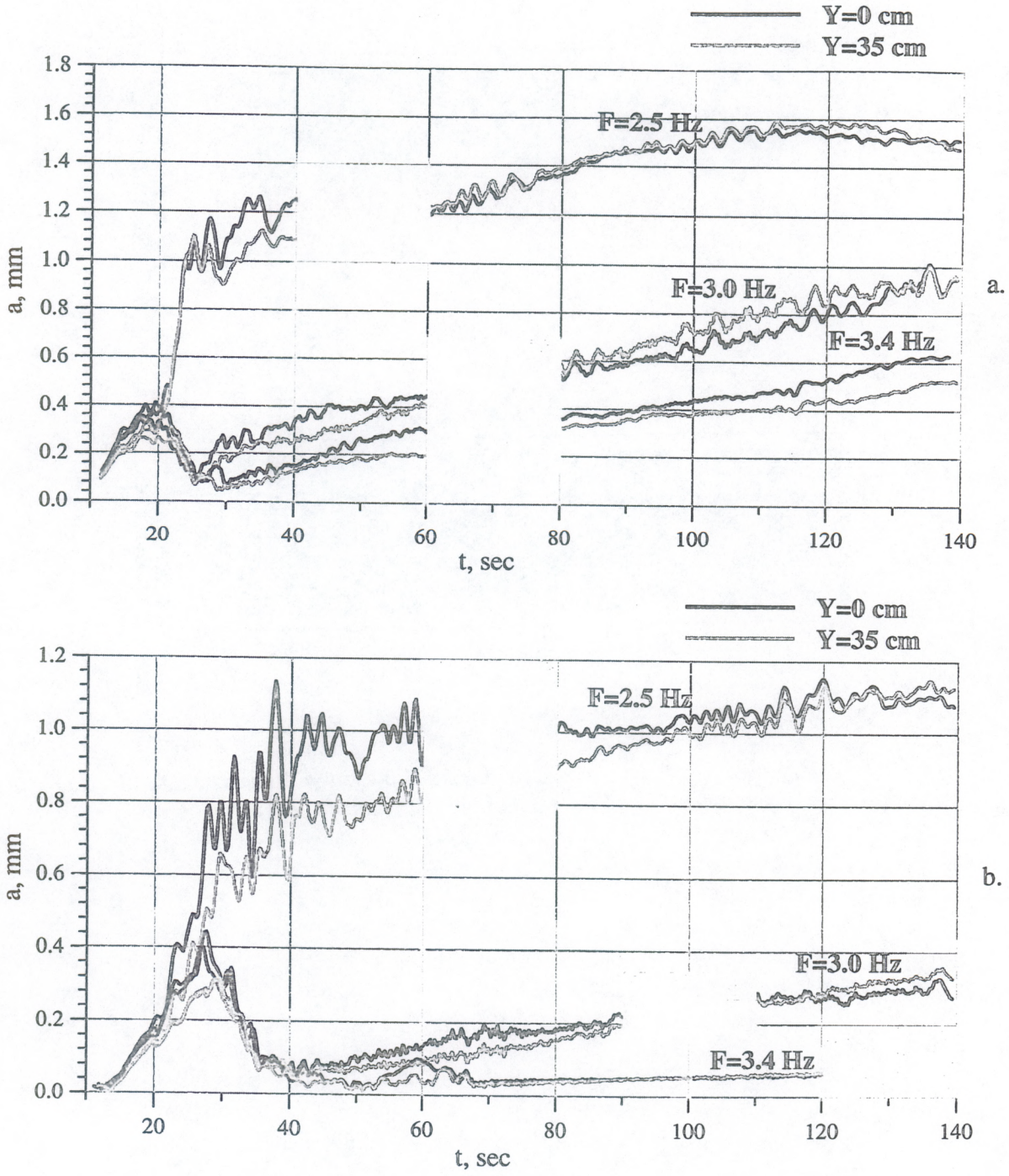

Fig. 4.7. Time dependence of the surface wave amplitude for two values of Y : 0 and 35 cm, obtained with the use of ultrasonic sensors. Oscillation amplitude of the wave maker is 4 mm. a - X = 6 m, b - X = 9 m.

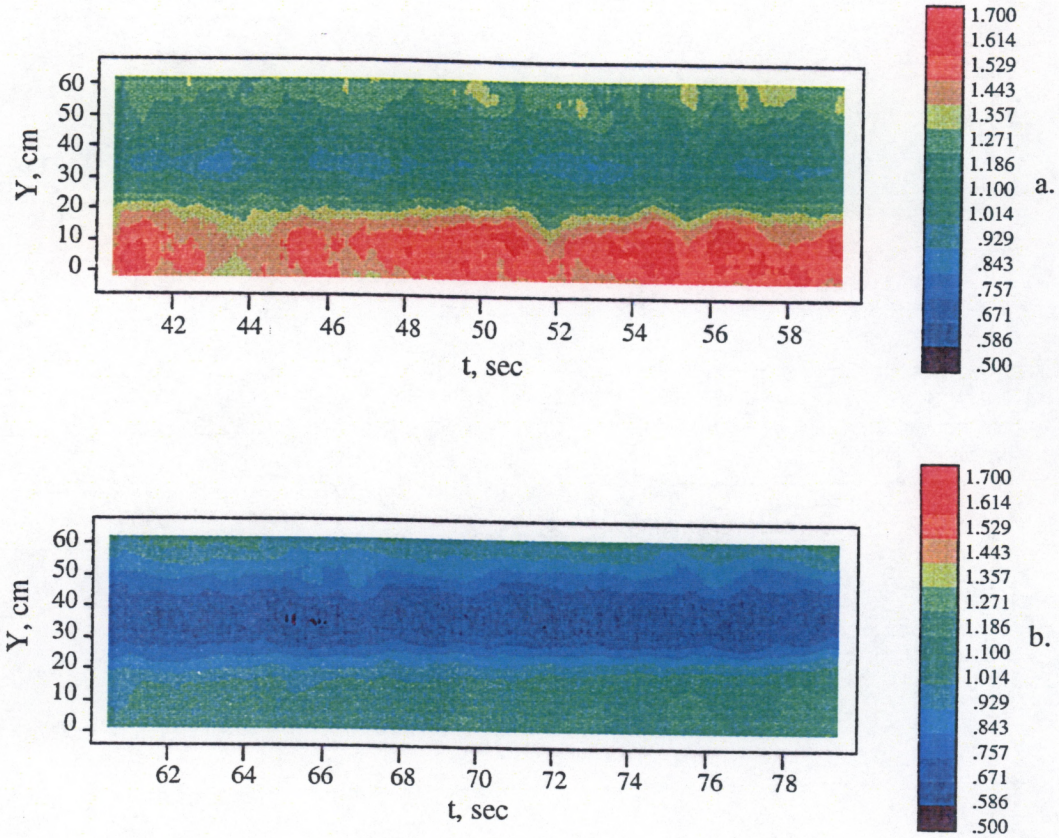

Fig. 4.8. The change of the surface wave amplitude distribution with the increase of the distance from the wave maker. Oscillation amplitude of the wave maker is 4 mm, f = 2.5 Hz. a - X = 6 m, b - X = 9 m. The data are obtained with the use of the video complex.

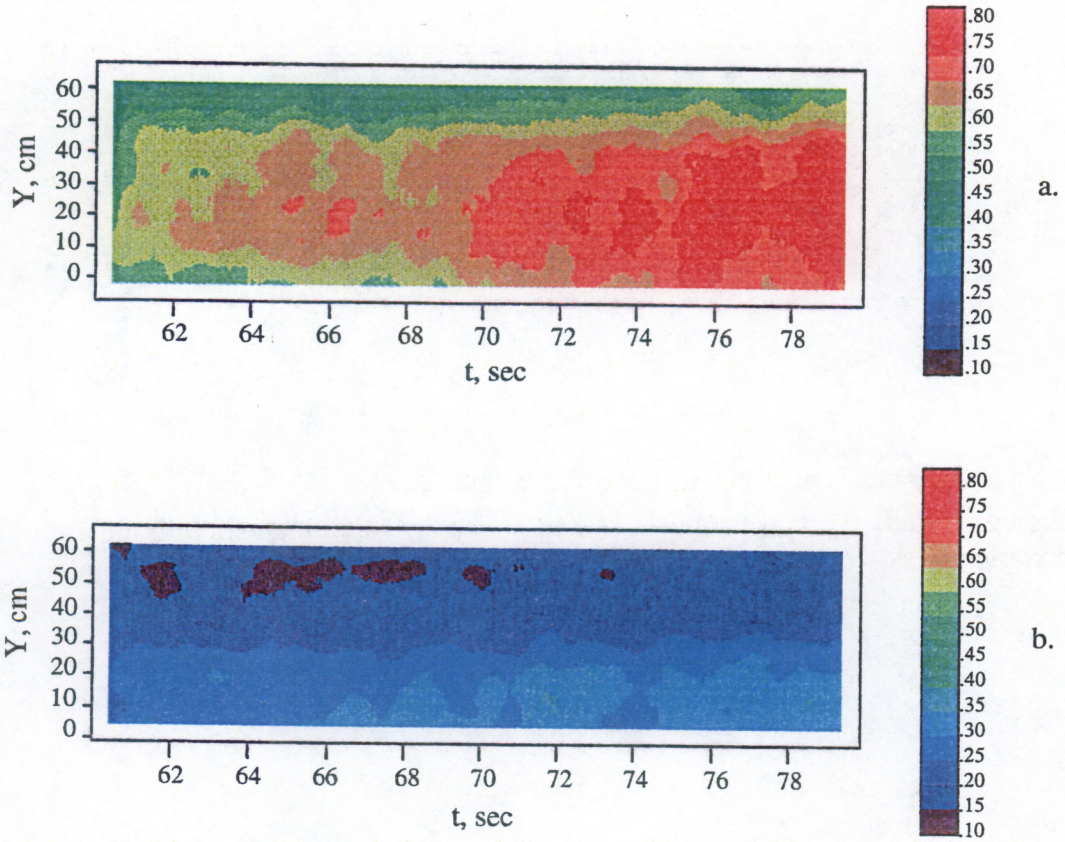

Fig. 4.9. The same as in Fig. 4.8, but f = 3.0 Hz.

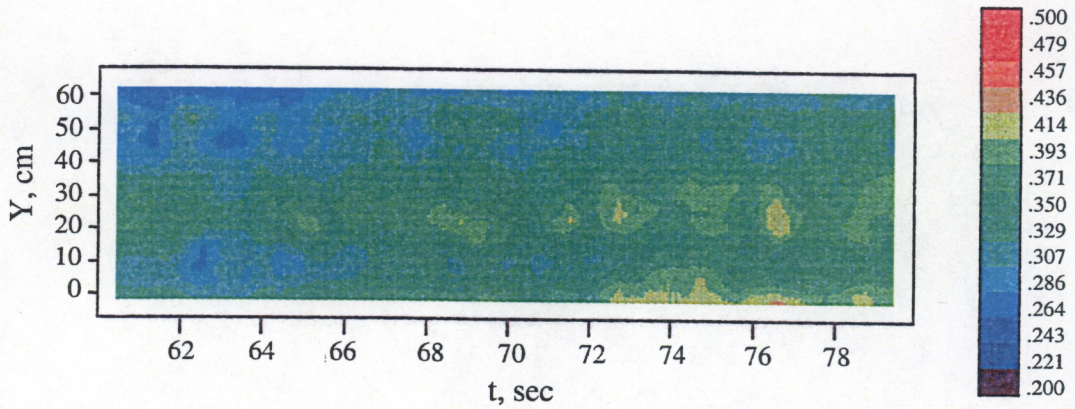

Fig. 4.10. Distribution of the surface wave amplitude for X = 6 m, f = 3.4 Hz. Oscillation amplitude of the wavemaker is 4 mm. The data are obtained with the use of the video complex.

Chapter 2. SURFACE WAVE MODULATION BY FLOW AROUND A MOVING SPHERE

Abstract

This chapter reflects the second stage of the IAP work in 2000 in what regards experimental studies and numerical calculations of wave transformation by a current created by a moving sphere. The characteristic surface wavelength can be comparable with both the characteristic spatial scale of the flow and the depth of body motion. It is found that, along with group synchronism, surface wave nonlinearity can significantly enhance the variability of surface wave amplitude in a wide frequency range. The proposed theoretical model gives a fairly good description of the basic features of the phenomenon.

Contents of Chapter 2

INTRODUCTION

Theoretical and experimental research into surface wave transformation in the field of a flow around a moving sphere has been carried out at IAP RAS since 1996 [1-5]. Theoretical aspects of this problem were considered in [1,2,5], and [3,4] were devoted to experimentation

The transformation of linear surface waves was considered in [1], and the influence of surface wave nonlinearity on the process of their modulation was analyzed in [5]. It was shown in [5] that three principal stages of surface wave transformation by an inhomogeneous flow can be distinguished:

At the initial stage, the condition of group synchronism between the surface wave group velocity and the velocity of the body motion is of primary importance; surface waves demonstrate a "linear" character of transformation.

At the next, stage, the gained modulation of surface wave amplitude may serve as a "seed" for the known Benjamin–Feir instability, and as a result, the nonlinearity of surface waves leads to a sharp increase in their amplitude variability. In contrast to the classical Benjamin–Feir instability, this process is radically affected by the presence of the inhomogeneous flow around the sphere.

At the final stage, the small-scale wave amplitude variations due to instability in the used equation appear in theoretical calculations. As a result, the applicability of the method used in [5] is violated.

The time of the transition from one stage of the evolution of surface wave anomalies to another is determined, primarily, by the amplitude of surface waves and the intensity of the inhomogeneous flow. As the wave amplitude increases, the transition from one stage to another becomes faster.

At the first stage of this project, an equation was obtained that takes into account the frequency dispersion of wave nonlinearity. Analysis of the stability diagram for this equation shows that the aforementioned small-scale instability of the surface wave envelope decreases substantially. Therefore, this equation allows for investigation of surface wave variability at larger time intervals. Theoretical calculations at the present stage of the research were carried out on the basis of this equation.

Results of laboratory measurements of spatial distribution of the surface wave amplitude in the presence of a moving sphere obtained by means of contact sensors were presented in [3] for several frequencies of surface waves. The first results of measurements with the aid of a remote optical system were given in [4].

Here, we report on measurements of the transformation of surface wave characteristics using the measuring systems described in the previous report. These are acoustic sensors of water surface displacement at definite points and an optical video system for recording water surface slopes in a particular region of space. Unlike our previous works, measurements were taken for shorter surface waves and for lower velocities of the sphere motion. This enabled us to investigate surface wave transformation at its later stages in a tank of the same length.

1. EXPERIMENTAL INVESTIGATION OF SURFACE WAVE TRANSFORMATION BY INHOMOGENEOUS FLOW AROUND A MOVING SPHERE IN A LARGE THERMOSTRATIFIED TANK OF IAP RAS

1.1 Experimental design

We reiterate that the large thermostratified tank of IAP RAS is 20 m long, 4 m wide and 2 m deep [6,7]. The scheme of the experiment was the following (Fig. 1.1):

• Two spheres of radius $r = 4.25$ cm and $r = 9.5$ cm were towed alternately along a stretched string at a depth h equal to two diameters of each sphere (h is the distance from the unperturbed water surface to the center of the sphere). The velocity of the sphere, U_0, was 0.26 m/s in both cases. Due to the known similarity relations, the flow around each of the spheres must produce inhomogeneous flows on water surface with the same maximal velocity but with different spatial scales. Thus, we can investigate how the ratio of the spatial scale of the flow to the length of the surface waves excited by a wave maker affects the transformation of these waves. Earlier experiments [5] showed that an increase in h naturally decreases the variability of the surface wave amplitude, but the location of the regions of increasing and decreasing amplitude and their size remain unchanged.

• A wave maker placed at the end of the tank where the sphere started its motion generated surface waves with frequency f varying from 3.5 Hz to 2 Hz (the group velocity of surface waves with frequency of 3 Hz was close to the velocity of sphere motion). The generated waves were absorbed by a wave damper at the opposite end of the tank, thus providing a regime of traveling surface waves. The generation of surface waves was initiated a little earlier than the moment at which the motion of the sphere begins. This time difference was chosen so that surface waves occupy a region several meters long ahead of the sphere.

Parameters of the surface waves were recorded by the ultrasonic sensors and video system mentioned above. They were placed at distances $R = 3.5$ to 8.5 m from the wave maker. The instant t^* when the center of the sphere intersected the sensor plane was recorded by a special contact sensor. We assumed that during the time (~ 5s) when significant anomalies of surface waves caused by the motion of the sphere passed the sensors, the characteristics of the anomalies changed only slightly. The recorded temporal variations of surface wave amplitude were recalculated into the dependence on the coordinate x directed along the axis of the tank.

The resulting spatial distributions of surface wave amplitude depend on four parameters: radius of the sphere, frequency and amplitude of the surface waves, and distance between the wave maker of surface waves and the point of measurement. Therefore, to construct a convincing pattern of the process, many time series have been recorded. Here, we will describe only the most important regularities of the surface wave transformation due to the flow streamlining the sphere.

1.2. Flow around a sphere

We measured all three velocity components of the flow around a moving smaller sphere (4.25 cm in radius) at a small distance from its surface (Fig. 1.2). For theoretical calculations we replace the sphere by a dipole situated at depth h and oriented along the x-axis, and map (reflect) it with respect to the water surface. Then, we obtain well-known expressions for velocity field components:

$$V_x = -\frac{U_0 r^3}{2}\left[\frac{-2x^2 + y^2 + (z-h)^2}{\left[x^2 + y^2 + (z-h)^2\right]^{5/2}} + \frac{-2x^2 + y^2 + (z+h)^2}{\left[x^2 + y^2 + (z+h)^2\right]^{5/2}}\right]$$

$$V_y = -\frac{U_0 r^3}{2}\left[\frac{-3xy}{\left[x^2 + y^2 + (z-h)^2\right]^{5/2}} + \frac{-3xy}{\left[x^2 + y^2 + (z+h)^2\right]^{5/2}}\right] \qquad (1.1)$$

$$V_z = \frac{U_0 r^3}{2}\left[\frac{-3x(z-h)}{\left[x^2+y^2+(z-h)^2\right]^{5/2}} + \frac{-3x(z+h)}{\left[x^2+y^2+(z+h)^2\right]^{5/2}}\right].$$

Results of calculations by Eqs. (1.1) under the same conditions for which the measurements presented in Fig. 1.2 were made, are shown in Fig. 1.3. One can see from the figure that the calculations agree well with the experimental data.

1.3. Two-dimensional amplitude distributions of surface waves of different frequencies

Measurements for the smaller sphere were made at the same distance R from the wave maker for each gauge set: $R = 6$ m for acoustic sensors and $R = 5$ m for a video system. Results of measurements of the spatial distribution of surface wave amplitude with the aid of the ultrasonic sensors are presented in Fig. 1.4 and by the video system in Fig. 1.5. Figures 1.4 (a) and 1.5 (a) correspond to a frequency $f = 2.5$ Hz, (b) to $f = 2.9$ Hz, and (c) to $f = 3.5$ Hz. The center of the sphere is at the point $x = 600$, $y = 0$ in Fig. 1.4 and at the point $x = 500$, $y = 0$ in Fig. 1.5. The surface wave parameters were recorded by acoustic sensors on only one side of the axis of the tank. Figure 1.4 was made symmetric by mapping of the recorded anomalies with respect to the x-axis. We did not do so for the results of measurements by the video system because we have no data on the variability of surface wave amplitude in the region adjoining the axis of the tank. The axes are calibrated in centimeters. The relative variation of surface wave amplitude, δa, is plotted in the figures. In each experimental series, the surface wave amplitude for each value of y was normalized to its average value in the region shown in the figures. The variation of δa is depicted by color in accord with the scale bar shown to the right of each picture.

The spatial distribution of surface wave amplitude contains regions of amplitude decrease and increase. The main region of decreased a is located ahead of the sphere for waves with $f = 2.5$ Hz, over the sphere for waves with $f = 2.9$ Hz, and behind the sphere for $f = 3.5$ Hz. This is due to the fact that the group velocity of surface waves increases with decreasing f, so that for waves with $f = 2.5$ Hz whose group velocity is higher than U_0, the perturbations move forward, while for waves with $f = 3.5$ Hz they primarily propagate backward with respect to the body. It is seen from the figures that variability of the wave amplitude becomes more pronounced with the increase of its frequency. This does not completely agree with the theoretical concepts because the wave group velocity for $f = 2.9$ Hz is close to the velocity of the sphere motion, and the highest values of δa could be expected for this case of group synchronism. A possible explanation is that in our experiment, the waves with $f = 3.5$ Hz dissipate strongly, so that they were initially generated with a very large amplitude to secure a sufficient amplitude level when they reach the region of measurements. (As was shown in the first-stage report, the damping coefficient for these surface waves is several times higher than for the others.) As a result, the wave nonlinearity leads to strong amplitude variations, δa, which can reach rather high values. [5]. Comparison of Figs. 1.4 and 1.5 shows that the structure of surface wave anomalies and the variability of surface wave amplitude are very close. Exceptions are Figs. 1.4 (c) and 1.5 (c), where the structures of surface wave anomalies are similar but the values of δa are larger in Fig. 1.4 (c). This can be due to different distances from the wave maker to the region of the measurements in these figures: 6 m in Fig. 1.4 and 5 m in Fig. 1.5; this difference is important for nonlinear waves when the variability of wave amplitude develops very fast.

For the larger sphere, 9.5 cm in radius, measurements by acoustic sensors were taken at three distances from the wavemaker: R = 3.5 m, 6 m, and 8.5 m. Measurements with the video system were made at R = 5 m, the same as the smaller sphere. Results of the measurements of the spatial distribution of surface wave amplitude by ultrasonic sensors for R = 3.5 m are given in Fig. 1.6. Figure 1.6 (a) corresponds to f = 2.0 Hz, (b) to f = 2.5 Hz, (c) to f =2.9 Hz, and (d) to f =3.3 Hz. The center of the sphere is at a point x = 350, y = 0. Similarly to Figs. 1.4 and 1.5, regions of the most significant variability of surface wave amplitude are shifted backwards as their frequency is increased. For waves with the frequency f = 2.0 Hz whose group velocity is much higher than U_0, the changes of the amplitude are, as expected, small. The largest values of δa were recorded for the waves with f = 2.9 Hz that are close to the condition of group synchronism. This is in contrast to the previous case, supposedly because the effects of wave nonlinearity at f =3.3 Hz did not have sufficient time to develop at a shorter distance.

Spatial distributions of the wave amplitude at different frequencies are presented in Figs. 1.7 and 1.8 for R = 6 m and R = 5 m (measurements were made, respectively, by acoustic sensors and by the video system). Figure 1.7 (a) corresponds to f = 2.0 Hz, (b) to f = 2.4 Hz, and (c) to f = 2.9 Hz. Figure 1.8 (a) corresponds to f = 2.4 Hz, and (b) to f = 2.9 Hz. We were unable to obtain reliable data for the waves with f = 3.4 Hz in this series: data of measurements by acoustic sensors and the video system differ strongly both in the structure of anomalies and the values of δa. This may occur because variability of such high-frequency, strongly nonlinear surface waves due to flow around a large sphere develops too fast, and for R = 6 m the anomalies enter the stage when not only δa but also their structure change very rapidly. This supposition needs further verification.

For surface waves with f = 2.4 Hz, amplitude variability by a large sphere is greater than that for a small sphere (cf. Figs. 1. 4 (a) and 1. 7(b)). At the same time, they are almost the same for f = 2.9 Hz. The spatial scales of surface wave anomalies are larger in the flow around a larger sphere, which is quite natural. The change of anomalies with the variation of wave frequency depicted in Figs. 1.7 and 1.8 is qualitatively the same as before: the variability of surface wave amplitude is weak at f = 2 Hz, and the anomalies shift backwards with increasing f. The data measured by acoustic sensors and by the video system are close. The effect of group synchronism is not decisive for such R, and the values of δa are close for f = 2.4 Hz and f = 2.9 Hz.

On the whole, the experimental results show that the condition of group synchronism between surface waves and the velocity of sphere motion is most important at the early stages of the evolution of surface anomalies.

1.4. Evolution of surface wave anomalies in time

Development of spatial variability of surface wave amplitude in the course of propagation will be illustrated on two examples: for waves close to the synchronism condition and for longer waves. Spatial distributions of amplitude for waves with f = 2.4 Hz are shown in Fig. 1.9: (a) at R = 3.5 m, (b) R = 6 m, (c) R = 5 m (data from the video system corresponding to Fig. 1.9 (b)), and (d) R = 8.5 m. As the distance increases, surface wave anomalies are expanded, and δa increases in them. The corresponding data for surface waves with f = 2.9 Hz (synchronous case) are given in Fig.1.10. In this case, δa rapidly reaches large values, and then only expansion of the anomalies is observed. Such a character of the evolution of surface wave amplitude variability agrees well with the theoretical results obtained earlier in [5].

1.5. Surface wave variability for different amplitudes

Theoretical estimates show that the variability of surface waves with $f = 2.0$ Hz and 2.4 Hz, for the values of amplitudes attained in the experiment, should occur according to the linear formulae. This was confirmed by experiments with waves at these frequencies: the geometry of surface wave anomalies and the values of δa were almost independent of the amplitudes of the generated surface waves. Experiments at frequency of 3.4 Hz were carried out only for one value of surface wave amplitude. Therefore, the nonlinearity effect, i.e., the dependence of the surface wave anomalies on amplitude, is considered here for the case of $f = 2.9$ Hz. Results of experiments with a smaller sphere are presented in Fig. 1.11: (a) data of acoustic sensors for the average amplitude of surface waves of 0.4 mm, (b) the corresponding data from the video system, (c) data of acoustic sensors, for the average amplitude of surface of 1.1 mm, and (d) data of the video system corresponding to Fig. 1.11 (c). The value of R was again 6 m for experiments employing acoustic sensors and 5 m for experiments using the video system. One can see from the figure that the increase of the average amplitude of surface waves leads to their increased variability, and regions of pronounced variation of a shift forward. Increased variability of surface wave amplitude due to their nonlinearity was obtained earlier theoretically [5]. The shift of surface wave anomalies forward is, evidently, associated with the increase of the group velocity of surface waves as their amplitude increases.

Results of experiments with a large sphere are shown in Fig. 1.12. The experiments were carried out employing acoustic sensors at a distance $R = 8.5$ m. The average amplitude of surface waves in the region of the measurements was 0.85 mm (a) and 2.1 mm (b). In both cases, δa attained large values; the only difference was in the structure of the surface wave anomalies. The larger the surface wave amplitude, the more complicated is the pattern of its variability. Apparently, small-scale instability of the surface wave envelope started to develop in the experiment depicted in Fig. 1.12 (b).

Note in conclusion that, depending on the frequency, amplitude and propagation time, surface waves demonstrate a very diverse set of anomalies in the field of the flow around a moving sphere. Therefore, of particular interest is a more detailed comparison of experimental data and theoretical results, which will be attempted in the next stage of this work.

2. NUMERICAL INVESTIGATIONS OF GRAVITY-CAPILLARY SURFACE WAVE TRANSFORMATION ON INHOMOGENEOUS FLOW. COMPARISON WITH TANK EXPERIMENTS

2.1 Formulation of the problem

Computations were carried out on the basis of the equations derived at the first stage of research for complex amplitude A of nonlinear gravity-capillary surface waves in the field of a localized perturbation $\mathbf{u}(x, y)$ of the constant surface current (main stream) $-U_0\mathbf{x}_0$:

$$\frac{\partial A}{\partial \tilde{t}} = 2iL\,A + (1-\beta_x)\frac{\partial A}{\partial \tilde{x}} - \beta_y \frac{\partial A}{\partial \tilde{y}} + i\left[(\beta_x - 1)\tilde{k}_{x0} + \beta_y \tilde{k}_{y0} - \tilde{\omega}_0\right]A +$$
$$+ \frac{ic}{2}\tilde{k}_0^{\,2}\sqrt{\tilde{k}_0 + \tilde{T}\tilde{k}_0^{\,3}}\,|A|^2 A - \frac{\eta}{4}\tilde{k}_0\sqrt{\tilde{k}_0 + \tilde{T}\tilde{k}_0^{\,3}}\,A^2\frac{\partial A^*}{\partial \tilde{x}} + \qquad (2.1)$$
$$+ \frac{\nu}{4}\tilde{k}_0\sqrt{\tilde{k}_0 + \tilde{T}\tilde{k}_0^{\,3}}\,|A|^2\frac{\partial A}{\partial \tilde{x}} + i\tilde{k}_0 A\frac{\partial \overline{\Phi}}{\partial \mathbf{r}_{k0}} \quad ,$$

where $|A| = 2ak_*$ is the dimensionless wave amplitude; $\tilde{t} = t\,k_* U_0$, $\tilde{x} = xk_*$, and $\tilde{y} = yk_*$ are dimensionless time and coordinates; $k_* = \dfrac{g}{4U_0^{\,2}}$, $\boldsymbol{\beta} = \dfrac{\mathbf{u}}{U_0}$, $\tilde{T} = \dfrac{Tg}{16U_0^{\,4}}$, T is the surface tension coefficient normalized to the water density; and $\tilde{\mathbf{k}}_0 = \dfrac{\mathbf{k}_0}{k_*}$, $\tilde{\omega}_0 = 2\sqrt{\tilde{k}_0\left(1 + \tilde{T}\tilde{k}_0^{\,2}\right)} - \tilde{k}_{x0}$ are the parameters of the unperturbed surface wave incident on inhomogeneous flow;

$$L\,J = \frac{1}{2\pi}\int \exp\left(i\left(k_x'\tilde{x} + k_y'\tilde{y}\right)\right)\cdot$$
$$\cdot\left[\left(\left(\tilde{k}_{x0} + k_x'\right)^2 + \left(\tilde{k}_{y0} + k_y'\right)^2\right)^{\frac{1}{2}} + \tilde{T}\left(\left(\tilde{k}_{x0} + k_x'\right)^2 + \left(\tilde{k}_{y0} + k_y'\right)^2\right)^{\frac{3}{2}}\right]^{\frac{1}{2}} \tilde{J}\left(k_x', k_y'\right) d\,k_x' d\,k_y' \quad ,$$

$\tilde{J}\left(k_x', k_y'\right)$ is the Fourier transform of the function J,

$$\tilde{J}\left(k_x', k_y'\right) = \frac{1}{2\pi}\int \exp\left(-i\left(k_x'\tilde{x} + k_y'\tilde{y}\right)\right) J(\tilde{x}, \tilde{y})\, d\,\tilde{x}\, d\,\tilde{y}\,,$$

$$c = \frac{8 + R^2 + 2R^4}{16(1+R^2)(1-2R^2)}; \qquad \eta = \frac{(1-R^2)(8+R^2+2R^4)}{16(1-2R^2)(1+R^2)^2} = \frac{1-R^2}{1+R^2}c;$$
$$\nu = \frac{3(4R^8 + 4R^6 - 9R^4 + R^2 - 8)}{8(1+R^2)^2(1-2R^2)^2}; \qquad R = \sqrt{\tilde{T}}\tilde{k}_0,$$

$\mathbf{r}_{k0}$ is the direction of $\mathbf{k}_0$, and $\dfrac{\partial \overline{\Phi}}{\partial \mathbf{r}_{k0}}$ is determined from the set of equations

$$\Delta\overline{\Phi} = 0$$
$$\frac{\partial \overline{\Phi}}{\partial z} = \frac{\sqrt{\tilde{k}_0 + \tilde{T}\tilde{k}_0^{\,3}}}{4}\frac{\partial}{\partial \mathbf{r}_{k0}}\left(|A|^2\right).$$

Expressions for β_x and β_y are readily obtained from (1.1) by substituting $z = 0$:

$$\beta_x = r^3 k_*^{\,3}\frac{2\tilde{x}^2 - \tilde{y}^2 - \tilde{h}^2}{\left(\tilde{x}^2 + \tilde{y}^2 + \tilde{h}^2\right)^{5/2}} \qquad \beta_y = r_s^{\,3} k_*^{\,3}\frac{3\tilde{x}\tilde{y}}{\left(\tilde{x}^2 + \tilde{y}^2 + \tilde{h}^2\right)^{5/2}} \quad ,$$

where $\tilde{h} = hk_*$ is the dimensionless depth of submersion of the sphere, and $r^3k_*^3$ is its dimensionless radius.

Equation (2.1) was used to calculate the temporal evolution of the surface waves with initially constant wave vector $\mathbf{k}_0$ and amplitude a_0 under the perturbation of the main stream, β, arising at a certain moment of time, $t = 0$. The values of the parameters r, h, U_0, and k_{x0} were taken directly from the experiment described in Sec. 1 of this report ($k_{y0} = 0$ in all the experiments). Calculations were made up to the time $t = R/U_0$, where R is the distance from the wave maker of surface waves to the plane of acoustic sensors or video system.

The choice of the value of a_0 was a non-trivial problem. As was shown at the first stage of the research, surface waves may significantly attenuate in the course of propagation, whereas theoretically it was assumed constant. Therefore, for a rough description of nonlinear effects we used the value of wave amplitude in the region of measurements to calculate the surface wave amplitude a_0 at the halfway point, i.e., distance $R/2$ from the wave maker by using the damping coefficients obtained at the first stage of the research [8] as an average for the entire interaction region. Certainly, the choice of a_0 is of no importance when surface waves are weak enough to demonstrate linear behavior. For waves of higher amplitude, several rather close values of a_0 were specified to evaluate the influence of this parameter on the results of the calculations.

Calculations were made in a region 4 m x 4 m in size. For the cases when surface wave anomalies expand rapidly and are outside this region, the latter was expanded to a region 8 m x 8 m. These cases will be specially qualified. In the figures 2.1 to 2.10 discussed below, the quantity δa is shown in color in accord with the scale bar in each figure. Note, that Results of theoretical calculations and the data of experiments will be compared in a sequence different from that in Sec. 1, namely, from lower to higher frequencies of surface waves.

2.2. Transformation of surface waves with frequency $f = 2$ Hz

Experiments have shown that the variability of surface wave amplitude is insignificant at this frequency (see Figs. 1.6a and 1.7a discussed above in this chapter). Theoretical calculations also gave only small values of δa. Results of calculations for the conditions specified in Fig. 1.6a are illustrated in Fig. 2.1. Since the group velocity of these surface waves is much higher than U_0, perturbations of their amplitude rapidly propagate forward so that Fig. 2.1 was plotted for a region 8 m x 8 m. The range of variations of δa, 0.9752 to 1.0258, obtained in the calculations, is too small to record in experiments. Therefore, comparison of the structures of surface wave anomalies in Figs. 1.6a and 2.1 has not been made.

2.3. Transformation of surface waves with frequency $f = 2.4 - 2.5$ Hz

We begin here with the case of a small sphere. Results of computations corresponding to experimental data shown in Fig. 1.4a are given in Fig. 2.2a. The structure of surface wave anomalies in theoretical calculations and in the experiment have similar features as well as pronounced differences. The region of maximal values of δa in the experiment is slightly shifted in the $-\mathbf{x}$ direction with respect to the corresponding region in the calculations. The calculated range of variation of δa was four times less than in the experiment. Control calculations for a 1.3-fold value

of a_0 were made (surface waves must have this amplitude directly near the wave maker), and their results nearly coincided with those presented in Fig. 2.2a. Consequently, in this region of the parameters, surface wave nonlinearity is unessential, and we had no reason for a further increase of a_0 in calculations.

An interesting peculiarity of the obtained theoretical results is that, notwithstanding the fact that the group velocity of surface waves exceeds the value of U_0, their amplitude anomaly is observed in the region $x<0$. A possible cause is that for a small size of flow inhomogeneity, (large $\frac{\partial \beta_x}{\partial x}$), backward scattering of the wave becomes essential. In this case, one of the conditions (namely, that the wavelength is much smaller than the characteristic spatial scale of the inhomogeneous flow) under which Eq. (2.1) was derived is violated for the parameters used in the calculations. Therefore, we made control calculations employing an equation obtained in [5] for the complex amplitude of linear surface waves without supposition of the smallness of their wavelength:

$$D_0^{-\frac{1}{2}}\left(i\sqrt{gk_*}+B_0\right)^2 A + B_1 D_0^{-\frac{1}{2}}\left(i\sqrt{gk_*}+B_0\right)A + \\ +\left(i\sqrt{gk_*}+B_0\right)D_0^{-\frac{1}{2}}B_1 A + B_1 D_0^{-\frac{1}{2}}B_1 A + gA = 0, \qquad (2.2),$$

where

$$B_0 = \frac{\partial}{\partial t} - U_0\frac{\partial}{\partial x}$$

$$B_1 = -ik_* u_x + u_x\frac{\partial}{\partial x} + u_y\frac{\partial}{\partial y}$$

$$D_0^{-\frac{1}{2}} f(x,y) = \frac{1}{(2\pi)^2}\int e^{i(k_x x + k_y y)}\frac{\hat{f}(k_x,k_y)}{\sqrt{(k_x-k_*)^2+k_y^2}}dk_x dk_y .$$

In contrast to (2.1), equation (2.2) is written in dimensional form and is derived under the assumption only that the liquid surface slope due to inhomogeneous flow is small. Results of the calculations are shown in Fig. 2.2b. They are close to the ones depicted in Fig. 2.2a: the structure of surface amplitude distribution in Fig. 2.2b is similar to that in Fig. 2.2a, but the spatial range of variation of δa is slightly broader. Evidently, we can use Eqs. (2.1) in calculations for the parameters typical of our experiments.

Results of calculations for a large sphere are given in Figs. 2.3 and 2.4. Figure 2.3a corresponds to Fig. 1.9a (R = 3.5 m), and Fig. 2.3b, corresponds to Fig. 1.9b (R = 6 m). Results of calculations for R = 8.5 m are similar to those shown in Fig. 2.3b; therefore, they are omitted. Unlike the results of calculations for experiments with a small sphere, the changes in the surface wave amplitude are observed only in the region $x>0$, as expected from the physical consideration. Presumably, this is due to a smaller gradient of the inhomogeneous flow so that there is no backscattering. In this case, surface wave anomalies expand rapidly, so that Figs. 2.3b and 2.4 corresponding to R = 6 m were calculated and plotted in a region 8 m x 8 m.

Similar to experiments with a small sphere, the range of variation of δa in calculations is four to five times less than in the experiment. At the same time, the geometry of surface wave amplitude anomalies in space is similar in calculations and in the experiment. The only difference is that in calculations the regions of increasing and decreasing of a are larger in size and are shifted forward in the **x** - direction.

To elucidate the influence of nonlinearity of surface waves on their transformation in the field of flow around the sphere, we carried out calculations for different values of a_0. A pronounced increase of the range of variation δa was obtained when the value of a_0 was increased by a factor of 1.75 compared to that calculated by the method described above (see Fig. 2.4). In this case, the range of variation δa is much closer to the one recorded in the experiment.

Overall, results of calculations for surface waves with a frequency 2.5 Hz, along with an agreement in spatial geometry, still have some significant differences when compared with the data of the experiments. We intend to determine the cause of this discrepancy in our further research.

2.4. Transformation of surface waves with frequency $f = 2.9$ Hz

The group velocity of surface waves with frequency 2.9 Hz is close to the velocity of the sphere motion. Therefore, it is natural to expect significant changes in the surface wave amplitude, even in the field of weak inhomogeneous flow around a moving sphere. Results of numerical computations confirm this supposition. Figure 2.5 shows the results of calculations corresponding to Fig. 1.4 (b) (experiment with a small sphere, $R = 6$ m). The ranges of variation δa in calculations and in the experiment have no pronounced differences, and the structures of the field of variation of surface wave amplitude have much in common. Calculations for smaller values of a_0 verify that the influence of surface wave nonlinearity is not essential. Such a significant variability of the characteristics of surface waves is a result of their closeness to the condition of synchronism. Results of calculations for larger values of a_0, which correspond to Figs. 1.11 (d) and 1.11 (c), are presented in Fig. 2.6. The influence of surface wave nonlinearity leads to still greater variability of their amplitude, which even exceeds that obtained in experiments. Besides, the structure of surface wave anomalies changes in this case faster than that of linear surface waves. Parameter R for Figs. 2.6 (a) and 2.6 (b) is equal to 5 m and 6 m, respectively. Nevertheless, the spatial distribution of surface wave amplitude is different in these figures. It is worth noting that the range of variation δa in Fig. 2.6 (b) is less than in Fig. 2.6 (a), i.e., it decreases with increasing R.

In calculations of the transformation of surface waves with $f = 2.9$ Hz, we investigated how different terms of Eq. (2.1) affect the results. As mentioned above, surface wave nonlinearity can lead to increased variability of amplitude. Allowance for the effects of capillarity in surface waves and for their nonlinear dispersion weakly affects the range of variation δa, but it changes the structure of spatial distribution of a. In the absence of terms responsible for nonlinear dispersion, allowance for capillary effects does not change the results of computations. In the absence of the capillary effects ($T = 0$ in Eq. [2.1]), allowance for nonlinear dispersion of surface waves leads to a decrease in the small-scale variability of their amplitude, small regions of increasing and decreasing a disappear, but the principal surface wave anomalies retain their position. It was somewhat unexpected that allowance for the effects of capillarity with retained nonlinear dispersion (i.e., all terms in Eq. (2.1) were retained) again gives small-scale variability of surface wave amplitude. The shape of the surface wave anomalies for $x < 0$ in Fig. 2.6 (b) is a consequence of allowance for the effects of capillarity. The position of the main regions of increasing and decreasing a also changes in this case.

Results of calculations for experiments with a large sphere are given in Fig. 2.7. Figure 2.7 (a) corresponds to $R = 3.5$ m (Fig. 1.6 (c) in the experimental part), and Fig. 2.7 (b) to $R = 6$ m (Fig. 1.7 (c) in the experiment). In the course of propagation of surface waves, the variability of their amplitude increases, and the region of space occupied by surface wave anomalies grows in size. Although the velocity with which the range of variation δa increases in calculations more slowly than in the experiment, it becomes as large as in the experiment with increasing R. For $R = 3.5$ m,

the maximal values of the change of surface wave amplitude in calculations are smaller than in the experiment, but they become equal for $R = 6$ m. The structures of spatial distribution of surface wave amplitude in calculations and in the experiment are also similar.

A distinctive feature of this case is a weakly increasing variability of surface wave amplitude with increasing a_0. The results of calculations presented in Fig. 2.8 correspond to those shown in Fig. 2.7 (b), but the value of a_0 is five times higher. The surface wave nonlinearity resulted in the shift of the region of variation of a in the direction x as a consequence of the increase of the group velocity of surface waves, but the range of variation δa increased only slightly. Evidently, the condition of synchronism of surface waves with the velocity of motion of inhomogeneous flow determines the depth of modulation of a, and the surface wave nonlinearity affects, primarily, the position of the regions of increasing and decreasing a.

2.5. Transformation of surface waves with frequency $f = 3.3 - 3.5$ Hz

Results of theoretical calculations corresponding to Fig. 1.4c (small sphere) are presented for two values of initial wave amplitude a_0: for the value calculated by the method described above (Fig. 2.9a) and for twice as large a_0 (Fig. 2.9b). In the first case, the range of variation δa was less than in the experiment, and in the second case it was slightly greater. The structure of spatial distribution of surface wave amplitude shown in Fig. 2.9b is close to the one obtained in the experiment; even some details coincide.

Results of calculations for the large sphere are presented in Fig. 2.10 (cf. Fig. 1.6d). Since the group velocity of surface waves is smaller than U_0, the regions of their amplitude anomalies are past the sphere; this shift is larger in the experiment than in theory. Regions of the minimal a lie above and under the $y = 0$ axis both in calculations and in the experiment. The range of variation of δa in calculations is approximately 1.5 times smaller than in the experiment. In this case, the potentialities of our computers did not allow us to perform calculations for larger values of a_0.

Comparison of numerical results and data of experiments shows that the proposed model of surface wave transformation in the field of an inhomogeneous flow created by a moving object provides a satisfactory description of its principal regularities. At the same time, there are certain discrepancies between theoretical and experimental results. In particular, the variation of surface wave amplitude was usually smaller in calculations than in the experiment. This discrepancy will be analyzed in further research.

CONCLUSION

To conclude, we present the principal results of the research done at both stages of this project.

An equation for the complex amplitude of nonlinear surface waves in the presence of two-dimensional flow perturbations has been derived, which takes into account the total linear dispersion of capillary-gravity waves by means of an integral-differential operator and the nonlinear dispersion caused, in particular, by the flow produced by surface waves. Analysis of spatial perturbations of the surface wave amplitude within the framework of this equation shows that allowance for nonlinear dispersion leads to limitation of the small-scale numerical instability and significantly extends the applicability of our calculations.

We developed an algorithm of a numerical solution to the equation describing the influence of inhomogeneous flows on the propagation of gravity-capillary waves. Using this algorithm, software was created that enables us to investigate the time evolution of surface wave anomalies.

Spatial-temporal variability of surface wave amplitude in the field around a submerged sphere and in its absence was experimentally studied in a large thermostratified tank of IAP RAS. (Without a sphere, we measured the surface wave damping and showed that it is due to the presence of an elastic film on the water surface.) When the inhomogeneous streamline current around the sphere acted on surface waves, we recorded regions (anomalies) of decreasing and increasing amplitudes of these waves. With decreasing frequency of surface waves, these anomalies shift forward with respect to the sphere, i.e., in the direction of its motion. The largest changes in the amplitude were recorded for the waves whose group velocity is close to the velocity of sphere motion (group synchronism) or for higher frequency waves. The surface waves whose frequency differs strongly from its synchronous value transform only weakly. As the time of action of the flow on the surface wave grows, the regions of anomalies expand, and the magnitude of amplitude variation increases. It was shown that at the initial stage of development of surface wave anomalies, the condition of group synchronism is decisive, while at the stages to follow, surface wave instability due to nonlinearity may play the main role. In this case, fast development of wave amplitude variability is recorded.

The main features of surface wave transformation by flow around a submerged sphere obtained in theoretical calculations carried out for the conditions of the experiment, were analogous to those described above. The magnitude of changes and the structure of the two-dimensional distribution of the amplitude of surface waves, both under group synchronism and for higher-frequency waves, were close both in theory and in experiment. However, for lower frequencies the variations of the wave amplitude in calculations were smaller than in the experiment. Besides, calculations verified that at the stage of development of wave anomalies when nonlinearity is essential, the structure of the anomalies changes rapidly. Allowance for surface tension in surface waves leads to decreased variability scales of their amplitude.

Overall, in this new series of experiments and calculations, a scale modeling of rather realistic conditions in the upper ocean has been achieved. In particular, the wavelength of the affected waves could be of the same order as the characteristic dimension of a moving body or at least of the flow around it, which is characteristic of many situations. Surface wave modulation is evidently deep enough to produce anomalies in radar and radiometric signals, and the anomalies can be situated both behind and ahead of the moving object.

REFERENCES

1. Basovich, A. Ya., V. V. Bakhanov, S. D. Bogatyrev, V. I. Kazakov, O. N. Kemarskaya, V. I. Pozdnjakova, V. I. Talanov, and I. A. Shereshevskii, 1997. The influence of two-dimensional nonuniform currents on surface waves, Izv. Akad. Nauk SSSR. Fiz. Atmos. i Okeana, v. 33, no. 3, 371-376.
2. Bakhanov, V. V., K. A. Gorshkov, E. M. Gromov, O. N. Kemarskaya, L. A. Ostrovsky, V. V. Papko, V. I. Talanov, Yu. I. Troitskaya, S. N. Reznik, and I. A. Soustova, 1997. Laboratory Modeling and Theoretical Studies of Wave Processes in the Ocean. Part 2: First Stage Results. Ed., L. A. Ostrovsky. Environmental Technology Laboratory, Boulder, CO, ERL, NOAA, 65 pp.
3. Bakhanov, V. V., I. S. Dolina, S. A. Ermakov, E. M. Gromov, V. V. Papko, V. I. Talanov, and Yu. I. Troitskaya, 1997. Laboratory Modeling and Theoretical Studies of Wave Processes in the

Ocean. Part 3: Second Stage Results. Ed., L. A. Ostrovsky. Environmental Technology Laboratory, Boulder, CO, ERL, NOAA, 88 pp.

4. Bakhanov, V. V., V. I. Kazakov, and O. N. Kemarskaya, 1998. The action of inhomogeneous currents on the fields of elevations and slopes of water surface nonlinear waves, 1998 International Geoscience and Remote Sensing Symposium Proceeding, v. 5, 2568-2570.
5. Bakhanov, V. V., and V. I. Talanov, 1999. Transformation of nonlinear surface waves in the field of inhomogeneous flows, In: Pripoverhnostnyi Sloi Okeana. Fizicheskie Processy i Distantsionnoe Zondirovanie (The Upper Layer of the Ocean. Physical Processes and Remote Sensing). Ed. V. V. Talanov and E. N. Pelinovsky. Nizhny Novgorod, v. 1, 81-106.
6. Arabadzhi, V. V., S. D. Bogatyrev, F. V. Golovanov, V. I. Kazakov, D. P. Korotkov, P. A. Matusov, L. A. Osrovsky, and D. V. Zaborskikh, 1993. Internal wave measurements in IAP Large termostratified tank. Part 1. Characterization of thermal stratification in the tank. Lawrence Livermore National Laboratory of the U. S. Department of Energy, 42 pp.
7. Bogatyrev, S. D., V. V. Bakhanov, I. S. Dolina, S. A. Ermakov, E. A. Gromov, L. A. Ostrovsky, V. V. Papko, V. I. Talanov, V. V. Titov, Yu. I. Troitskaya, and D. A. Zaborskikh, 1997. Laboratory Modeling and Theoretical Studies of Wave Processes in the Ocean. Part 1: Experimental Design and Program. Ed., L. A. Ostrovsky. Environmental Technology Laboratory, Boulder, CO, ERL, NOAA, 74 pp.
8. Chapter 1 of this Memorandum.

Figures to Chapter 2

In figures 1.4, 1.6, 1.7, 1.9-1.12, the real data from the acoustic sensors were obtained at only one side of the sphere motion axis and supplemented by the pattern "reflected" from the axis to give an idea of the full picture of perturbations and compare with theoretical patterns.

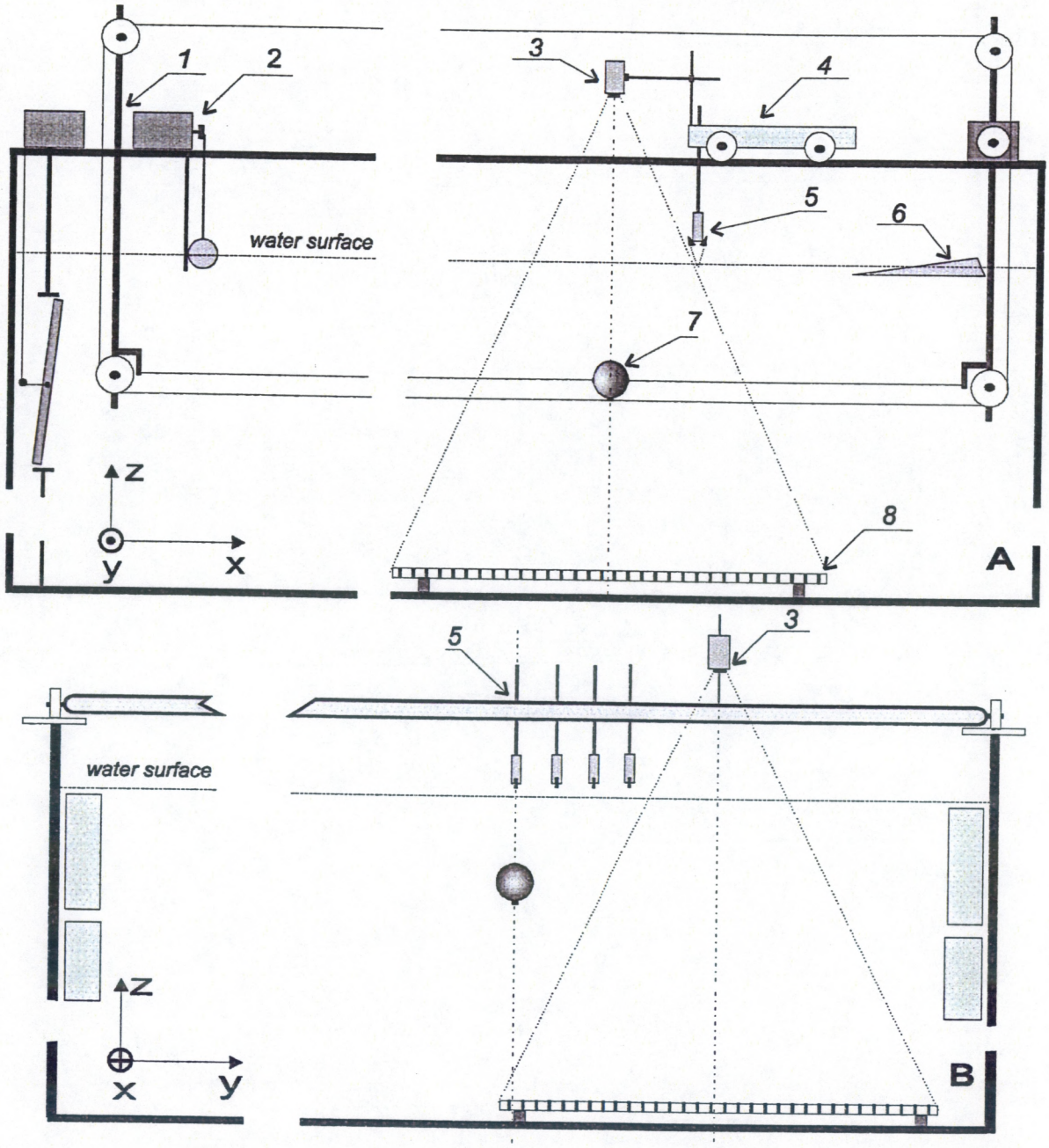

Fig. 1.1. General scheme of the experiment:
1 – system for rope towing of a sphere, 2 – wave maker of surface waves, 3 – video camera, 4 – self-propelled cart, 5 – utrasonic sensors, 6 –damper of surface waves, 7 – towed sphere (r = 4.25 cm or 9.5 cm, depth of submersion is $4r$), 8 – screen-grid. A – side view (*XZ*), B – back view of the tank (*YZ*).

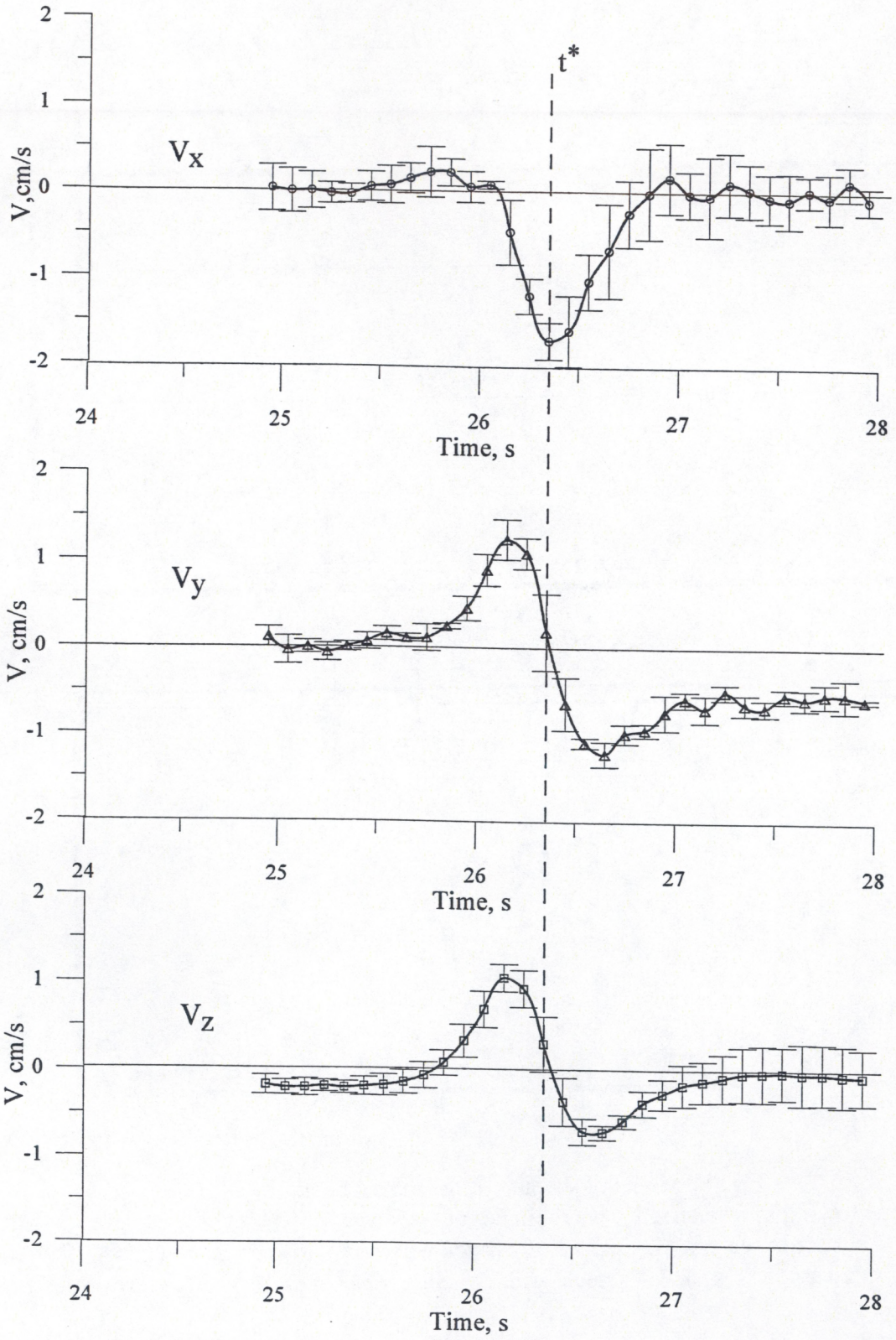

Fig. 1.2. Three velocity components of the flow around the sphere measured in experiment; t^* is the time when the sphere center crosses the plane of sensors.

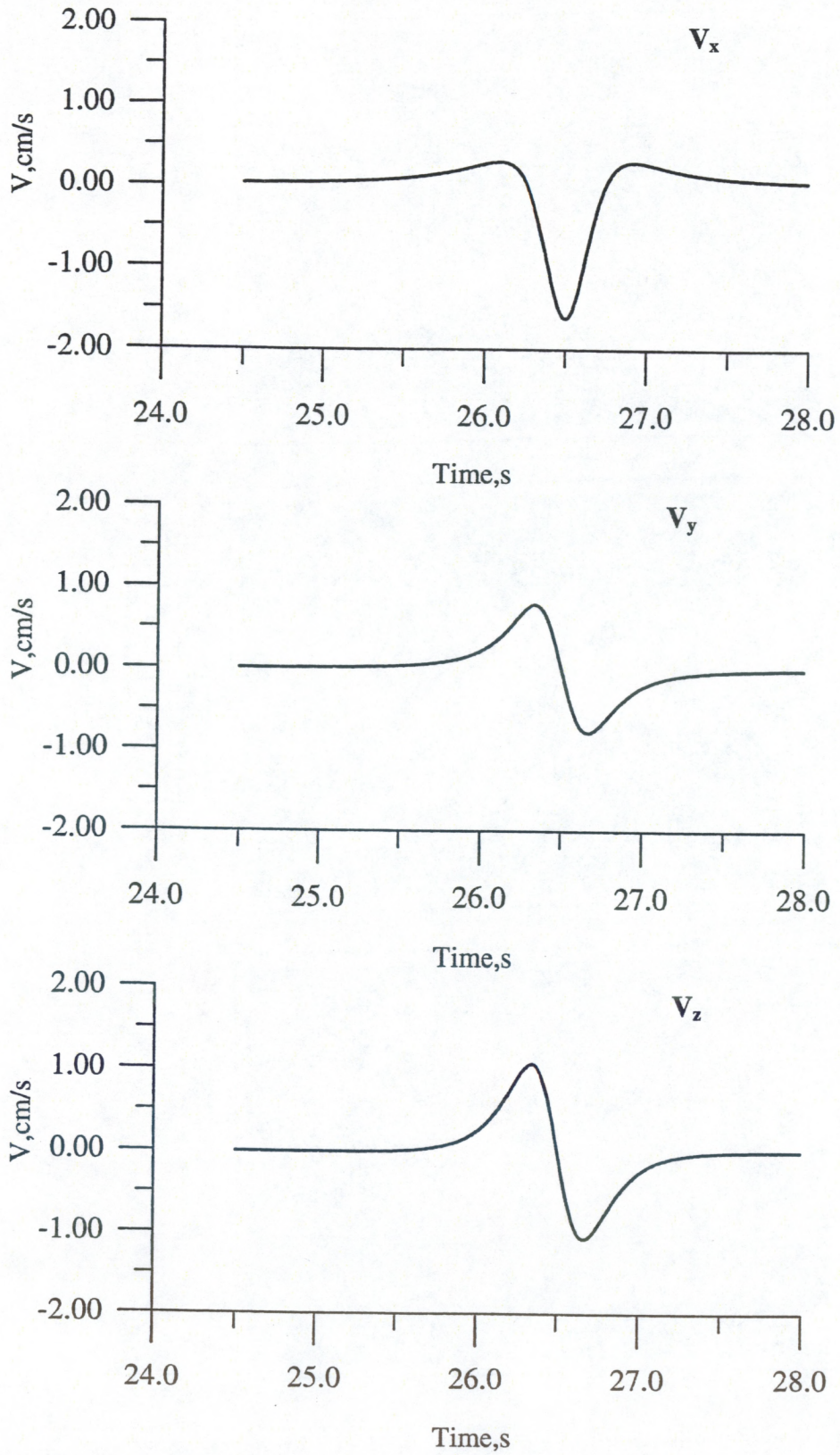

Fig. 1.3. Results of theoretical calculations corresponding to the experiment presented in Fig. 1.2.

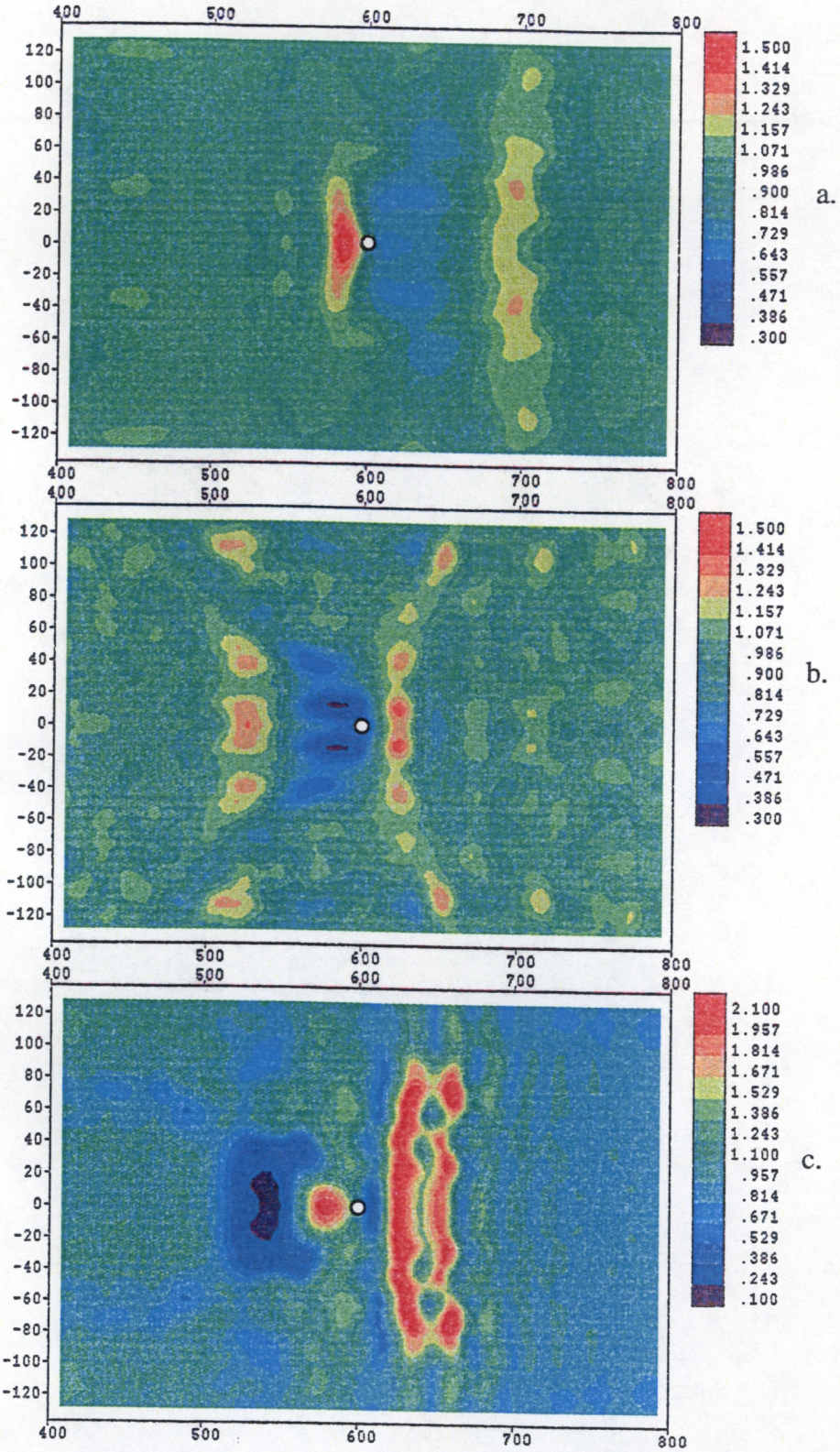

Fig. 1.4. Two-dimensional distributions of surface wave amplitude obtained by acoustic sensors for different surface wave frequencies: (a) f = 2.5 Hz, (b) f = 2.9 Hz , (c) f = 3.5 Hz; r = 4.25 cm, R = 6 m.

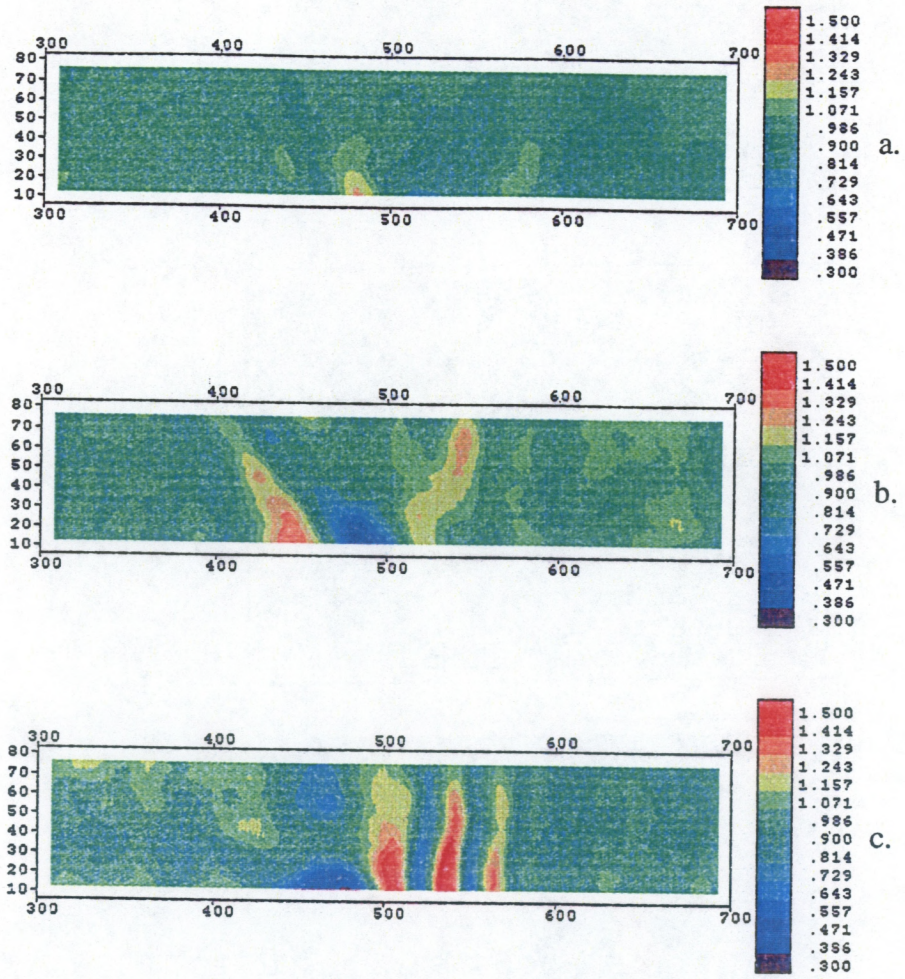

Fig. 1.5. Two-dimensional distributions of surface wave amplitude obtained by a video system for different surface wave frequencies: (a) f = 2.5 Hz, (b) f = 2.9 Hz, (c) f = 3.5 Hz; r = 4.25 cm, R =5 m.

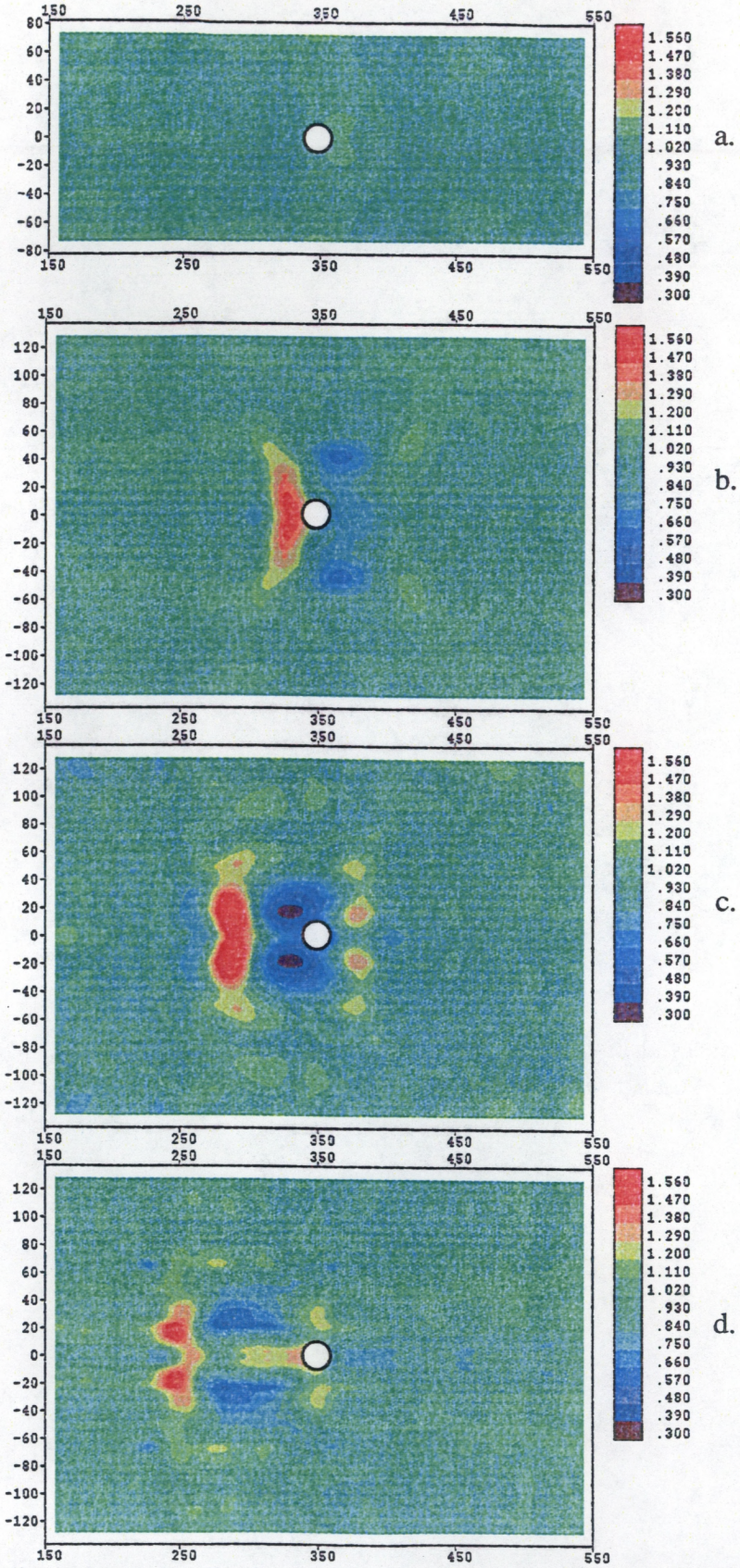

Fig. 1.6. Two-dimensional distributions of surface wave amplitude obtained by acoustic sensors for different surface wave frequencies: (a) f = 2.0 Hz, (b) f = 2.5 Hz , (c) f = 2.9 Hz, (d) f = 3.3 Hz; r = 9.5 cm, R = 3.5 m.

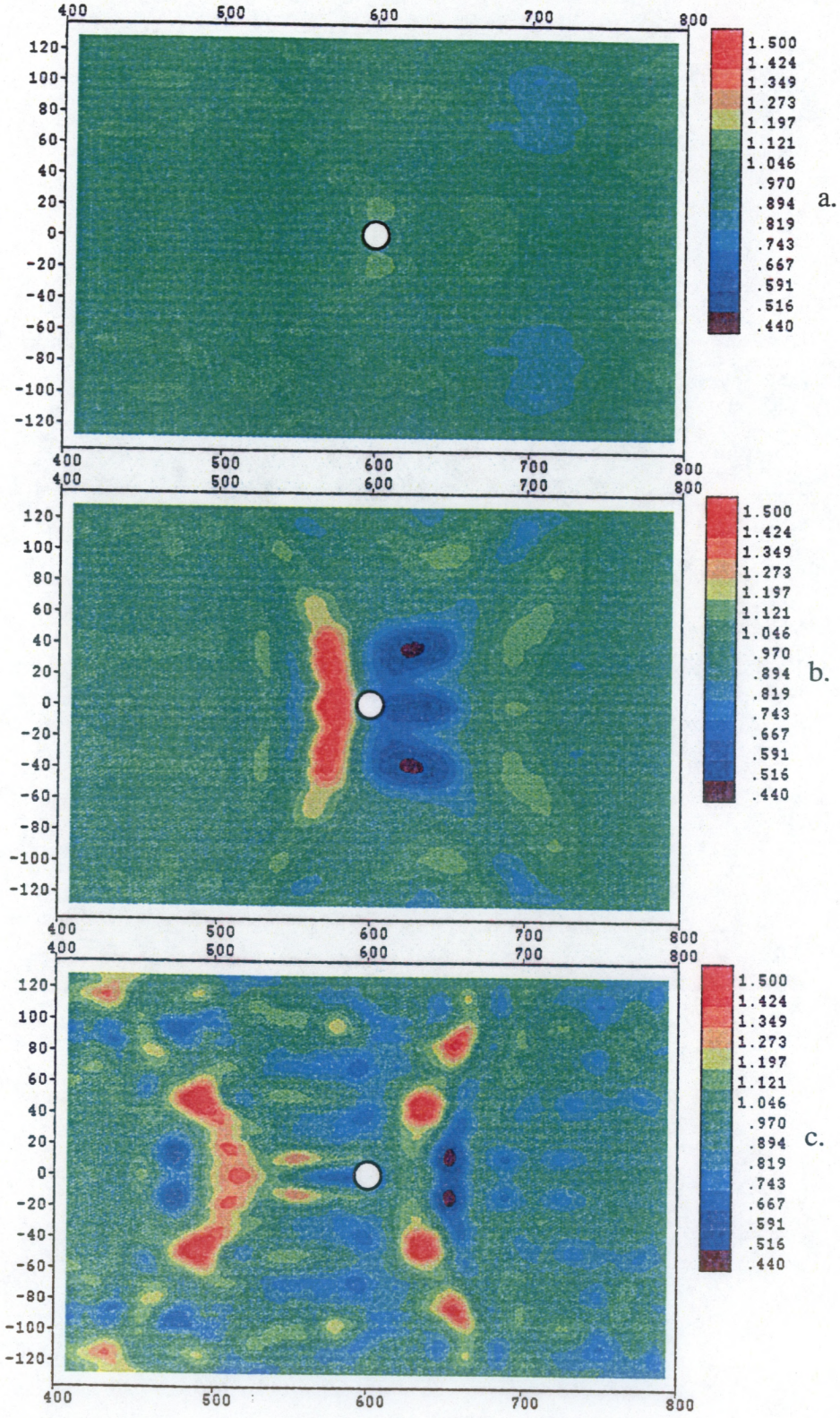

Fig. 1.7. Two-dimensional distributions of surface wave amplitude obtained by acoustic sensors for different surface wave frequencies: (a) f =2.0 Hz, (b) f = 2.4 Hz , (c) f = 2.9 Hz; r =9.5 cm, R =6 m.

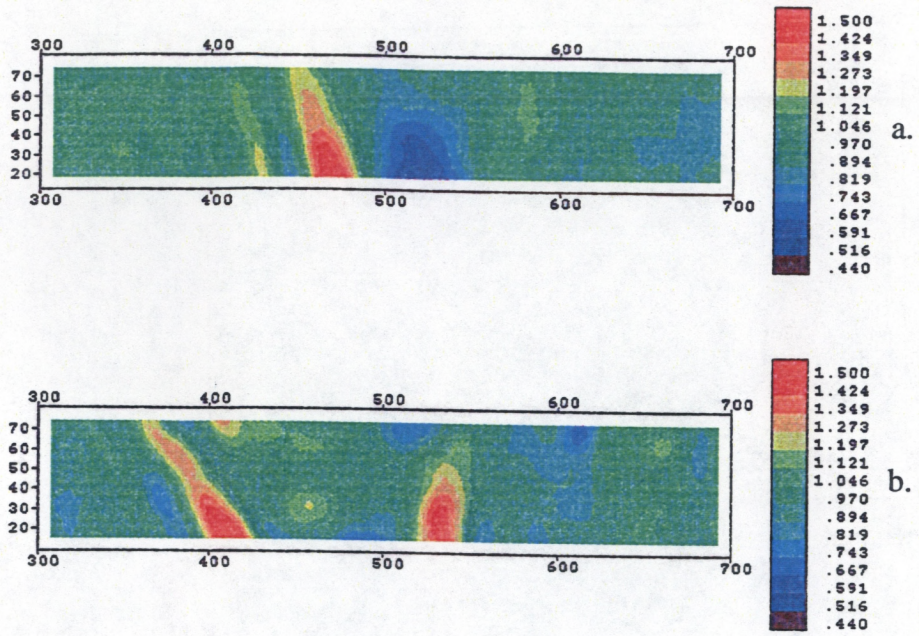

Fig. 1.8. Two-dimensional distributions of surface wave amplitude obtained by a video system for different surface wave frequencies: (a) $f = 2.4$ Hz, (b) $f = 2.9$ Hz; $r = 9.5$ cm, $R = 5$ m.

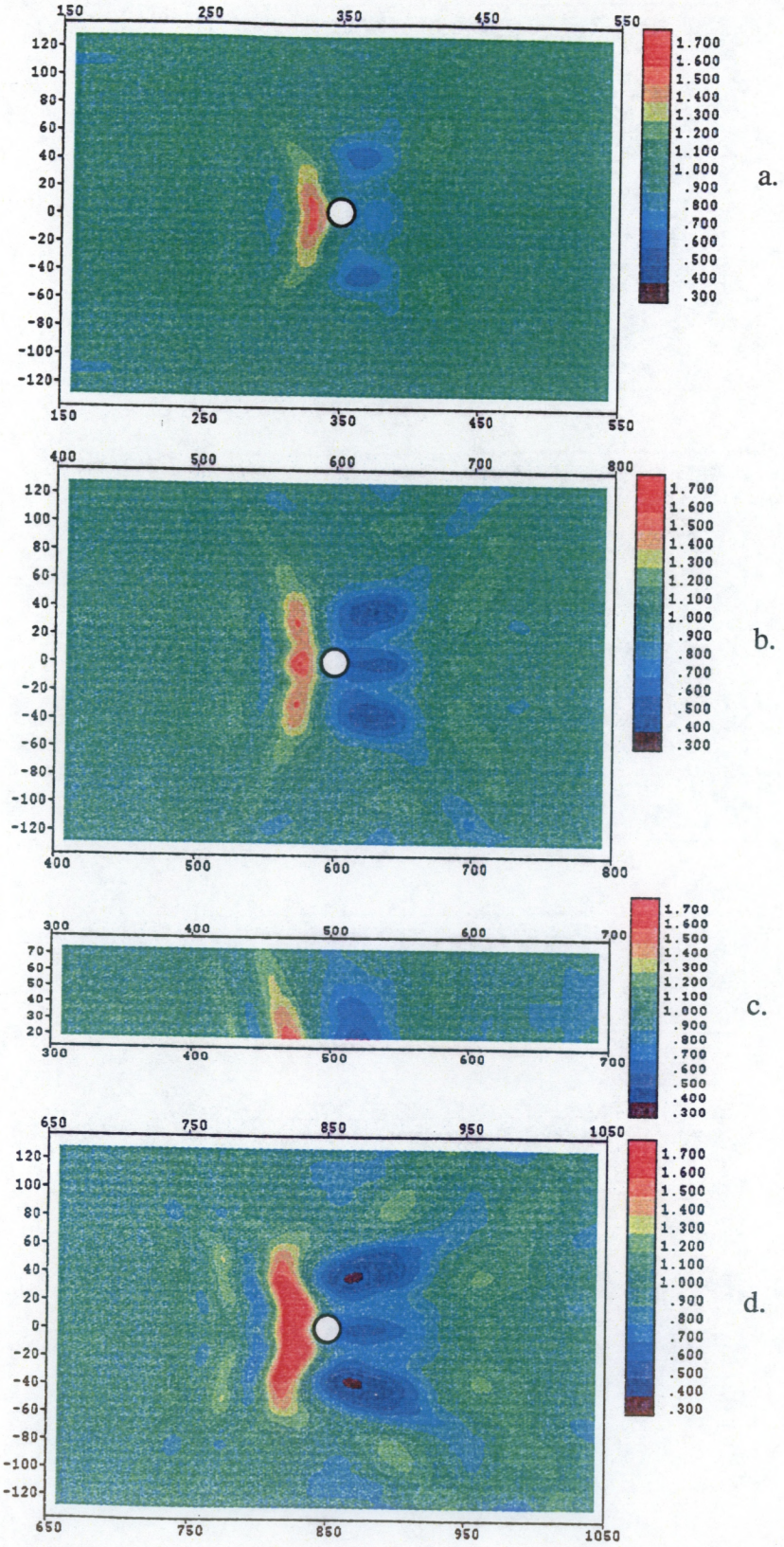

Fig. 1.9. Evolution of two-dimensional distribution of surface wave amplitude with increasing R: (a) R = 3.5 m, data of acoustic sensors; (b) R = 6 m, data of acoustic sensors; (c) R = 5 m, data of video system; (d) R = 8.5 m, data of acoustic sensors; r = 9.5 cm, f = 2.4 Hz.

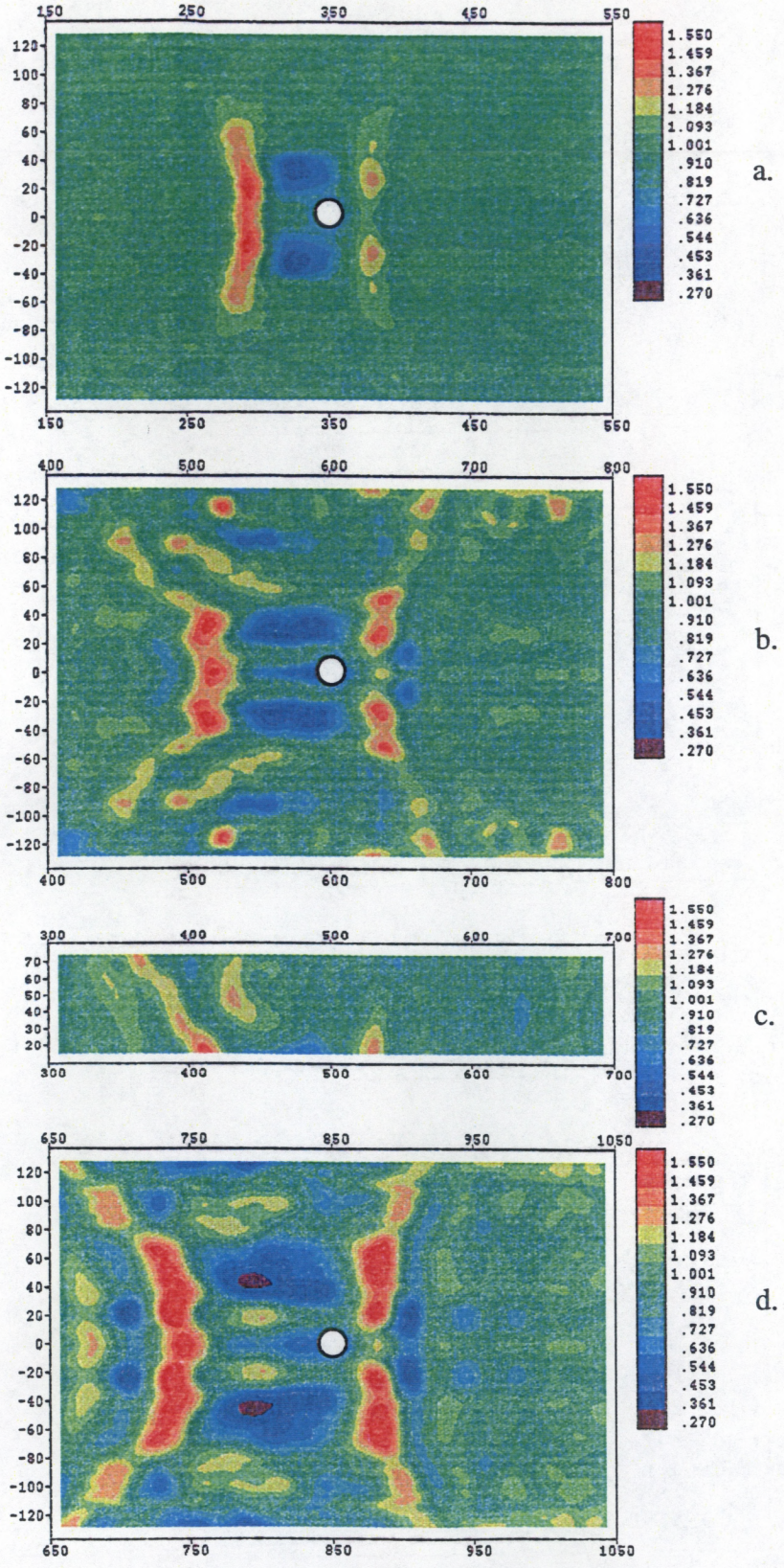

Fig. 1.10. Evolution of two-dimensional distribution of surface wave amplitude with increasing R: (a) R = 3.5 m, data of acoustic sensors; (b) R = 6 m, data of acoustic sensors; (c) R = 5 m, data of video system; (d) R = 8.5 m, data of acoustic sensors; r = 9.5 cm, f = 2.9 Hz.

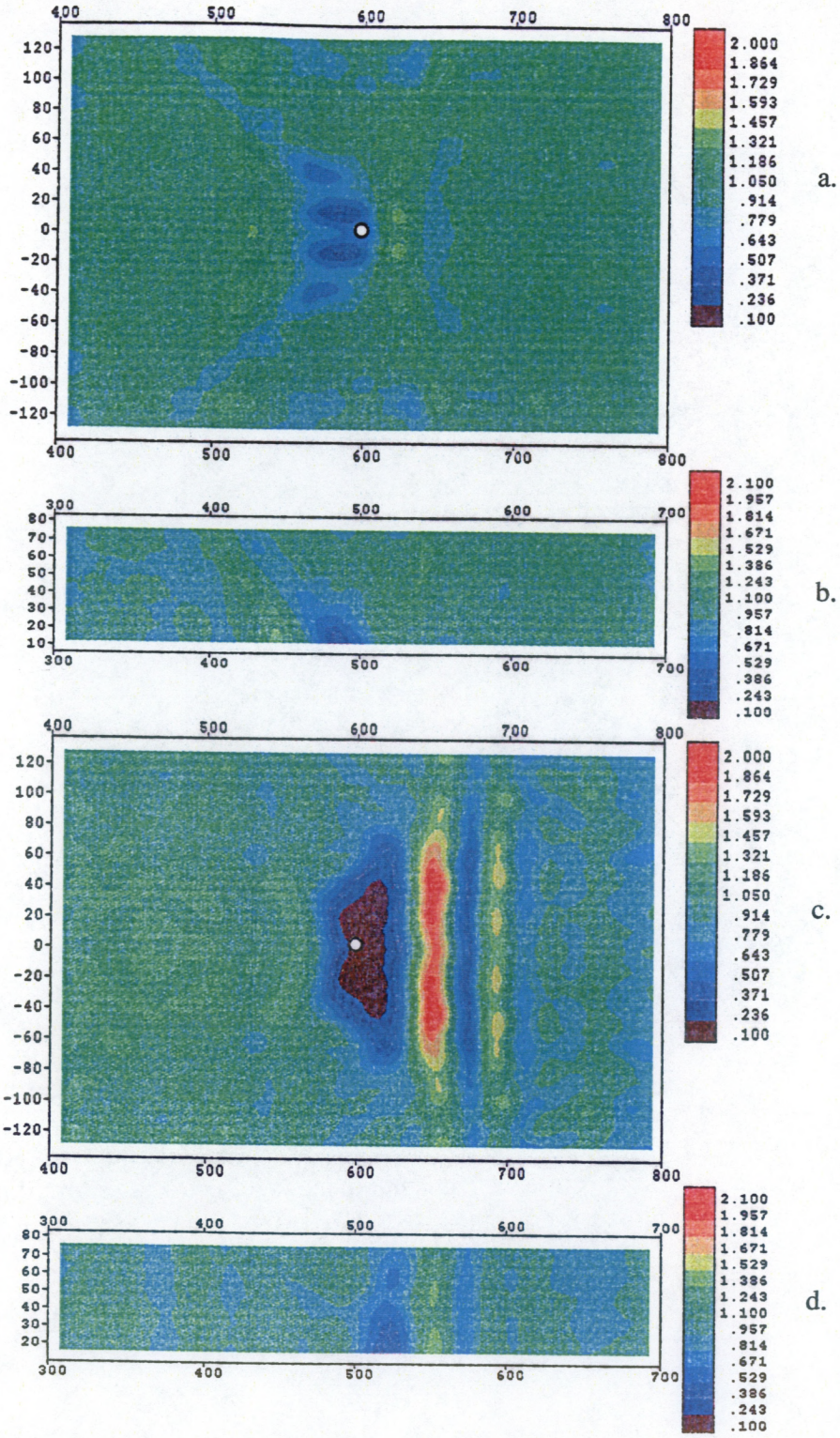

Fig. 1.11. Two-dimensional distributions of the amplitude of surface waves for different values of their unperturbed amplitude: For a 0.4-mm average amplitude of surface waves in the region of measurements: (a) R = 6 m, data of acoustic sensors, (b) R = 5 m, data of video system; For a 1.1-mm average amplitude of surface waves in the region of measurements: (c) R =6 m, data of acoustic sensors, (d) R =5 m, data of video system]; r =4.25 cm, f =2.9 Hz.

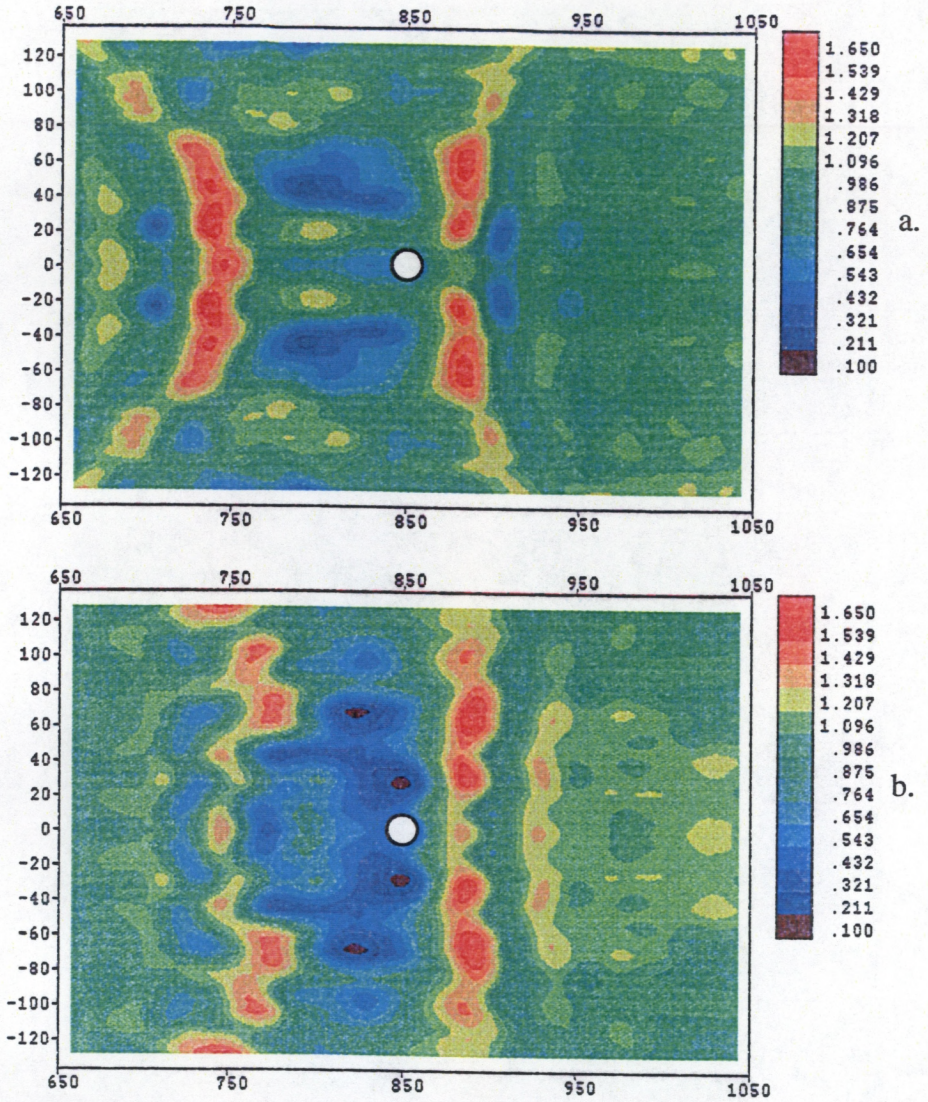

Fig. 1.12. Two-dimensional distributions of surface wave amplitude obtained by acoustic sensors for different values of an unperturbed amplitude: (a) the average amplitude of surface waves in the region of measurements is 0.85 mm, (b) 2.1 mm; r=9.5 cm, f = 2.9 Hz, R = 8.5 m.

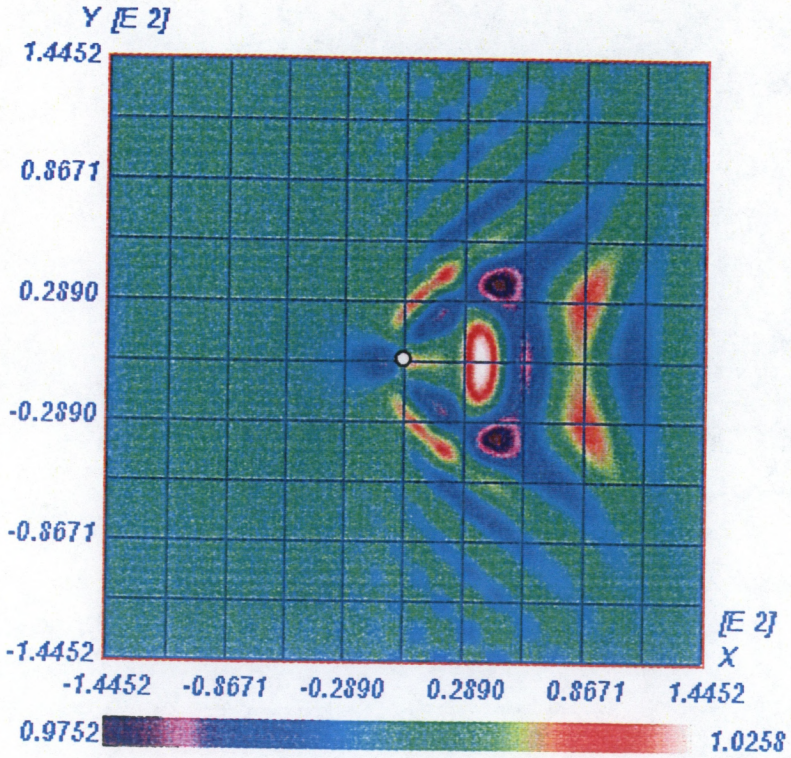

Fig. 2.1. Results of theoretical calculations for the region 8 m x 8 m corresponding to an experiment presented in Fig. 1.6a.

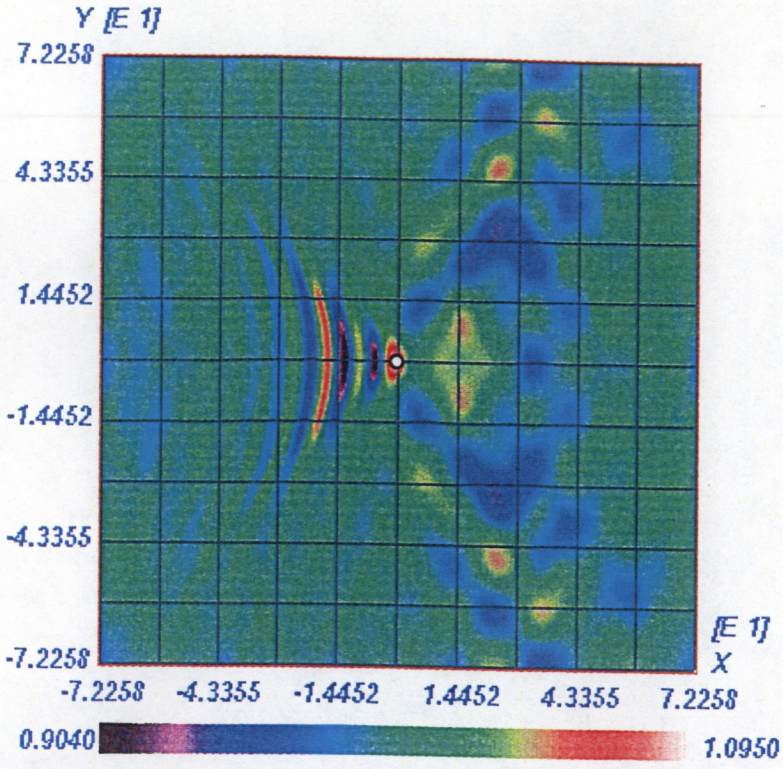

a.

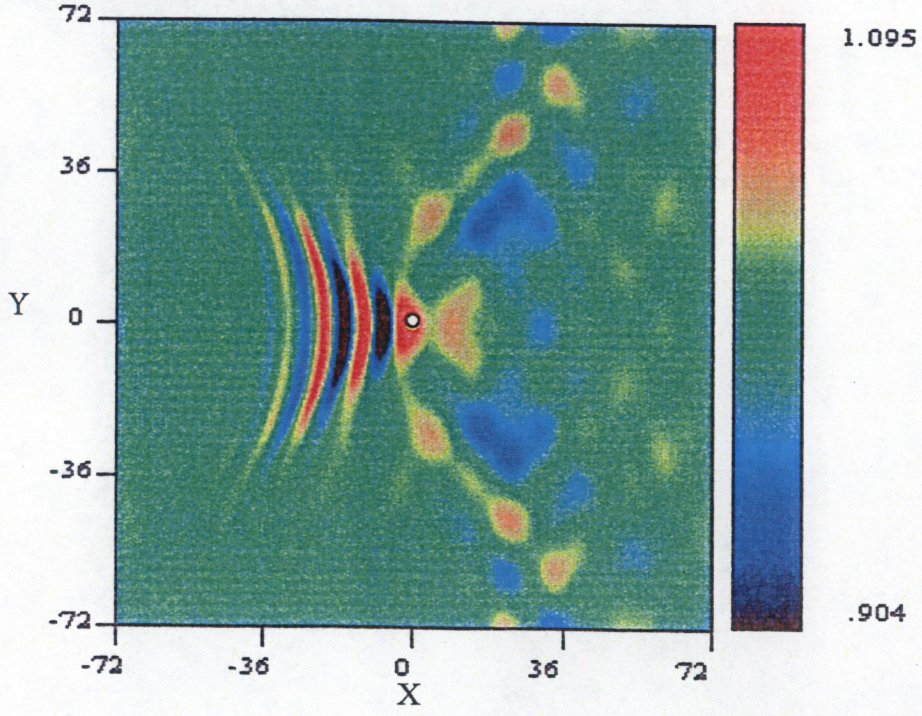

b.

Fig. 2.2. Results of the theoretical calculations for the region 4 m x 4 m corresponding to the experiment presented in Fig. 1.4a: (a) calculations using Eq. (2.1), (b) using Eq. (2.2).

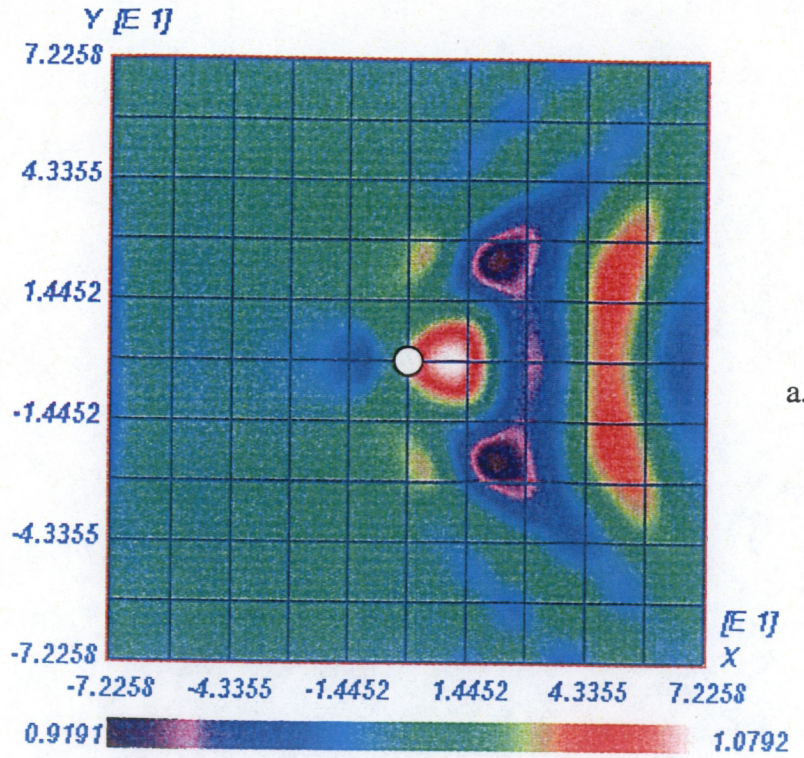

a.

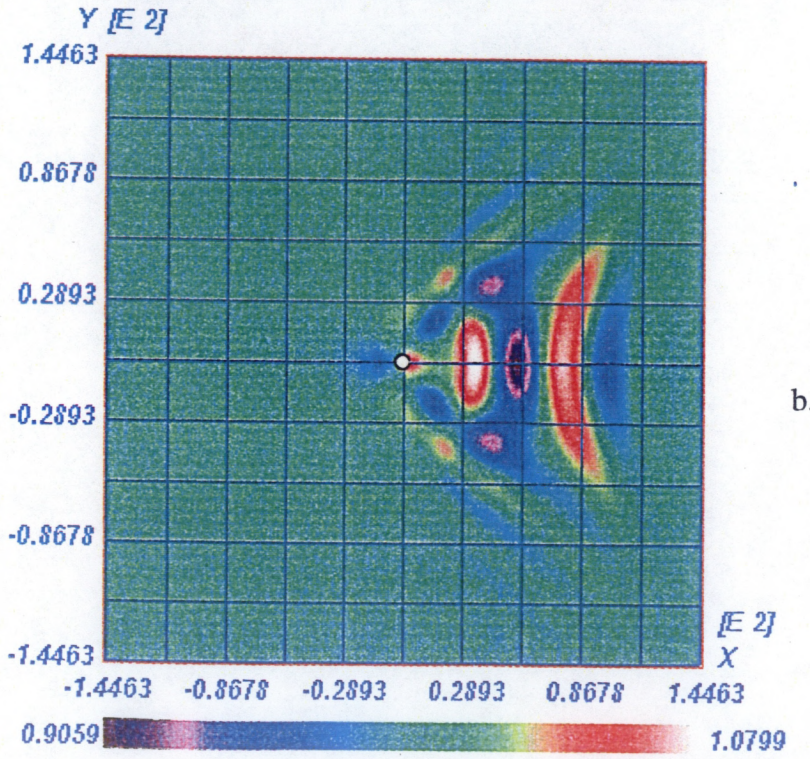

b.

Fig. 2.3. Results of theoretical calculations corresponding to experiments presented (a) in Fig. 1.9a (calculations for the region 4 m x 4 m) and (b) in Fig. 1.9b (for the region 8 m x 8 m). Sphere position is marked by a circle.

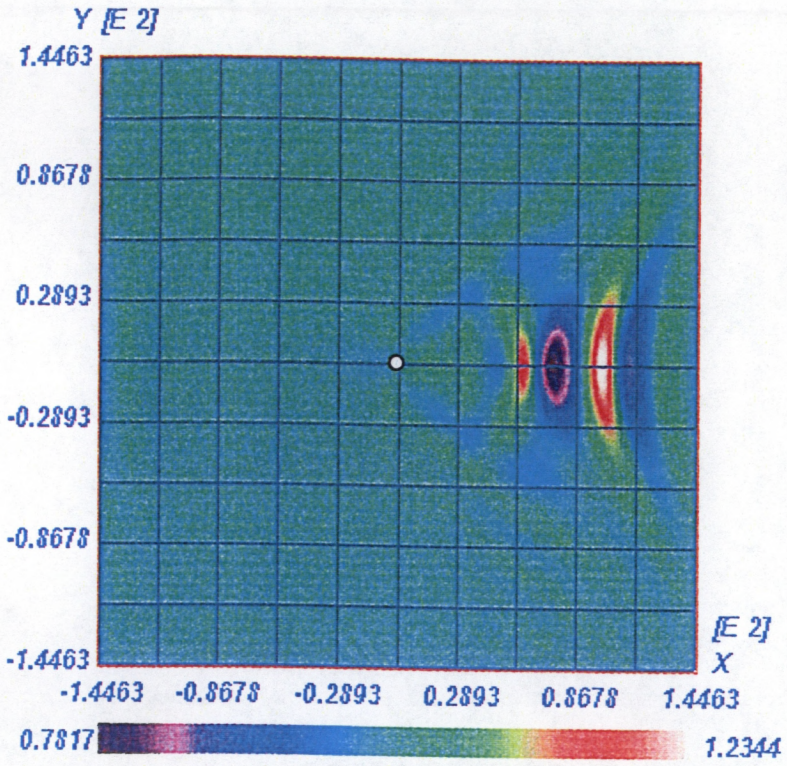

Fig. 2.4. Same as in Fig. 2.3b, with the value of a_0 increased 1.75 times.

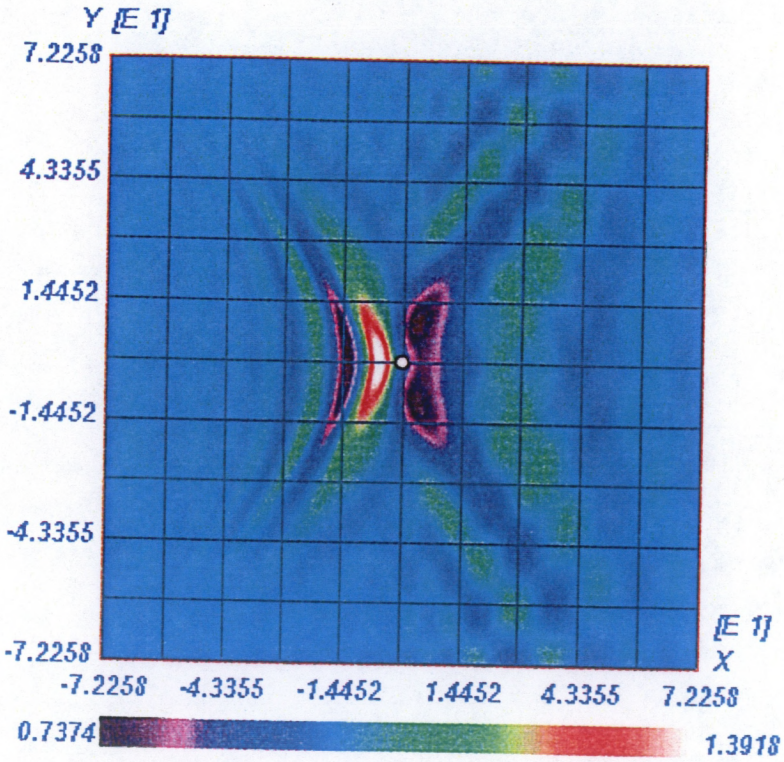

Fig. 2.5. Results of theoretical calculations for the region 4 m x 4 m corresponding to an experiment presented in Fig. 1.4b.

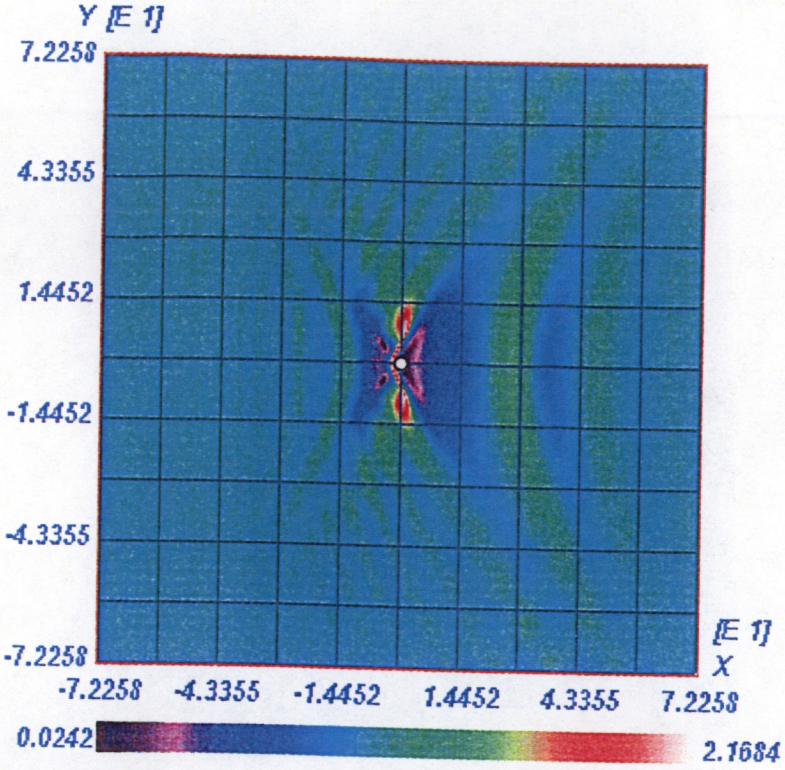

a.

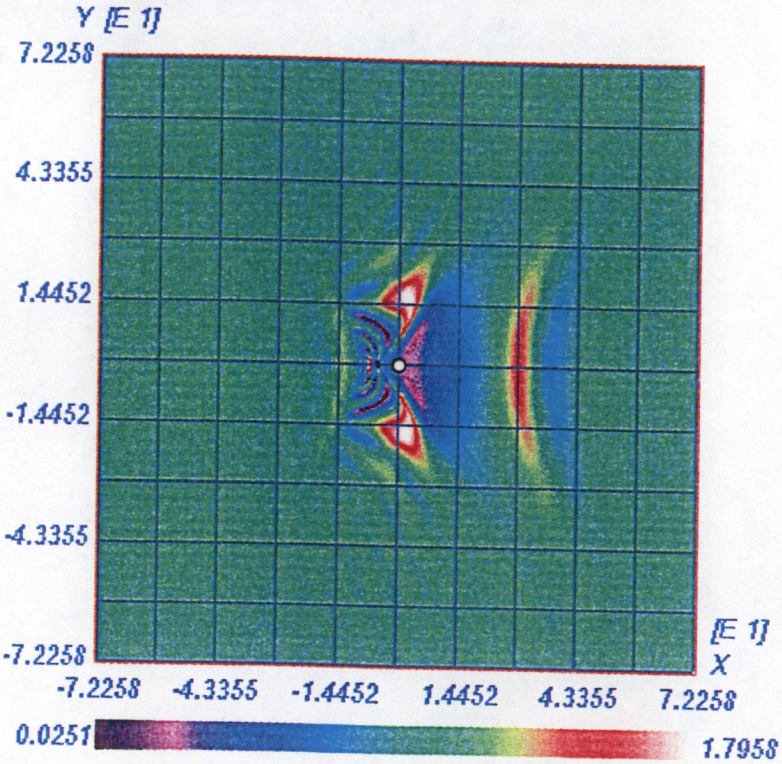

b.

Fig. 2.6. Results of the corresponding theoretical calculations for the region 4m x 4m presented (a) in Fig. 1.11d and (b) in Fig. 1.11c.

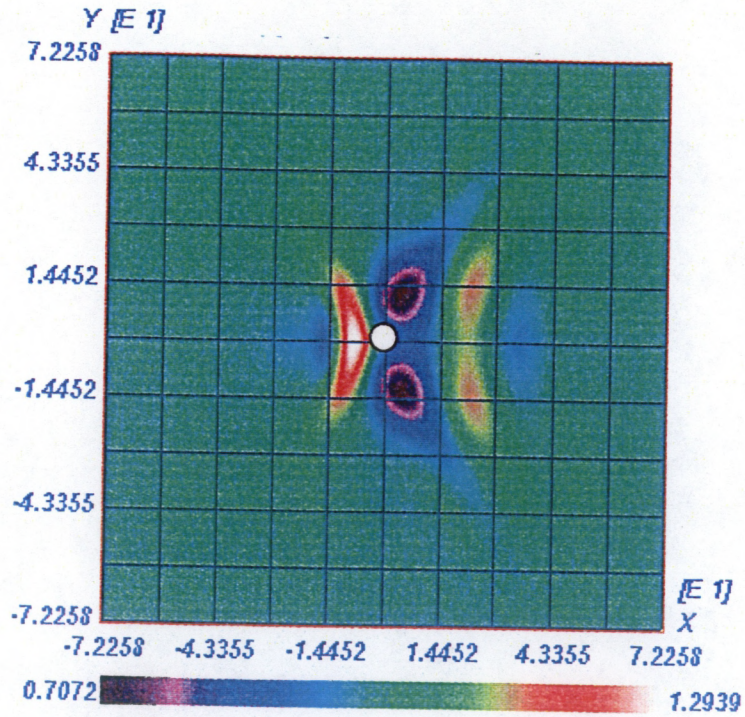

a.

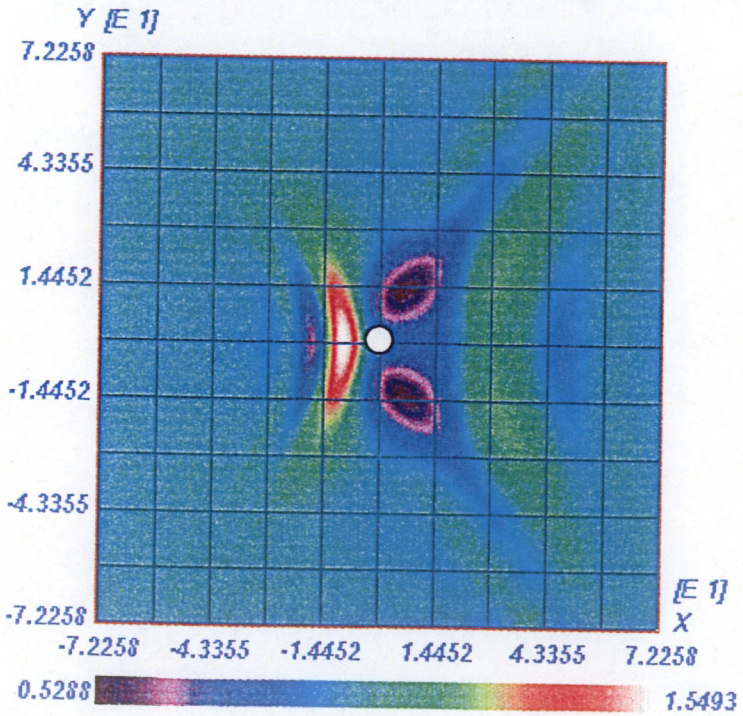

b.

Fig. 2.7. Results of theoretical calculations for the region 4 m x 4 m, corresponding to the experiments presented (a) in Fig. 1.6c and (b) in Fig. 1.7c.

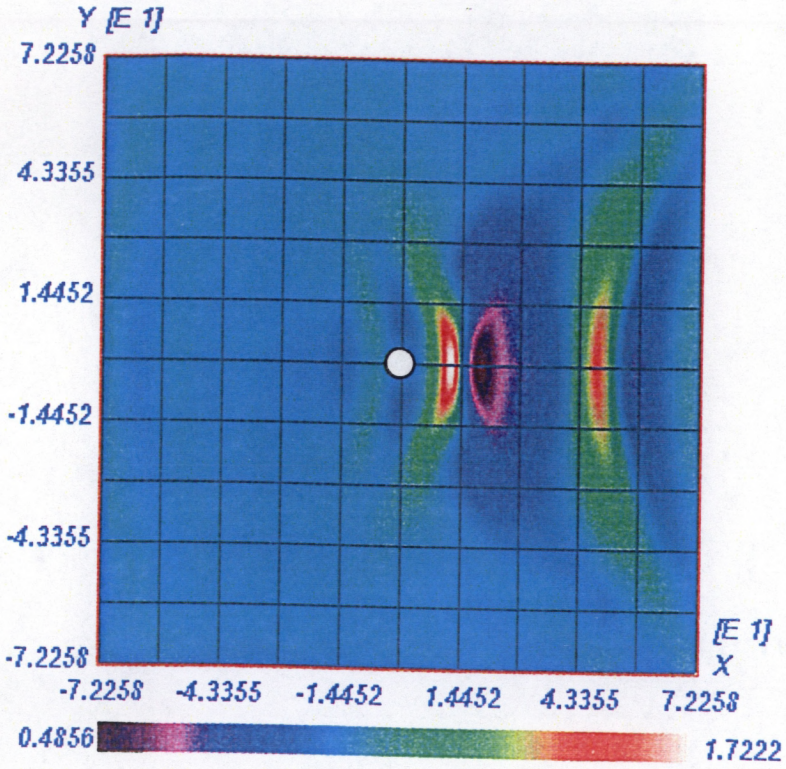

Fig. 2.8. Same as in Fig. 2.7b with the value of a_0 increased five times. Location of sphere is indicated by white circle.

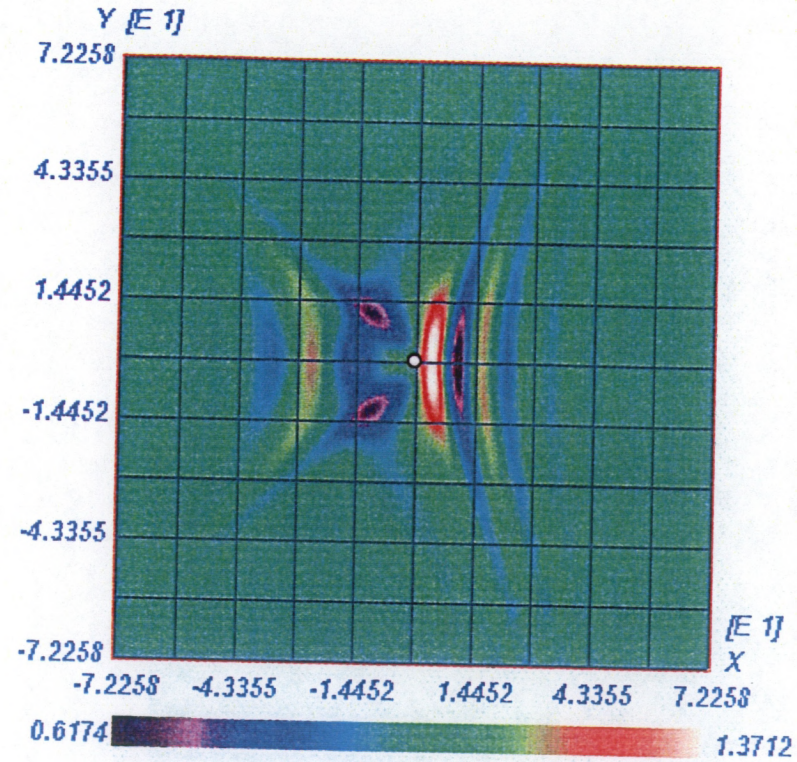

a.

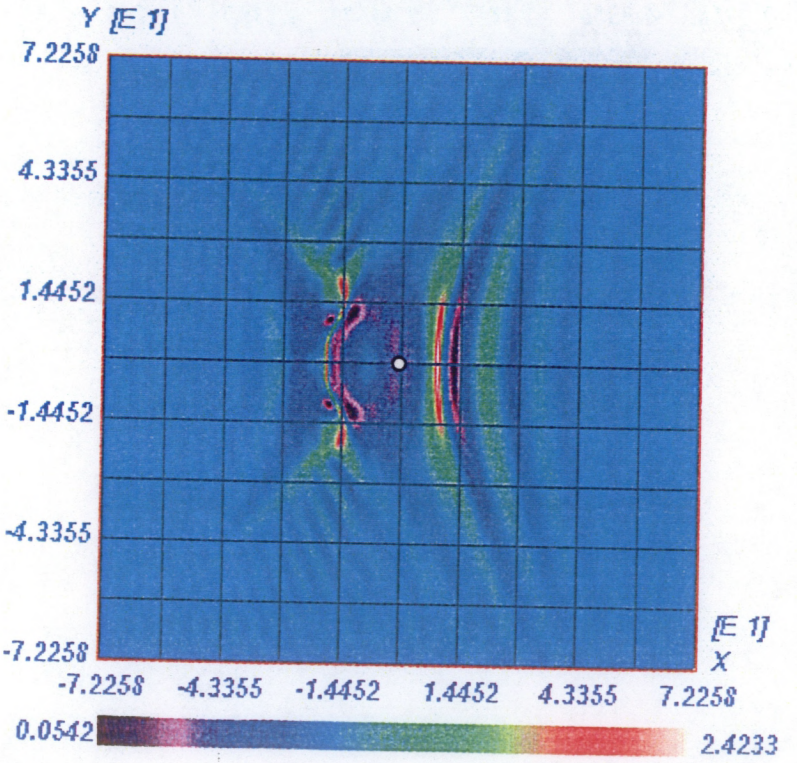

b.

Fig. 2.9. Results of calculations c for the region 4 m x 4 m, corresponding to the experiment presented in Fig. 1.4c. The value of a_0 in (b) is twice as large as in (a).

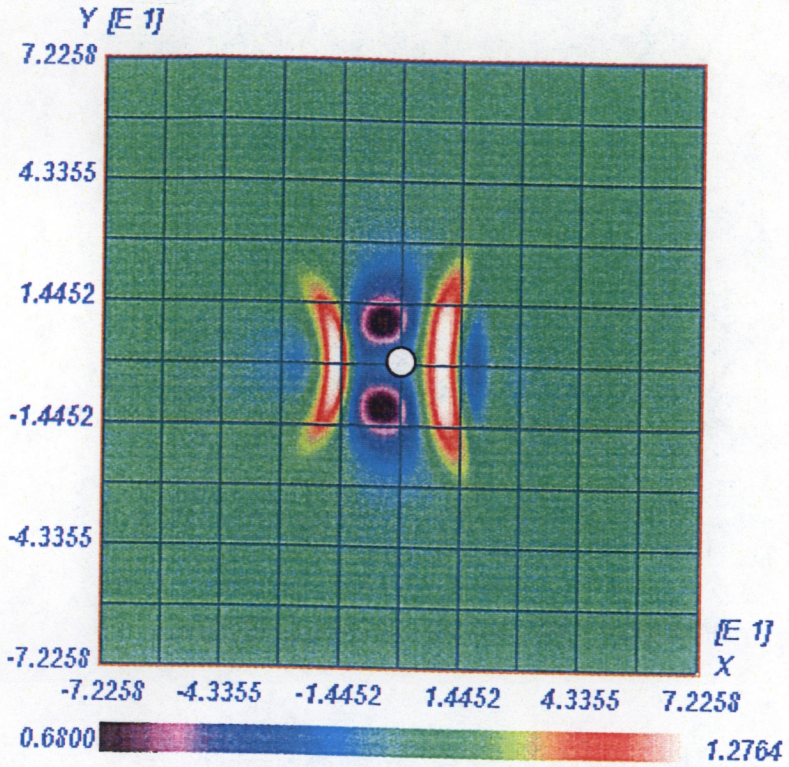

Fig. 2.10. Results of theoretical calculations for the region 4m x 4m, corresponding to the experiment presented in Fig. 1.6d